Patterning Principles in Vertebrate Sensory Systems.

by

Rebecca M. Long

A thesis submitted in partial fulfillment of the requirements for the degree of

Doctor of Philosophy

Neuroscience and Mental Health Institute

University of Alberta

Abstract

Patterns are predictable, ubiquitous, and functional. In something as complex and vast as the nervous system, patterns play an important role in maintaining order through logical organization. Sensory systems are one such example where neuronal organization show common patterns across modalities. From the distributions of different sensory receptors in their terminal organs, to the final central organization in cross-modality integrative regions, consistencies appear across both senses and species. This thesis will describe different aspects of patterning techniques employed at all levels of sensory processing, in three animal models covering a wide range of vertebrate phylogeny.

The first project focuses on one proposed theory of how patterns form, using the adult mammalian peripheral nervous system (PNS) as a model. The adult mammalian PNS, which is at constant risk of injury and disruption, must have a guidance mechanism to help re-pattern sensory nerve fibre terminations following an injury in the adult animal. We investigate the clustered protocadherins and their role in the control of outgrowth and spacing of somatosensory terminals in the skin and show how protocadherins may exert an inhibitive effect on the outgrowth of regenerating axons. This project also discusses how they are likely employed in organizing neurons of the same subtype following a peripheral nerve injury, which is necessary to maintain proper sensory feature separation.

The second project investigates the organization of primary sensory projections once they enter the central nervous system. The distribution of primary projection terminals of the vestibular system in snakes, a relatively unique and understudied clade of reptiles, show similarities in the distribution patterns with other reptilian and non-reptilian organisms. Utilizing

a novel tracing technique in an *ex vivo* prep, we show that the patterns exhibited by primary terminations are divided by the sensory feature detected, and that this pattern seems to be consistent with other studied vertebrates.

Finally, the third project focuses on the function of a pattern. Sensory systems exhibit modular organization, and when integrating across modalities, this modular organization remains conserved. As individual features of sensory stimuli are segregated at the point of transduction, as well at the point of primary cortex, this separation is maintained all the way up until higher cortex where they then can be integrated with other modalities. Using the vestibulocerebellum of the pigeon as a model, we examine these alternating modular zones. We show that each zone has distinct electrophysiology and speculate how they could integrate the visuo-vestibular input to participate in the modulation of direction specific vestibulo-ocular reflexes.

By understanding different aspects of patterning in the sensory nervous systems, and how the architecture is common across vertebrates, we can make inferences into how they work based on similarities in other systems within the brain.

Preface

The research presented is original work completed by Rebecca Long, with edits suggested by the examining committee, under the supervision of Dr. Douglas Zochodne. The research projects in Chapter 2 and Chapter 4 received research ethics approval from the University of Alberta Animal Research Ethics Board and Animal Care and Use Committee (ACUC), and was carried out in accordance with the University of Alberta Health Sciences Laboratory Animal Services (HSLAS) and the Sciences Animal Support Services (SASS) standards and guidelines. The project in Chapter 3 received research ethics approval from the corresponding authorities from the Government of Upper Bavaria, and the Technical University of Munich.

Chapters 3 and 4 were completed under the supervision of Dr. Douglas Wylie.

A version of Chapter 4 has been published in the *Journal of Neurophysiology*, as Long RM., Pakan JMP., Graham DJ., Hurd PL., Gutierrez-Ibañez C., and Wylie DR, "Modulation of complex spike activity differs between zebrin-positive and -negative Purkinje cells in the pigeon cerebellum", vol. 120, pages 250-262. I was responsible for the conception, design, data collection and analysis, and writing of the manuscript. DRW was the supervisory author and was also involved in all steps of the production of this manuscript. JMP was involved in conception, design, data collection and analysis, and editing of the manuscript. DJG as involved in conception, design, data collection. PLH and CG-I were involved in data analysis and manuscript edits. All authors approved the final version of the manuscript.

Acknowledgements

Equal credit for this thesis belongs to the incredible support system that got me through its creation. I would like to first and foremost thank my supervisor, Dr. Douglas Zochodne, who welcomed me into his lab with open arms in the middle of my degree and entrusted me with this project. With his mentorship, guidance, and endless encouragement, I was able to jump headfirst into a field I had no knowledge or experience in and made something stick. I cannot thank the entire Zochodne lab enough for their incredible help and support over the past two years. Anand Krishnan, Prashanth Komirishetty, Aparna Areti, Twinkle Joy, Kasia Zubkow, and Honyi Ong, you made my experience here unforgettable. As well, I'd like to specifically thank Ambika Chandrasekhar, Arul Duraikannu, and Matt Larouche for their technical help with PCR, genotyping, general troubleshooting and daytime chats. I'd be here for many more moons fumbling through without your assistance. Trevor Poitras, thank you for being my PNS lifeline. You taught me everything I know in the lab, and dug me out of whatever hole I ended up in. To Dr. Wylie, Cristian, and Iulia, I want to send a heartfelt thank you for the early years and beers!

I must acknowledge the support staff I had the privilege of working with during my degree. First, I'd like to thank Mr. Isaac Lank in the Psychology department for always being there when I needed, be it coffee, electrical, or mechanical assistance. As well, I'd like to thank Megan Eatock and Chantelle Sedgwick in the NMHI office for your guidance and chats, and to the maternal force of the NMHI, Amber Lapointe, for absolutely everything.

I'd also like to thank the entire 2018-2020 NGSA team, and all other fellow students I have met over the years. You helped me through some tough times, and I wish I could have started this journey with the connections I had made by the end. Know that I would name you all

if I could, but I want to thank each of you specifically for the hellos in the hallways, the chats over beers, or the rants in the bathroom, all of it helped me to get where I'm at now.

To my family; thank you. Your patience for unwarranted facts beyond your interest has not gone unnoticed. To my brothers, Willi and Michael, and my sister Lisa, thanks for the support and stress relief needed throughout this time, and for the excuses for the necessary mental health vacations I never would have otherwise taken. To my uncle, Dr. Steven Heine, for your academic wisdom I only sometimes (but should've always) heeded. To my parents, Brenda and Malcolm, thank you does not accurately capture how much your love and support has helped me through this.

Finally, to Scott. Thank you for all the grounding you have provided and talking me out of whatever tangent I got fixated on. Your wisdom, maturity, and emotional intelligence have helped me with more than just MATLAB and stats. Sorry you had to deal with thesis-writing Quarantine Becky…

To all my colleagues, friends, family members, and mentors, this chapter of my life could not have been completed without your help.

Table of Contents

List of Tables

List of Figures

Chapter 1: Introduction

1. Introduction

1.1. The blind men, the elephant, and the senses

We exist in a physical world, surrounded by various forms of energy and chemicals. To survive, organisms must internalize these signals to extract valuable information regarding the state of the world around them. Sensory systems achieve exactly that, providing the receptors to collect and translate stimuli from the environment into meaningful, useful signals that guide us towards or away from what may be necessary for survival. This dissertation includes work from several disciplines within sensory neuroscience. This approach, while initially unintended, has enlightened me to the unique advantage afforded by multiple perspectives. Perhaps best illustrated through the ancient Buddhist parable, John Godfrey Saxe (1868), highlights the importance of multiple approaches when solving a problem in his poem "The Blind Men and the Elephant" (Saxe, 1868 p.259–261). Six blind men hear of a strange creature called an elephant, but none had any idea of its shape or form. Through touch, each man investigates a different part of the animal, such as the ear, tail, or leg, and each come to a very different conclusion based on their independent findings: "…the Elephant is very like a fan…a rope…a tree!". Though each of their own conclusions have merit, it is not until the men communicate with each other to share their collective findings do they begin to approach an accurate description of an elephant. This example is used to demonstrate the necessity of collaboration between disciplinary fields when tackling something as complex and intricate as the brain. We are perhaps naïve to how much progress we can achieve when we become pigeon-holed in a single topic, cell type, or protein, and we forget to recall the overall picture. By learning about multiple sensory systems, especially across a wide range of species, we can perceive unique parallels and are able to draw yet further

inferences about how the nervous system may function. Obviously, there is enormous biological diversity between species, driven by unique modifications forced through evolution, but this should only serve to highlight the importance of what remains (or becomes) the same (Miller et al., 2019). Common organizational principles across species are strikingly paralleled within the systems themselves, with different sensory systems sharing similarities in organizational structure. Parallel feature processing, hierarchical design, and interactions between neurons employ common patterning principles, regardless of what sensory modality they belong to. Therefore, this thesis will take advantage of a variety of animal models and sensory systems to emphasize the pervasiveness of patterning strategies within and across sensory systems. Three aspects describing fundamental principles of patterns within the sensory nervous system will be investigated: how patterns are formed, what they look like, and what function they serve.

1.2. Patterned organization of sensory systems

The development of the eye through evolution began small, first as low resolution light detectors, and gradually expanded in function to be the incredible organ we use today (Arendt et al., 2009; Randel and Jékely, 2016). By increasing the features of stimuli that are extracted through diversification of the number of neurons and receptors, organisms could begin to recreate a more accurate internal experience of the stimuli through sensory integration. However, as the nervous system grew larger with more cells, the task to properly connect with specific neurons became more difficult. Neurons must now navigate millions of cells to find a specific target, and this journey must be made consistently across organisms for proper function. The brain is not organized randomly, but rather is highly specific, and shows repeated stereotypical patterns. Pioneering neuroanatomists, such as Cajal, made intricate observations that neurons are discrete units, and coined the Neuron Doctrine (Ramon y Cajal, 1889), which led to the

discovery and description of the synapse, the point of connection and communication, in 1897 by Sherrington (Sherrington, 1952; López-Muñoz et al., 2006). The first project in this thesis will question how neurons consistently make connections to produce the same functionality we see within and across species.

1.3. Patterns are predictable: Chemoaffinity Hypothesis

There were two seminal experiments conducted around the turn of the 20th century. The first was completed by John Langley (Langley, 1895), who studied regeneration of the autonomic system of the cat. Within the superior cervical ganglion, which is innervated through a common nerve, there are neurons that innervate several organs. Some axons innervate the ciliary muscles to control pupil dilation, some control the vasoconstriction of the vessels within the ear. Langley severed the nerve and once re-apposed, he observed a curious result: regenerating fibres would only connect with neurons that innervated the same tissue as before and did not "run indiscriminately to such cells as may be on their course". Less than 50 years later, Roger Sperry followed up with a series of experiments examining the regeneration of visual function following a 180° rotation of the eyeball in lower vertebrates (frogs, newts, and toads, Figure 1.1). Following regeneration from the optic neurons to the tectum, vision was orderly, albeit inverted. Neurons that projected from the dorsal region of the retina, reconnected with the respective dorsal neurons within the tectum, despite arising from the now-ventral portion of the eyeball. When a food source was presented above the animal, the animal behaved as if the food was below and turned towards the ground (Sperry, 1943; Meyer, 1998). Langley describes a "special chemical relation between each class of nerve fibre with each class of nerve cell" (Langley, 1895).

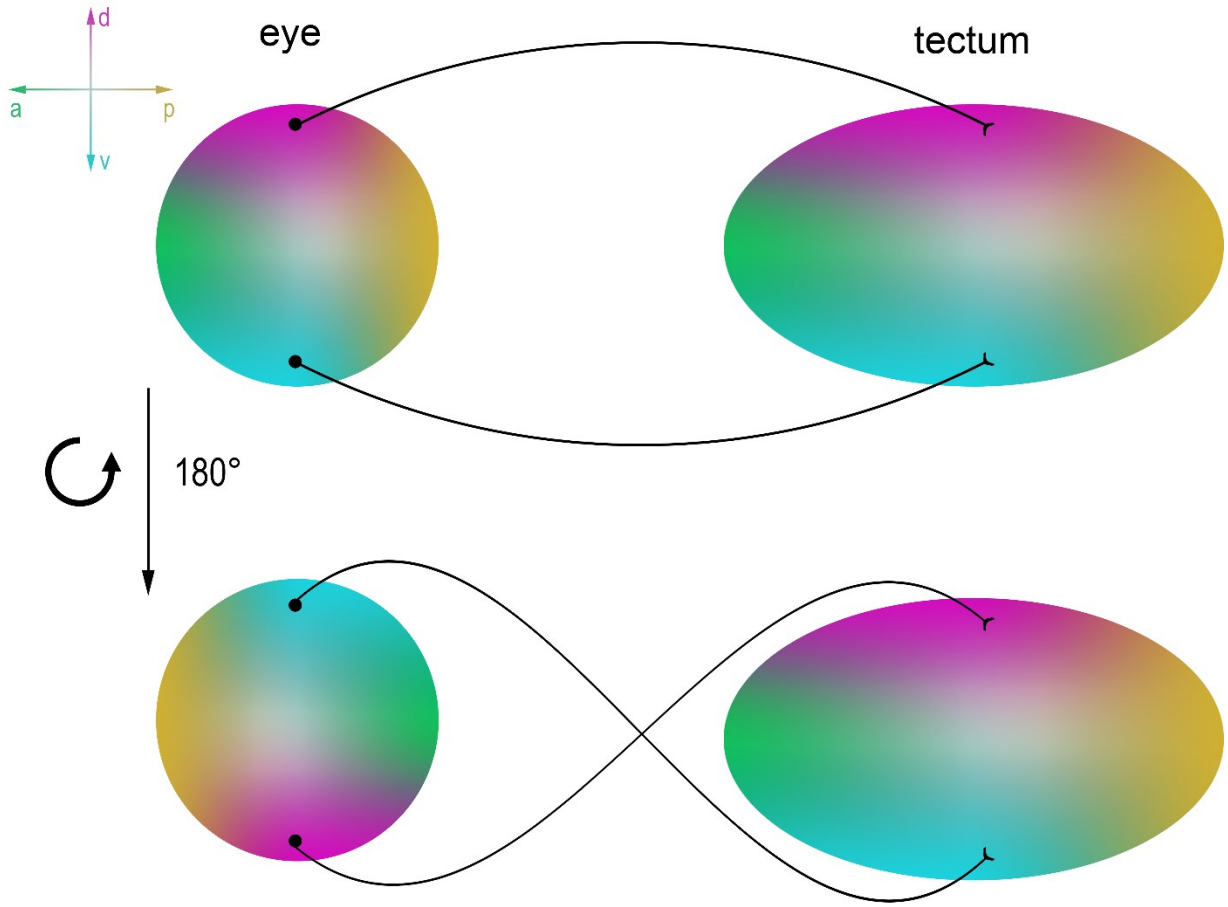

Figure 1.1: *Regenerating retinal ganglion cells will reconnect with original targets in the optic tectum.* Retinal ganglion cells (RGCS) on the retina project to topographically corresponding zones within the optic tectum (pink, d, dorsal; yellow, p, posterior, lateral; blue, v, ventral; green, a, anterior). Following the inversion of the eyeball and subsequent regeneration, RGCs will reconnect with the same tectal zone, regardless of the orientation of the eyeball.

These two experiments suggest a presence of an identifying feature between nerve and target. However, considering the immense number of neurons present, there would need be a sufficient quantity of unique identifiers (for an in depth review of this topic, see Zipursky and Sanes, 2010). Three suggestions have been put forth. The first is a molecular gradient. Indeed, it has been suggested that epidermal innervation is guided by finite amounts of neurotrophins (Wang et al., 2013), however exogenously applied neurotrophins should then keep axons growing indefinitely, so long as the supply is maintained. This has been suggested in the retina as

well, (Gierer, 1982), however the retina has the problem of density, where axons would not be able to distinguish among intermingled neurons. Second, specific guidance could be achieved through the concerted actions of short- or long-range attractants, repellants and their respective receptors, but the sheer number of molecules involved has been deemed inelegant and complicated (Zipursky and Sanes, 2010), though this does not negate the possibility. Finally, the third suggestion is through distinct binding specificities that are differentially expressed within each cell, like an individual stamp or "barcode". However, for a barcode to be effective, each cell would need to have its own unique isoform, and cells would need to use these isoforms to identify "self" from "non self". Given there are 10^{12} neurons in the human brain making 10^{15} connections, how can a genome with 30,000 genes fill this requirement (Hattori et al., 2008)?

Taking advantage of the unique options for genetic manipulation available in a mouse model, the first project in this thesis focuses on the clustered protocadherins, a novel, potential "barcode" molecule, and its role in the mammalian peripheral nervous system. The peripheral system provides the opportunity to see how this guidance mechanism functions during regeneration following a nerve injury, and how sensory neurons behave when they need to regrow axons into previously innervated territory. We believe the clustered protocadherins play a role in the regeneration of adult peripheral sensory neurons.

From the sensory terminals, neurons must then project to higher areas for further sensory integration. We will discuss in the next chapter what this organization looks like, and how the organizational principles seen in primary sensory projections are also exquisitely conserved across species.

1.4. Patterns are hierarchical and conserved

Perhaps the most intriguing aspect of the organization of the nervous system does not arise from its complexity, but rather in its consistency. The pursuit of comparative, evolutionary neurobiology may appear less glamourous, but is no less important, as the underlying meaning of these similarities can speak volumes and help provide context to aid many other discoveries in all disciplines. Captured in his 1973 essay, Dobzhansky exclaims how "nothing in biology makes sense except in the light of evolution" (Dobzhansky, 1973). However, since evolution is ongoing and the accumulation of genetic variation is inevitable, the brain maintains striking similarities across many parameters, with sensory systems showing distinct commonalities between distantly related species (Casanova et al., 2011). These shared organizational strategies are not just products of evolutionary accumulation but can also appear across species independently. Reviewed by Sanes and Zipursky (2010), the comparison of the visual circuits between fly and vertebrates is one such example. Both species have the same general organization of the retina, with multiple neuronal types evenly distributed in layers, divergent and convergent connections between photoreceptors, and parallel processing of visual features in distinct regions in higher cortex, however these systems arose independently. Independent evolution, therefore, should further emphasize the importance of an organizational pattern. Although, it is important to note that the similarities observed should not negate the existence of innovation. Driven by their ecological demands, sensory innovation does exist in response to novel stimuli (ie. magnetoreception, infrared detection, electroreceptors), but the development of these systems follows the same framework seen in the established sensory systems as they are typically modifications on already existing structures (Hartline, 1974; Gregory et al., 1988; Hodos and Butler, 1997). Sensory receptor cells are typically unipolar or pseudo-unipolar, and synapse onto

second order neurons before integrative processing. Despite some elaborations across species, the underlying organization is the same. Most interestingly, the central representation of the somatosensory system displays isomorphic representation, where there is fidelity in structure to the reflection of the area of the nervous system it represents (Hodos and Butler, 1997). The face appears face-like in human somatosensory cortex, with the nose situated between the eyes and the lips, the distribution of vibrissae of a rodent perfectly recapitulated in barrel cortex, and, most dramatically, the finger-like processes of the star-nosed mole exhibiting a disturbingly accurate depiction on somatosensory cortex (Penfield and Boldrey, 1937; Woolsey and Van der Loos, 1970; Butler and Hodos, 1996; Catania and Kaas, 1996). This organization contains divisions dictated by the receptive fields. Another feature that is conserved across these systems, is its hierarchical organization, a sequential progression of organization, where modules within the system can be further subdivided into even more basic components (Meunier et al., 2010; Hilgetag and Goulas, 2020). These arise during expansions of sensory cortex over evolution (Kaas, 2008). But in sensory systems that do not vary much species to species, the organization shows a more overt consistency in organization, as well as simplicity (Hodos and Butler, 1997; Straka and Baker, 2013).

The second project in this thesis uses a novel tracing technique to investigate the projections of the vestibular system at the level of a single semicircular canal. This preparation allowed us to probe complex anatomical projections in a unique organism. Snakes are limbless animals that experience a notably different perspective of the world, and by investigating a deeply innate sensory system such as the vestibular system, will allow us to see striking similarities between the snakes, and other late-branching vertebrates. Despite these differences in

experience, we hypothesize that the vestibular primary afferent terminations in the snake will be like that of other studied vertebrates.

1.5. Patterns are meaningful and functional

Such deep consistency and conservatism seen across species begs to be recognized as fundamentally important. These patterns of organization of sensory cortex and its similarities across species likely occurred due to their systematic development. Similar to how the retina evolved from a single photoreceptor, to simple Reichardt motion detectors, to the mammalian eye, the brain has shown similar expansions in processing power to accommodate new incoming stimuli (Kaas, 2008; Randel and Jékely, 2016). However, the brain maintains the separation of features in discrete units, and, despite some local pre-processing, most integration occurs at the level of the brain (Hartline et al., 1956; Moayedi and Davis, 2013). The separation of these features create an internal representation of the complex stimuli that our brains can then integrate and utilize (Masland, 2012; Abraira and Ginty, 2013). As well, the organizational order appears to be driven by features unique to the stimulus itself. The auditory system shows organization based on frequency, the somatosensory system is organized based on the types of tactile receptor, and the olfactory system is organized based on odorant chemical structure (Penfield and Boldrey, 1937; Mountcastle, 1997; Talavage et al., 2004; Johnson and Leon, 2007). It is biologically conservative to keep cells with similar roles spatially near each other, instead of having to communicate over long distances (Kaas, 2008; Meunier et al., 2010). This likely arose due to the local expansion of sensory systems throughout evolution. Early animals had smaller brains, fewer neurons, and fewer cortical areas, while the human brain has an over 10-fold increase in the number of cortical areas in comparison, paired with a much more complex connectional network. For example, compared to early mammals, primates have an enlarged primary motor

cortex with more area devoted to the forepaw, presumably for manipulating objects. They also have an expanded visual system, with more hierarchical levels, and new areas such as the motion-sensitive middle temporal area, MT, which is supposedly unique to primates (Kaas, 2008). The visual system is the most studied sensory system, likely because of the human dependence of vision as our primary sense. This focus has unveiled several further layers within the retinotopic hierarchy within primary cortex. Primary visual cortex contains hypercolumns for each receptive field, which is a cortical column that can be subdivided into two ocular dominance columns, one dedicated to each eye. These columns are then further divided into orientation columns, which are vertical collections of neurons that respond to the same orientation of stimulus, adjacent to columns that detect orientations that deviate by a few degrees (Hubel and Wiesel, 1963; Hubel et al., 1977). These subdivisions all contribute to the logical integration of simple stimuli, which assists in the computational integrative power of sensory cortex (Masland, 2012; Abraira and Ginty, 2013).

The final project in this thesis will focus on the level of sensory integration in the cerebellum, a remarkably conserved structure. We will discuss the benefits afforded when sensory features are kept separate, and how the patterns in which they terminate allow for differential processing. Using an avian model, we will describe a possible function represented within patterns based on submodules within the visually sensitive and exquisitely conserved vestibulocerebellum. We hypothesize that there exists a separation of sensory features within these submodules, and that this separation can assist in fine-tuning the vestibulo-ocular reflex.

The overall goal of this dissertation is to highlight organizational principles seen within sensory systems, and to draw parallels that are consistent not only across species, but across sensory systems themselves. To appreciate why these patterns form, it is perhaps best to learn

how they form. The first project in this dissertation will focus on one recently proposed mechanism, the clustered protocadherins, and how they function in the adult nervous system. Further, we hypothesize that they play a role in guiding the regenerating adult peripheral nervous system.

Chapter 2: Clustered protocadherins and their role in the regeneration of the mammalian peripheral nervous system.

This work was completed under the supervision of Dr. Douglas Zochodne, from April 2018 – June 2020.

Abstract

The mammalian peripheral nervous system is at constant risk of insult and injury. While there exists a capacity for axon regeneration, this regeneration is often incomplete, and is not greatly understood. One aspect that is unclear during peripheral nerve regeneration is the patterning of sensory nerve fibres in the skin, and these mechanisms may provide insights to how the fibres distribute during development. In the developing central nervous system (CNS) growing neurons use self-recognition strategies, which in mammals is driven by the clustered protocadherins (Pcdh). This effect has been demonstrated in multiple types of CNS neurons, but its expression and function are unknown in the PNS. Given the role of Pcdh in the CNS, we hypothesize that the γ subcluster of the Pcdh gene (Pcdh-γ) participates in the patterning of epidermal re-innervation and contributes to regenerative outcomes.

Using the adult mouse peripheral nervous system as a model, we show that the expression patterns of Pcdh-γ are localized to the cell bodies within sensory peripheral nerves. We knocked down the Pcdh-γ protein in adult dorsal root ganglion cells (DRGs) and observed greater rates of neurite outgrowth compared to a group with the Pcdh-γ protein intact. However, this difference was not maintained after injury. As well, we also noted there was a decrease in neurites crossing over self-neurites, but only following an injury.

Additionally, we observed regeneration in animals that had Pcdh-γ knocked down *in vivo* following a sciatic nerve injury, and found that injured animals with Pcdh-γ knocked down exhibited higher rates of epidermal axons penetrating the epidermis compared to the non-injured foot, suggesting that an intact Pcdh-γ may act as an outgrowth restrictor, but only several days after the injury.

These results suggest that the Pcdh-γ may influence sensory neurite patterning following regeneration and is the first description of a function Pcdh-γ may have in the peripheral nervous system. Furthering our understanding of the mechanisms behind peripheral nerve regeneration and the factors that influence regrowth may have important implications for therapeutic strategies, and this project provides the first step to understanding how re-growing axons distribute themselves following a peripheral nerve injury.

Abbreviations:

CMAP	compound motor action potential
CNS	central nervous system
CTCF	corrected total cell fluorescence
CV	conduction velocity
da	dendritic arborization neurons
DRG	dorsal root ganglion
DSCAM	Down Syndrome Cell Adhesion Molecule
HTMR	high threshold mechanoreceptor
LTMR	low threshold mechanoreceptor
NF200	high molecular weight neurofilament (200kD)
Pcdh	clustered protocadherins
Pcdh-γ	clustered protocadherins gamma subcluster
PNS	peripheral nervous system
qRT-PCR	quantitative real-time polymerase chain reactions
RAGs	regeneration associated genes
RFE	relative fold expression
RPLP0	ribosomal protein lateral stalk subunit P0
SC	Schwann cell
siRNA	small interfering ribonucleic acid
SNAP	sensory nerve action potential

2. *Introduction*

2.1.1. *Anatomy of the peripheral nervous system*

The peripheral nervous system (PNS) provides the circuitry to connect the physical world and state of the body to the brain. While the PNS can be divided into two parts; somatic sensation and autonomic innervation, in addition, the PNS also includes the axons of the somatic motor neurons, which originate from the anterior gray matter of the spinal cord, and travel through peripheral nerve trunks (Kandel et al., 2000). The perikarya of the sensory neurons exist in the dorsal root ganglia (DRG), a collection of cell bodies located just outside the spinal cord. DRG neurons are pseudo-unipolar, extending a single axon before bifurcating into a central process, which projects to the dorsal horn of the spinal cord, and a peripheral process, which travels through the nerve trunk to its target tissue. Motor neuron axons join and blend with the peripheral projections of the DRG to form a mixed nerve trunk, a highway of afferent and efferent connections connecting the CNS to the rest of the body. The nerve trunk can be further parsed into fascicles, encompassed within three layers of connective tissue: the epineurium, perineurium, and endoneurium. As the outermost layer, the epineurium is continuous with the dura and arachnoid layer of the CNS (Zochodne, 2008). This provides most of the protection for the internal bundle of nerves. It also includes the arteriolar and venular feeding plexus of the vasa nervorum, providing the critical blood supply to the capillaries and nerves within. Below lies the perineurium, which wraps around endoneurial fascicles, and participates in the blood-nerve-barrier, a leakier PNS homologue to the blood-brain-barrier. The innermost layer, the endoneurium, encloses the axons directly. In addition to the nerves, the endoneurium is also home to another major player of the PNS, Schwann cells (SC), which provide support and myelination for peripheral axons. The endoneurium also contains capillaries, as well as other

resident immune cells (Zigmond and Echevarria, 2019). However, despite the many connective layers, they provide insufficient physical protection. While the delicate brain and spinal cord exist within the protective recesses of the skull and vertebral column, cells within the PNS are exposed and vulnerable to injury. Depending on how many layers of the nerve trunk are disrupted, several different degrees of injury are possible (Robinson, 2000; Zochodne, 2008). In addition, disturbances to nerves can arise from disease. Neuropathies, which can alter the normal functioning of the nerve without an extrinsic insult, arise through pathological degradation due to disorder or disease (Robinson, 2000). Both events are highly prevalent and can have permanent devastating impacts on patients.

2.1.2. *Injuries to the PNS*

About 3% of all patients entering a level 1 trauma centre experience a peripheral nerve injury (PNI), and around 2.4% of the general population suffer from a peripheral neuropathy (Robinson, 2000; Taylor et al., 2008). This thesis will focus on peripheral nerve injuries, as a result of a physical external insult. To combat these risks, the PNS has developed strategies to regenerate, but these are substantially limited by factors that include the degree of injury. The degree of injury is defined by which layers of the nerve trunk are disrupted. The mildest, disrupting only the myelin sheaths covering the axons within the nerve trunk, is called neurapraxia, and typically recovers fully within weeks to months. If there is axon interruption, the classification is elevated to axonotmesis, and has several subdivisions. Depending on which of the three connective layers are disrupted, these injuries can be classified as second degree (all three layers intact), third degree (endoneurial tubes disrupted), fourth degree (endoneurial and perineurial tubes disrupted), and fifth degree, also called neurotmesis, where all layers are disrupted (Seddon, 1943; Sunderland, 1951; Robinson, 2000).

While recovery from a nerve injury is possible, the ability for any spontaneous recovery in the PNS has perhaps created the perception that PNS regeneration is complete, but this is far from the case. Clinical evidence illustrates just how incomplete peripheral nerve regeneration is (Zochodne, 2012). There are substantial roadblocks preventing peripheral nerves from fully recovering, with the slow and reluctant rate of regrowth and the distance to target being some of the most significant (Zochodne, 2012).

2.1.3. *Regeneration*

Following an injury to a peripheral nerve, there are several important events that occur both proximally and distally to the injury site. Once the integrity of the axon has been breached, a "latent period" is initialized. Characterized by a loss of the enzyme NMNAT and the activation of SARM1, both events result in a loss of NAD+, a major component of ATP formation. Following the drop in ATP, an active molecular degeneration program begins, culminating in cascades of calpains and proteases, initiating microtubular dissolution and mitochondrial dysfunction of the distal nerve stump (Finn et al., 2000; Yahata et al., 2009; Barrientos et al., 2011; Zochodne, 2012; Gerdts et al., 2013; Yang et al., 2013; Conforti et al., 2014). This process of axonal degeneration, first described by Augustus Waller in the mid-1800s, is termed Wallerian degeneration, which is defined as axonal breakdown following a nerve transection. If the axon is not transected, but rather crushed to the point where similar disintegration follows, the process is called Wallerian-like degeneration (Waller, 1850; Zochodne, 2012). Local SCs dedifferentiate into an active state and together with recruited macrophages, phagocytose axonal debris (Zochodne, 2012; Jessen and Mirsky, 2016; Zigmond and Echevarria, 2019). Delays in the clearance of the distal stump debris have been associated with impaired regeneration as debris provides an inhibitive environment to newly regenerating axons (Brown et al., 1992;

Fournier and Strittmatter, 2001). Once the axonal debris has been cleared, a growth cone slowly begins to emerge from the proximal stump and, with the trophic support of SCs, regeneration can begin. (Navarro et al., 2007; Bradke et al., 2012).

Concurrently, a response is being mounted in the cell body. Following the injury, retrograde signals travel back to the soma to initiate the "cell response". This event can be visualized through morphological changes occurring within the soma. Central chromatolysis describes the disintegration of the dark endoplasmic reticulum, or Nissl bodies, as the neuron primes itself for a regenerative or growth state (Cragg, 1970; Lieberman, 1971; Zochodne, 2012). In addition to morphological changes, there are numerous transcriptional changes occurring within the nucleus. Following the injury, there is a downregulation of more constitutively present genes (eg. neuropeptides, neurofilaments subunits) in favour of an upregulation of regeneration-associated-genes (RAGs, Verge et al., 1996). RAGs include genes such as β-III tubulin, GAP43/B50, ATF3, NOS, HSP27, Arg-1, IL-6, and BDNF, among others (Zochodne, 2008, 2012; Senger et al., 2018). How these RAGs influence the regenerative capability of the neuron is still not well understood, and mounting evidence suggests there are sensitive time periods when RAGs are more effective (Christie et al., 2014; Oh et al., 2018; Zubkow, 2018).

Despite all these pro-regenerative events, peripheral regeneration still faces significant barriers to success, and can leave patients facing permanent sensory, motor, and autonomic deficits. Many of these hurdles result from the slow rate of axon growth, approximately 1-3mm/day, and the distance of the target tissue, which can be up to a meter away (Navarro et al., 2007; Zochodne, 2012). As well, the longer it takes for regeneration to occur, the poorer the outcome will be (Sulaiman and Gordon, 2013). Sensory neurons, which are the focus of this

thesis, innervate the furthest reaches of the PNS in the dermis and epidermis and are particularly impacted by these factors.

2.1.4. *Tactile sensation*

There are several types of cutaneous sensory receptors that each detect unique features, dispersed throughout the skin within the dermal and epidermal layers (Willis and Coggeshall, 2004). The different types of signals each neuron is specially designed to detect include nociception, temperature, vibration, and pressure. This provides the ability for sensitive identification of stimuli through the integration of the different sensory modalities (Abraira and Ginty, 2013). Low threshold mechanoreceptors (LTMRs) in non-hairy, glabrous skin react to non-damaging physical stimuli such as vibration and light touch, through specialized endings such as Merkel cells, Ruffini endings, Meissner and Pacinian corpuscles (Cauna and Ross, 1960; Halata, 1977; Bell et al., 1994; Halata et al., 2003). As well, the skin acts as a key protector of the body and contains nociceptors, which are actively tuned to detect harmful stimuli. High threshold mechanoreceptors (HTMRs) exist in the epidermis to allow detection of damaging stimuli.

With the varying sensitivities to distinct features of touch, it can be appreciated how the skin is accurate at identifying different types of stimuli. But how can they coordinate to provide an integrative view of touch perception? The retina provides a relevant example where there are multiple neuronal types sensitively tuned to specific features of visual stimuli, and are evenly distributed across the tissue (Masland, 2012). Here, each subtype of neuron exists within a single layer of the retina, evenly spread out and avoiding other isoneuronal types in a phenomenon known as tiling. The somatosensory system has also been shown to exhibit specific patterning of sensory terminals across species (Kramer and Stent, 1985; Grueber et al., 2002; Sagasti et al.,

2005; Shrestha and Grueber, 2010; Kuehn et al., 2019). For example, nociceptors show specific placement, with the peptidergic fibres innervating the deeper regions of the epidermis, while the non-peptidergic fibres terminate in the more superficial layers (Zylka et al 2005). As well, the topography of somatosensation is conserved in the skin, with neurons projecting to adjacent terminals in the skin also projecting to adjacent regions within the spinal cord (Kuehn et al 2019). Interestingly however, these partnered neurons seem to arise from non-adjacent DRGs and can even be distributed across ganglia (Kuehn et al., 2019). How could peripheral and central processes know to maintain this innervation pattern while arising from distant cell bodies? As well, is this elaborate organization maintained following an injury, and its subsequent reinnervation?

2.1.5. *Patterning Strategies in the CNS*

As mentioned in the introduction, the chemoaffinity hypothesis provides an explanation for axonal guidance that is required for the journey peripheral neurons must embark on. Not only would this system be effective for guiding neurons to their ultimate targets, it also has implications for its innervation of its immediate area. Patterning of the numerous cutaneous sensory fibres innervating the skin must be coordinated to maximize coverage of each type, while minimizing the biological investment and encroachment on other neurons of the same type.

In the CNS, the structure of dendritic and axonal arbours is achieved through the utilization of two strategies. Self-avoidance is a phenomenon within cells that prevents intra-neuronal overlap of its own dendrites and axons. This results in even spacing of sister neurites from the same neuron. The other strategy, called tiling, prevents inter-neuronal overlap of dendrites and axons, and functions during interactions with neighbouring cells. Tiling is present

in layered tissue such as the retina, where there are layers of different cell types that must evenly spread out within their own class (Grueber and Sagasti, 2010; Jan and Jan, 2010). Both strategies result in efficient, coordinated innervation, minimizing redundant coverage of receptive fields. We wish to investigate if similar strategies are used in the mammalian PNS, and more importantly, if these strategies are maintained following injury.

2.1.5.1. Down Syndrome Cell Adhesion Molecule (DSCAM)

To create enough isoforms to provide each neuron with a unique identity requires elegance in the design of the gene, resulting in multiple variants from a single sequence. The Down Syndrome Cell Adhesion molecule (DSCAM) in *Drosophila* achieves over 38,000 isoforms through alternative splicing, where a stochastically selected exon from three separate groups are concatenated onto one another and translated into a unique variant of the protein, anchored by a common transmembrane region (Schmucker et al., 2000; Hattori et al., 2008). These isoforms also engage is very strict homophilic binding, where each of the three variable domains must match in order for successful binding to occur (Wojtowicz et al., 2007). This specificity in binding can provide cells with signals of self/non-self recognition, which the neuron can then respond to.

The functional role of DSCAM in *Drosophila* is best illustrated in the dendritic arborization neurons (da). da neurons are peripheral sensory neurons named for their grand arbours extending along the body wall but are restricted to compartmentalized spaces and display minimal overlap with dendritic fields of neighbouring da neurons. In DSCAM null mutants, these arbours exhibit fasciculation between dendrites and high instances of self crossings (Grueber et al., 2002; Soba et al., 2007). However, the DSCAM gene in vertebrates is significantly less complex, and does not show the same extensive repertoire as DSCAM in

Drosophila, suggesting the protein functions differently in vertebrates (Schmucker and Chen, 2009). Recently, another protein has been described to exhibit similar levels of isoform diversity arising from a common genetic sequence.

2.1.5.2. Clustered Protocadherins (Pcdh)

In 1999, Qiang Wu and Tom Maniatis described the clustered protocadherins (Pcdh), 52 novel cadherin-like genes that are organized with variable exons upstream from constant domain exons (Wu and Maniatis, 1999). They describe three "clusters", Pcdh-α, Pcdh-β, Pcdh-γ, containing 14, 22, and 22 exons respectively (Figure 2.1). At the end of the Pcdh-α and Pcdh-γ clusters exists several constant exons, which encode for a cytoplasmic domain. The Pcdh-β cluster contains no constant exons (Mah and Weiner, 2016). Pcdh are the largest group within the cadherin superfamily, and are expressed primarily within the nervous system, though are detectable at low levels in other organs such as the lungs and kidneys (Frank et al., 2005). Similar to the alternative splicing seen in DSCAM, Pcdh creates diversity through the alternative use of individual promoters, preceding each variable exon. The variable exons are then spliced onto the constant exons of the respective cluster, and form membrane-bound heteromultimers with other co-expressed Pcdh proteins (Tasic et al., 2002; Schreiner and Weiner, 2010). As each cell is capable of expressing multiple isoforms, the heteromultimers are the true driver behind the diversity Pcdhs exhibit (Esumi et al., 2005; Kaneko et al., 2006). In the case of Pcdh-γ alone, 234,256 tetramers are possible (22^4). Despite showing high promiscuity in *cis* interactions within the heteromultimer, Pcdhs also engage in strict homophilic binding in *trans* between cells (Schreiner and Weiner, 2010). Similar to DSCAM, this allows cells expressing Pcdh to determine whether an encountered membrane is self or non-self.

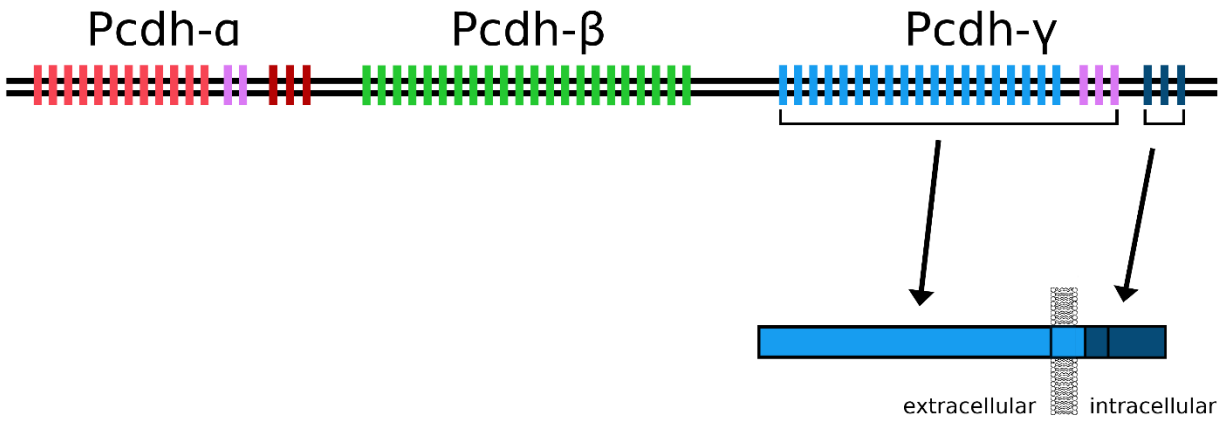

Figure 2.1: *Organization of the clustered protocadherins gene.* The gene is organized into three clusters (Pcdh-α, Pcdh-β, and Pcdh-γ). Pcdh-α and Pcdh-γ have both variable (light red, light blue) and constant exons (dark red, dark blue), while Pcdh-β only includes variable exons (green). During splicing, a unique promoter is chosen which encodes a single variable exon, which encodes the extracellular domain, and is then spliced to the 3 constant exons downstream, which encode the majority of the intracellular domain.

Of the three clusters, Pcdh-γ is the most extensively studied and the focus of this thesis. Pcdh-γ participates in the survival of spinal interneurons, however the role is not universal across interneurons, as some subtypes fare better in the absence of Pcdh-γ than others (Wang et al., 2002; Prasad et al., 2008). Recently, seminal work done by Lefebvre et al (2012) highlights the role of Pcdh-γ in the patterning of amacrine and Purkinje cells. Using conditional knockout mice, they show that starburst amacrine and Purkinje neurons lacking Pcdh-γ exhibit high instances of fasciculation and overlap, similar to the DSCAM mutants. As well, it has been shown that Pcdh-γ mutant neurons have decreased dendritic arborization (Garrett et al., 2012; Suo et al., 2012). Pcdhs have also been implicated in axonal guidance, as the olfactory system has been recently shown to be dependent on the cell surface diversity afforded by Pcdh (Mountoufaris et al., 2017). However, in the case of neural circuits, it has been shown that different parameters, such as number of neurons and synaptic strengths, can result in similar behavioural outputs, suggesting that neurons have additional compensatory mechanisms (Prinz et al., 2004). Despite the recent

explosion in literature investigating Pcdh, at the time of writing there has been very little focus on the role of Pcdh in the PNS, nor following a peripheral nerve injury. The available evidence suggests that Pcdh must be an important player in the growth and patterning of peripheral neurons, and we hypothesize that Pcdh-γ participates in the growth and patterning of epidermal neurons following injury. The following series of experiments aims to provide the first in-depth analysis of the function of Pcdh-γ in the mammalian peripheral nervous system.

2.2. Methods

2.2.1. *Animal Care*

C57BL/6 mice of either sex were used for all experiments. All experiments were carried out according to approved standard operating procedures and complied with the University of Alberta Animal Care and Use Committee, as well as the University of Alberta Health Sciences Laboratory Animal Services review, following guidelines from the Canadian Council on Animal Care.

2.2.2. *Animal Euthanasia*

Mice were euthanized via cardiac exsanguination under isoflurane anaesthesia. Once the mouse had reached surgical plane, the mouse was placed supine and an incision was made in the skin overlying the sternum. The diaphragm was cut to expose the heart, and the left ventricle was snipped and allowed to bleed out. Mice were then subjected to a secondary euthanasia measure (decapitation) to ensure death. All tissue was harvested fresh and fixed according to specific assay guidelines.

2.2.3. *Pcdh-γ Detection Methods*

2.2.3.1. Reverse Transcription and qRT-PCR

Tissue or cultured cells were collected and placed into TRIzol® reagent (Invitrogen, Waltham, MA). RNA was treated with DNase (Promega, Madison, WI) to eliminate any genomic DNA contamination. RNA was then subjected to a High Capacity cDNA Reverse Transcription Kit (Applied Biosystems, Foster City, CA) to generate complementary DNA. SYBR Green fluorophore (Applied Biosystems) was used for quantitative real-time polymerase chain reactions (qRT-PCR). Primer sequences are listed in Table 2.1. The cycle threshold (CT) was determined as the point where a fluorescing signal from the amplifying gene product can be distinguished against the background noise (Pfaffl, 2001). The CT value was then used in the comparative CT method ($2^{-\Delta\Delta CT}$) to calculate relative fold expression values (RFE) in relation to the housekeeping gene, ribosomal protein lateral stalk subunit P0 (RPLP0). Values were then compared using a Students' t-test in GraphPad Prism 8 software.

GENE (Mouse)	FWD/REV	Primer Sequence (5'-3')
RPLP0	FWD	AAGAACACCATGATGCGCAAG
	REV	TTGGTGAACACGAAGCCCA
Pcdh-γ C3	FWD	CTCAGTGTGACTGATCTGGATG
	REV	GAGGGAAGAAGTCAGGCTAAAG
Pcdh-γ C5	FWD	GCCTTATTGGAGGATGACTCTG
	REV	GTACTGTTGCTGTGGAGGATAG
Pcdh-γ constant domain	FWD	TGGCCCAACAACCAGTTTGA
	REV	AGGGTAAACTGGGGTCCGTA

Table 2.1: *PCR primers used in qRT-PCR reactions.* RPLP0, ribosomal protein lateral stalk subunit P0; FWD, forward; REV, reverse.

2.2.3.2. Immunohistochemistry and quantification

Footpads, DRGs, and sciatic nerves were harvested from euthanized mice and placed into an appropriate fixative solution (footpads: paraformaldehyde, L-lysine, and sodium m-periodate; DRGs and nerves: Modified Zamboni's) immediately post-mortem. Samples were fixed in solution for 12-24 h at 4°C. After fixation, samples were then rinsed twice with either 0.1 M Sorrenson's phosphate buffer (footpads) or PBS (DRGs, nerves), and cryoprotected in a solution of 20% glycerol/0.1 M Sorrenson's (footpads) or 20% glucose/PBS (DRGs, nerves) and kept at 4°C overnight. Tissue was then dried off thoroughly with a Kimwipe and embedded in OCT blocks and frozen to prepare for cryostat sectioning.

Once frozen, tissue was cross sectioned at 25 μm (footpads) or 12 μm (DRG, nerve). Sciatic nerves were cut transversely. Sections were mounted onto SuperFrost Plus slides (Thermo Fisher Scientific, Waltham, MA) and allowed to dry overnight.

Footpad sections underwent antigen retrieval in 65°C Tris-EDTA buffer for 90 min to encourage antigen presentation of PGP9.5. Sections were blocked in a solution of 10% normal goat serum, 1% bovine serum albumin (BSA), 0.3% Triton-X100 and PBS for 1 h at RT. Sections were then incubated in a solution of 0.1% BSA, 0.04% EDTA, 0.3% TritonX100, 1% normal goat serum, and the primary antibody (1:1000 rabbit anti-PGP9.5, EnCor Biotech. Inc., Gainesville, FL) overnight at 4°C. PGP9.5 was chosen as it has been shown to be a robust marker for visualizing epidermal sensory fibres (Cheng et al., 2010). Following primary incubation, sections were then rinsed 3 times for 5 min in PBS, then incubated in the same solution as above, but with a secondary antibody instead of the primary (1:1000 goat anti-rabbit AlexaFluor 546) for 1 h at RT. Sections were rinsed in PBS for 3 x 5 min, then mounted with Vectashield Mounting Media, cover slipped, and sealed.

DRG and nerve sections were blocked in a solution containing 10% normal goat serum, 1% BSA, 0.03% Triton, and 0.05% Tween20 for 1 h at RT. Sections were then incubated in the primary antibodies (1:200, mouse anti-NF200, Millipore Sigma, Burlington, MA, and 1:500 rabbit anti-Pcdh-γ, Synaptic Systems, Gottingen, GER) in 1% normal goat serum, 0.1% BSA, 0.03% Triton, and PBS overnight at 4°C. Slides were rinsed for 3 x 5 min in PBS, then incubated in the secondary solution (1:100 Alexa Fluor goat anti-rabbit 488, 1:200 goat anti-mouse 546, Invitrogen) for 1 h at RT. Sections were then rinsed 3 x 5 min and mounted with Vectashield, cover slipped, and sealed. Footpads, DRGs and sciatic nerves were imaged using a Leica SP5 confocal microscope.

Corrected total cell fluorescence (CTCF) analyses were conducted on sciatic nerve section. Four randomly selected regions were measured per section of tissue, and the area, integrated density, and mean grey value were measured using ImageJ. CTCF values were measured using the following equation,

$$\text{CTCF} = integrated\ density - (area\ of\ selection * mean\ fluorescence\ of\ background),$$

Values were then compared between groups and appropriate statistics were applied.

2.2.3.3. Western blot

Protein was extracted from DRG, sciatic, and footpad tissue, and quantified using the Bradford assay. 25 μg of denatured protein lysate was loaded into each well of a gel. The gel was then run at 75 V until the protein bands reach the 7.5% resolving gel, at which point the voltage was adjusted to 100 V until the bands reached the bottom of the gel. Proteins were transferred to

a PVDF membrane over 90 m at 100 V. Membranes were then blocked in a solution containing 5% BSA in TBST. Membranes were incubated for the presence of Pcdh-γ (1:1000 rabbit anti-Pcdh-γ, Synaptic Systems) in 5% BSA/TBST overnight at 4°C. Beta-actin was used as a loading control (1:3000 rabbit anti-β-actin primary, Abcam, Cambridge, UK). Blots were visualized using goat anti-rabbit HRP (1:3000, Life Technologies Carlsbad, CA).

2.2.4. *Peripheral Nerve Injury*

Mice were anaesthetized using inhaled 2% isoflurane. When the mouse reached surgical plane, the right hind leg where the incision was to be made was shaved and disinfected. A small incision just below the femur and adjacent to the sciatic notch was made. The entire sciatic nerve trunk was crushed at mid thigh, for 15 seconds in two orthogonal orientations (ie. 90°) using forceps. The wound was then sutured and checked twice a day post surgery. Mice were administered buprenorphine as an analgesic twice a day for three days for postoperative pain management.

2.2.5. *Cell Culture*

DRGs were harvested and placed into cold L-15 media (Gibco, Waltham, MA). DRGs were then rinsed using fresh L-15 and placed into 1% collagenase D (Roche Applied Science, Budapest, HUN) in L-15 and incubated at 37°C for 30 m. Initially a concentration of 0.1% collagenase D was used, but a better yield was found with a 1% solution. DRGs were then dissociated into a single cell suspension through trituration. This suspension was centrifuged at 800RPM for 6min at RT. The pellet was resuspended in fresh L-15 and poured through a 70 μm mesh. Suspension was centrifuged again, and the pellet resuspended in fresh L-15. Suspension was poured through 15% BSA gradient and centrifuged to separate out tissue debris and

Schwann cells (supernatant) from the neurons (pellet). The pellet was then resuspended in fresh media (Dulbecco's Modified Eagle Medium (DMEM, Gibco), N-2 supplement (Gibco), NGF (Invitrogen), cytosine-β-arabinofuranoside (Sigma-Aldrich, St. Louis, MO), penicillin, and streptomycin). For siRNA mediated knock down experiments, media was split across two treatment groups: Scr (scrambled sequence siRNA), and Pcdh-γ (Pcdh-γ sequence siRNA). 20nM siRNA (Qiagen, Hilden, GER) was mixed with HiPerfect Transfection Reagent (Qiagen) 15 m prior to mixing with media. Equal amounts of the cell suspension were distributed to each well of a 4-well chamber slide (Fisher, Waltham, MA) containing 1 ml of prepared media. Chambers were pre-treated with 0.1% poly-l-lysine and 10 µg/ml laminin. Chambers were then incubated at 37° for 24 h (injured neurons) or 72 h (naïve neurons). Neurons tend to grow quickly following an injury, so we kept this incubation period shorter to limit axon density for analysis.

2.2.6. *Neuronal outgrowth, intersection analysis, Sholl analysis*

Using the procedure above, a dissociated DRG culture was created and allowed to grow on 4-well chamber culture plates for 24 h (injured neurons) or 72 h (naïve neurons) at 37°C following plating. Cells were then fixed using a 4% PFA solution and blocked with 5% BSA and 0.3% TX-100 in PBS for 1 h at RT. Cells were then incubated in 3% BSA, 0.3% TX-100 and the primary antibody (1:200 rabbit anti-NF200, Sigma) for 75 m at RT. Cells were then rinsed 3 x 5 min with PBS and incubated in the secondary antibody solution (1:200 Alexa Fluor goat anti rabbit 488, Invitrogen) with 3% BSA and 0.3% TX-100. Cells were then mounted using Vectashield mounting media with DAPI and were imaged using a Zeiss AxioScope microscope at 20X. Each neuron was imaged alone whenever possible to maximize accuracy of the neurite outgrowth software. Neurites were analyzed using the Neuromath software (Rishal et al., 2013,

https://biii.eu/wis-neuromath), which calculates the length, number of sprouting neurons, and branching complexity of each image.

Intersection experiments followed the same procedure as above, but one side of the animal was given a sciatic nerve crush, providing both injured and contralateral (uninjured) DRGs. Animals recovered for 72 h (see section 2.2.4). L4-6 DRGs from both sides were harvested from these animals, as these are the DRGs that supply the majority of axons within the sciatic nerve. DRGs were cultured for 24 h, processed, and imaged. Images were processed using the Neuromath software, which generates a MATLAB file containing a tracing of the neurites measured for each image. This tracing was overlaid with the original image in Photoshop (Adobe, San Jose, CA), and neurite self crossings were labeled manually. Only neurites that had a signal large enough to be detected by the Neuromath software were included.

Neighbour intersection analysis was conducted on randomly selected images that contained two neurons that exhibited neurites growing towards the other cell body and were only included if the length of the longest neurite could intersect with the longest neurite emerging from the other neuron.

Sholl analyses was carried out using ImageJ (NIH, Bethesda, MD). MATLAB neurite tracings from Neuromath were imported into ImageJ and analyzed using the Sholl plugin. A shell size of 10 µm was used. The soma centres were identified manually.

2.2.7. *siRNA in vivo knockdown model*

5 µL of Pcdh-γ siRNA or a scrambled negative control sequence siRNA were combined with HiPerfect Transfection Reagent (Qiagen) for 20 min at RT prior to injections. Saline was added to increase the volume of bolus injected into the animal. Following the peripheral nerve injury protocol described in section 2.2.4 and prior to suturing the wound, 50 µL of the siRNA

solution was administered directly to the nerve. The wound was sutured, and a conductive gel was applied to the lateral and medial regions of the thigh, maintaining separation between gel applications to prevent short circuiting. Electrodes were held in contact with the gel, with the negative electrode positioned on the lateral side of the leg (side of incision), and the positive electrode placed on the medial side of the leg. Five 25 V pulses lasting 50 ms each in duration were given at 1 Hz, administered using an ECM 830 Electro Square Porator ™ unit. 20 µL (3 µL siRNA) of the siRNA solution was also injected into the ipsilateral footpad subcutaneously. This region was electroporated as above, with the negative electrode place on the ventral side of the foot (site of injection), and the positive electrode placed on the dorsal side of the foot. Injections were repeated at both sites 3 times a week for 28 days (12 injections). Injections to the nerve were done through the incision site, as the sutures were not reopened at any time.

2.2.8. *Behavioural analyses*

Prior to all behavioural testing, mice were acclimated to both the Hargreaves and Von Frey apparatuses. Animals were tested on Day 0 prior to the injury, Day 14, and Day 28 prior to harvesting.

Mechanical hypersensitivity was assessed using Von Frey monofilaments to quantify mechanical allodynia in mice. Mice were separated and placed on a wire mesh platform through which the center of each hind paw could be stimulated using Von Frey fibres. Fibres ranging from 0.4 g – 4 g were used. Starting from the lowest weight fibre, the fibre used to elicit paw withdrawal and associated pain behaviours (paw licking) was assessed. The fibre that elicits a response 75% of the time was recorded as the mechanical pain threshold. If there was no response after 5 applications of the fibre, the next weight up was tested until a response was

given 75% of the time. Testing did not go above 4 g. If there was no response at 4 g, the recorded withdrawal threshold was 4 g.

Thermal sensitivity was assessed with the Hargreaves apparatus. Mice were placed on a plexiglass platform, with a radiant heat source underneath. The heat source was applied to the middle of the hind paw, and the latency to withdraw the paw was recorded (in seconds, Christie et al., 2014). Withdrawal latency was averaged from 3 trials per footpad. In order to prevent damage to the animals' paw, each individual trial did not exceed 20 seconds of heat exposure. Paws were alternated and animals randomized to allow footpad sensation to normalize.

2.2.9. *Nerve Conduction analyses*

Electrophysiological measurements were collected using a Cadwell Sierra® Ascent™ base unit and software (version 1.1.143), a 2-channel amplifier, and electrical stimulator, sampled at 16 bit at 100 kHz. Animals were tested on Day 0 prior to the injury, Day 14, and Day 28 prior to harvesting. Motor and sensory multi-fibre conduction studies were performed on mice under isoflurane anaesthesia. Near nerve temperature was maintained at 37°C via a heat lamp for the duration of the study. Platinum subdermal electrodes were placed at appropriate stimulation and recording sites. Compound motor action potentials (CMAPs) were recorded at the interosseous foot muscles, while supra-maximally stimulating the sciatic notch and the knee to calculate the nerve conduction velocity (CV) between the two points. The signal was filtered between 10 and 10 kHz. Sensory nerve action potentials (SNAPs) were recorded at the knee and stimulated from sensory interosseous branches in the foot. SNAPs were averaged over 10 consecutive recordings and was filtered between 10 and 2 kHz. Distances between electrode sites were recorded manually and inputted into the Sierra® Ascent ™ computer software to generate velocities from the collected waveforms.

2.2.10. *Statistical Analyses*

Statistical analyses were carried out using Microsoft Excel (Microsoft, Redmond, WA, https://www.office.com/), GraphPad Prism 8 (GraphPad Software, San Diego CA, https://www.graphpad.com/), JASP (JASP, University of Amsterdam, NLD, https://jasp-stats.org/), and MATLAB software (Mathworks, Natick, MA, https://www.mathworks.com/products/matlab.html) using parametric (Student's t-tests and two-way ANOVAs) and non-parametric tests (Wilcoxon and Mann-Whitney) as appropriate. Comparisons were checked with non-parametric tests if the sample size was less than 4, or if the distribution was not normal. The null hypothesis was rejected if $p < 0.05$. Post hoc power analyses were completed using G*Power with an α threshold = 0.05 (Faul et al., 2007).

2.3. Results

2.3.1. *Pcdh-γ is expressed in the mammalian PNS*

Since the sequence of the constant region of Pcdh-γ is unavailable online, and the γ C3 and γ C5 exons are ubiquitously expressed in all cells that express Pcdh-γ, (Kaneko et al., 2006), we designed primers to both exons for our initial experiments. We conducted systematic analyses on the peripheral sensory nerve cell soma (DRG), axon (sciatic nerve), and terminal endings (footpad). Using qRT-PCR, we tested for the expression of these two exons, compared to a RPLP0 housekeeping gene. Positive expression was seen in each tissue type for both exons (Figure 2.2), suggesting mRNA is present throughout the cell from the soma to the terminal endings.

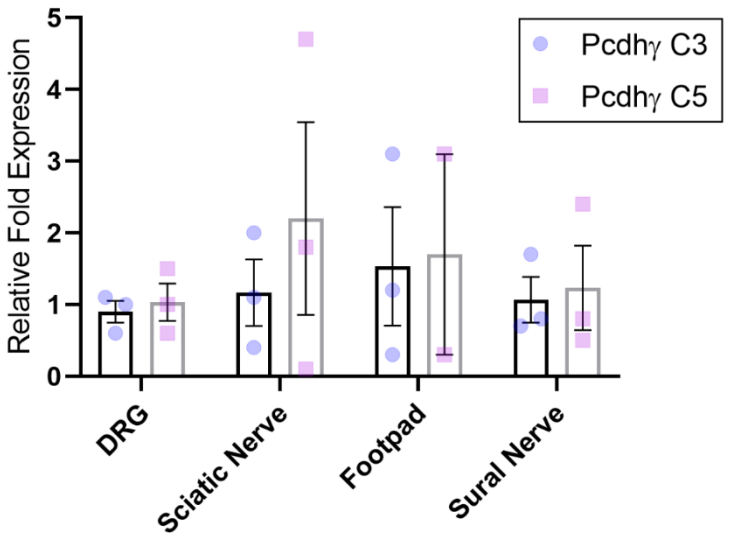

Figure 2.2: *Expression of Pcdh-γ exons C3 and C5 are present throughout mouse peripheral sensory neurons.* Pcdh-γ exons C3 and C5 are expressed at all levels of the neuron compared to a RPLP0 housekeeping gene. Error bars indicate ±SEM. n = 3.

Using a pan-Pcdh-γ antibody, which labels all Pcdh-γ isoforms by targeting the constant region, immunohistochemical experiments reveal wide Pcdh-γ expression in both mouse (Figure 2.3) and rat (Figure 2.4) DRGs. Interestingly, Pcdh-γ appears to be expressed widely across DRG neurons in both animals and is not just limited to the larger caliber neurons expressing the high molecular weight neurofilament (200kD, NF200). Arrows point to cells negative for NF200 expression but positive for Pcdh-γ expression. Further testing to examine co-localization with peptidergic and non-peptidergic neuronal markers are needed. To rule out the possibility of non-specific staining, we also conducted negative primary controls where the primary antibody was omitted (Figure 2.3H, 2.4H, K). This showed some non-specific fluorescent staining, but at threshold levels which are lower (Figure 2.3B, top right)., indicating non-specific secondary background staining.

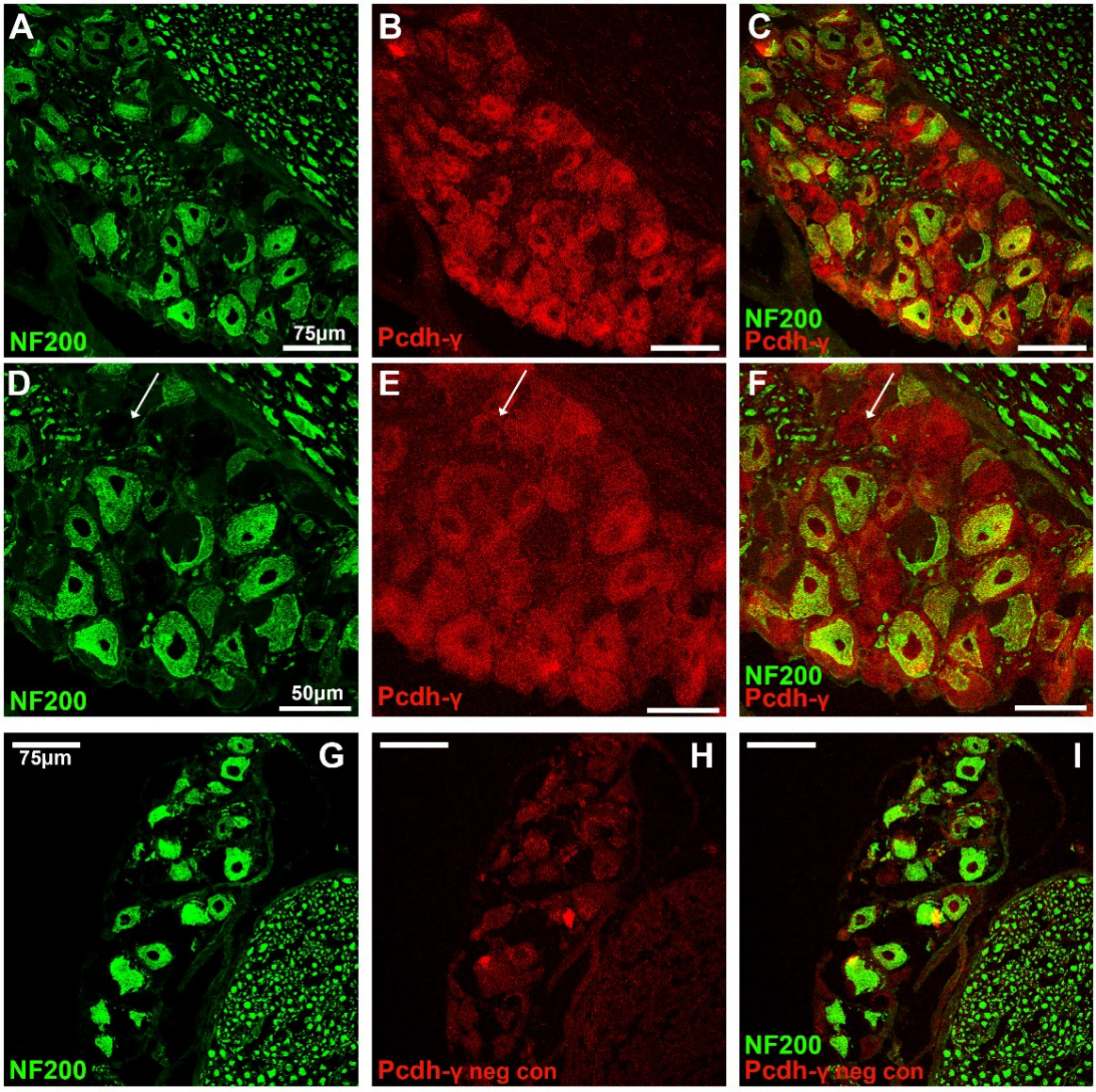

Figure 2.3: *Pcdh-γ is expressed widely in mouse DRG neurons.* Transverse section of mouse DRG immunostained for NF200 (green, A, D, G), and Pcdh-γ (red, B, E). Colocalization is shown in overlay (C, F, I). Arrow indicates small diameter neuron negative for NF200, but positive for Pcdh-γ expression. H, I: Pcdh-γ primary negative control. A-C: imaged at 40X. D-F, same region as A-C, imaged at 63X. G-I imaged at 40X. Scale bars listed in A, D, G for respective magnifications. NF200, neurofilament heavy subunit.

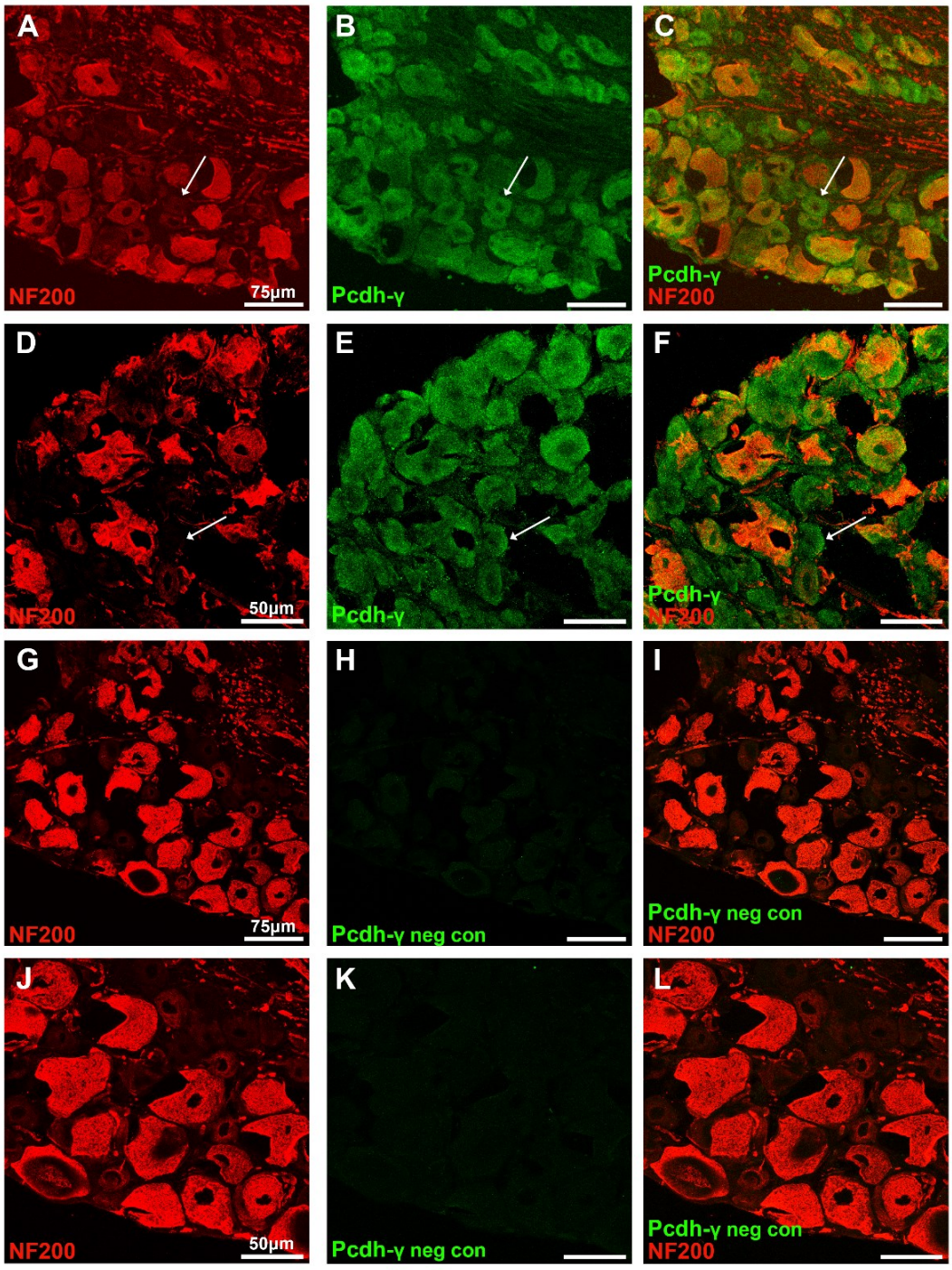

Figure 2.4: *Pcdh-γ is expressed widely among neurons of rat DRG.* Transverse section of a rat DRG immunostained for NF200 (red, A, D, G, J), and Pcdh-γ (green, B, E). Colocalization is shown in overlay (C, F). Arrow indicates small diameter neuron negative for NF200, but positive for Pcdh-γ expression. G-L: Pcdh-γ primary negative control. A-C, G-I: imaged at 40X. D-F, J-L: imaged at 63X. Scale bars listed in A, D, G, J for respective magnifications. NF200, neurofilament heavy subunit.

To investigate whether there was fluorescent signal in the nerve, we used a corrected total cell fluorescence analysis (CTCF) on two sections, taking four separate measurements to maximize the sampling from the tissue. We saw an increase in the Pcdh-γ signal in the sciatic nerve compared to a negative control where the primary antibody was omitted (n = 4; t-test; p = 0.002, Figure 2.5). Although the sample size was small, this suggests that Pcdh-γ is expressed primarily in the soma and may be present at lower levels in the axons. It is unlikely to be present in the Schwann cells from this image. Staining of the footpad for Pcdh-γ identified substantial staining in the keratinocytes without clear axon localization (Figure 2.6).

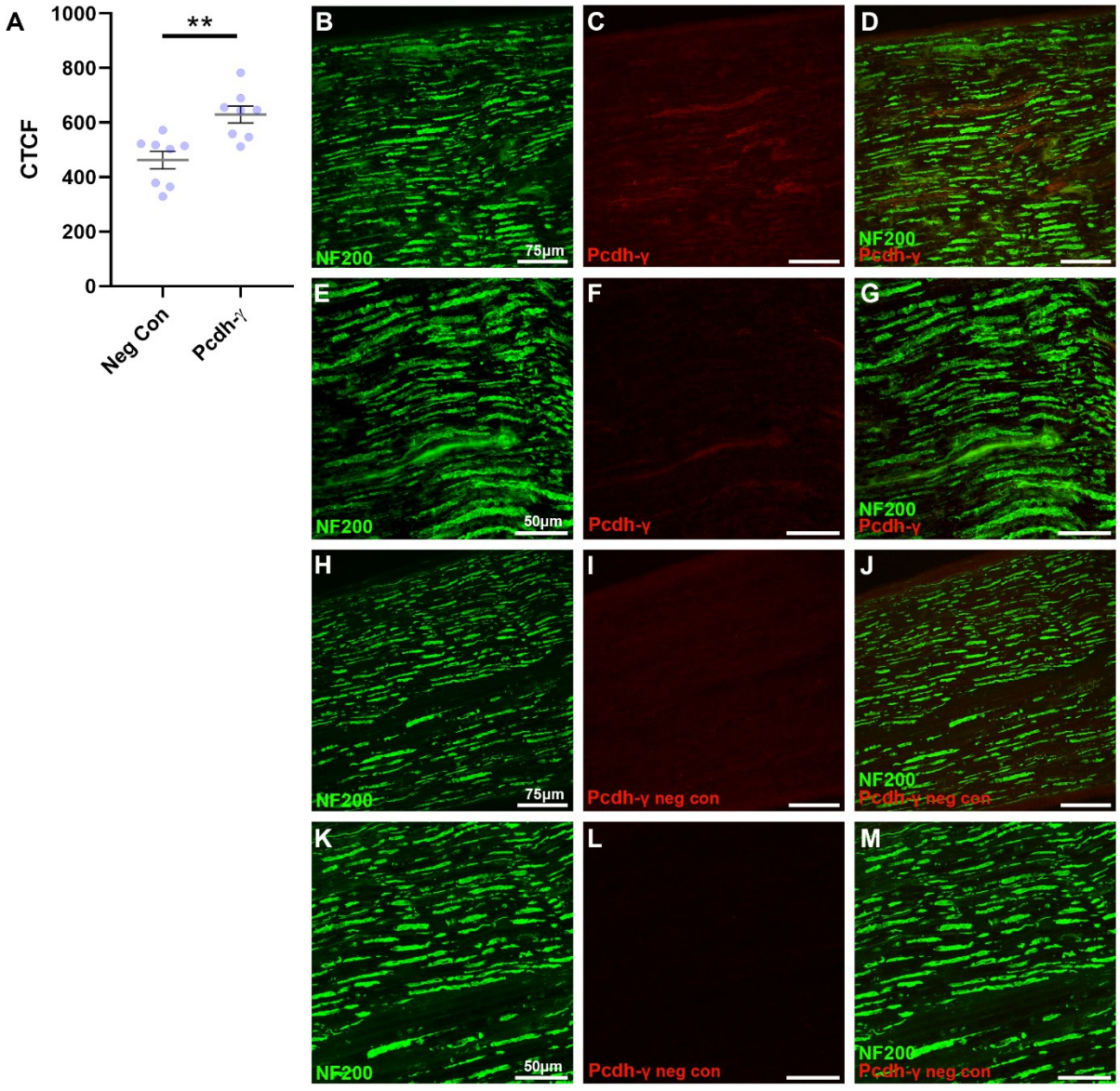

Figure 2.5: *Pcdh-γ expression in mouse sciatic nerve.* Longitudinal sections of sciatic nerve immunostained for NF200 (green (B, E, H, J) and Pcdh-γ (red, C, F). Overlay shown in right column (D, G, J, M). Pcdh-γ negative control shown in I, L. Corrected total cell fluorescence (CTCF) quantification shows a small but significant amount of Pcdh-γ staining in sciatic nerve when correcting for background fluorescence (±SEM, n = 4; t-test; $p = 0.002$). B-D, H-J: imaged at 40X. E-G, K-M: imaged at 63X Scale bars listed in B, E, H, K for respective magnifications. NF200, neurofilament heavy subunit. ** = $p < 0.01$.

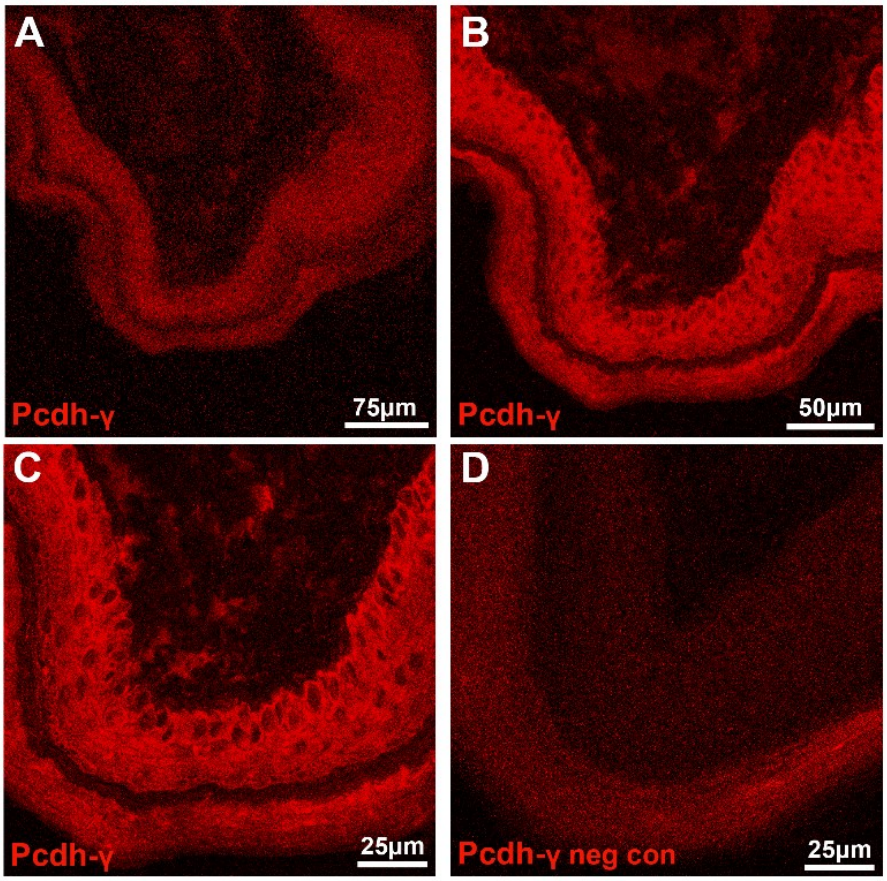

Figure 2.6: *Pcdh-γ expression in mouse footpad.* Cross sections of skin stained for Pcdh-γ (red). The same region of dermis and epidermis imaged at 40X (A), 63X (B), and 100X (C, D). D shows a negative control in absence of a primary antibody to Pcdh-γ in order to illustrate the secondary background staining.

2.3.2. *Pcdh-γ expression drops at 36hpi, but returns to baseline levels by 72hpi*

Following a peripheral nerve injury many molecular expression patterns are altered in response, in which constitutive molecules are downregulated, and regeneration-associated genes are upregulated (Verge et al., 1996; Zochodne, 2012). Many of these upregulated molecules are developmentally relevant, such as neurotrophic factors (Verge et al., 1996), and other important guidance molecules such as the DCC or Unc5H receptors (Webber et al., 2011). Due to the role of Pcdh during development and its effect on guiding growing neurites shown in the CNS (Chen

et al., 2012; Ing-Esteves et al., 2018), we investigated whether Pcdh-γ was upregulated following an injury to assist in guiding the regenerating neurites. We induced a sciatic nerve injury in mice and examined mRNA and protein levels at several time points post injury (Figure 2.7). We noted a consistent drop in the Pcdh-γ signal in both the C3 and C5 mRNA in the ipsilateral DRG compared to contralateral DRGs (Mann-Whitney; Pcdh-γ C3 36 h, $p = 0.02$, Figure 2.7A, Pcdh-γ C5 36 h, $p = 0.03$, Figure 2.7B). However, despite a trend toward less protein at 36h following a nerve injury, these changes were not significant. (DRG: Wilcoxon; Con vs. 36 h; $p = 0.50$, 36 h vs. 72 h, $p = 0.25$, Figure 2.7D. Footpads: Wilcoxon; Con vs. 36 h; $p = 0.99$, 36 h vs. 72 h; $p = 0.99$, Figure 2.7E. Sciatic nerves: Wilcoxon; Con vs. 36 h; $p = 0.10$, 36 h vs. 72 h; $p = 0.20$, Figure 2.7F). To check whether these non-significant results were because of the low sample size, power analyses were conducted. With an $\alpha = 0.05$, a strong effect size of 0.84 and 2.45 were calculated for the DRGs and sciatic nerves respectively, requiring an n = 21 and 5 replicas respectively to achieve significance based on the values obtained. The footpads however had a very low effect size of 0.005 and would require over 460,000 replicates to see a statistical difference. Based on this, we can cautiously interpret the decreases seen in the DRGs and sciatic nerves as an effect on the Pcdh-γ protein due to the injury, and the footpads exhibit no difference following injury. Interestingly, the Pcdh-γ levels all returned to baseline by 72 h post injury. This study did not look past 72 h however, which may provide further temporal information.

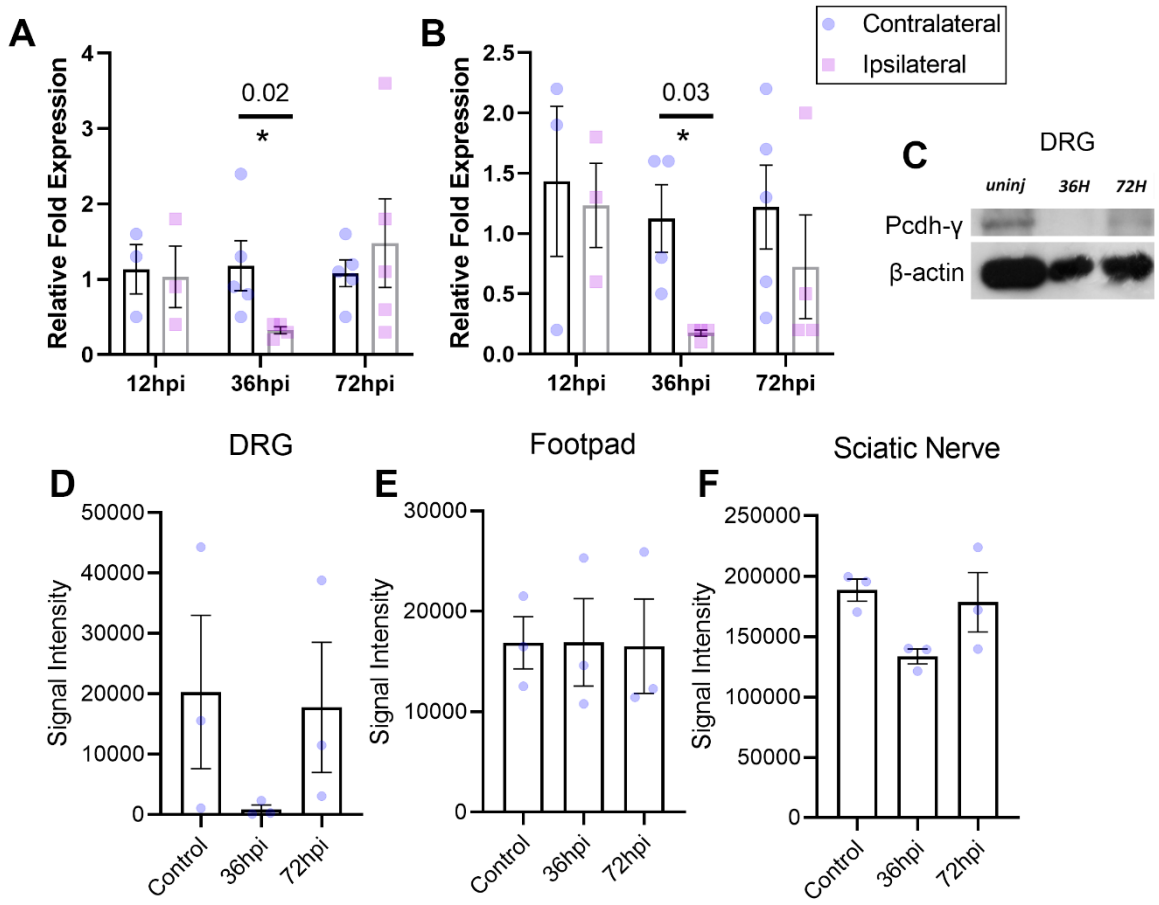

Figure 2.7: *Pcdh-γ RNA expression falls at 36 h following peripheral nerve injury and returns to baseline levels by 72 h.* A, B: relative fold expression of mRNA levels of Pcdh-γ exons C3 (A) and C5 (B) both show decreases in expression at 36 h post injury compared to the contralateral side, but approach normal values at 72 h post injury (n = 4; Mann Whitney; Pcdh-γ C3 36 h Con vs. Ipsi p = 0.02, Pcdh-γ C5 36 h Con vs. Ipsi p = 0.03,). There were no significant changes in the DRG, footpad, and sciatic nerve western blots despite a similar trend for a protein decline at 36h in the DRG and sciatic nerve samples. (C, D, n = 3; Wilcoxon; Con vs. 36 h p = 0.50, 36 h vs. 72 h, p = 0.25. E, n = 3; Wilcoxon; Con vs. 36 h, p = 0.99, 36 h vs. 72 h, p = 0.99. F, n = 3; Wilcoxon; Con vs. 36 h, p = 0.10, 36 h vs. 72 h, p = 0.20). Non-significant results may be a result of low sample size, see text for power analysis. Error bars represent ±SEM. DRG, dorsal root ganglion.

2.3.3. *Pcdh-γ knockdown increases neurite extension in vitro*

There is abundant support for a role of Pcdh-γ in arborization (Garrett et al., 2012; Lefebvre et al., 2012; Suo et al., 2012), but there has been no investigation of this role of protocadherins and their impact on axons in the PNS. Following other studies in our lab (Christie

et al., 2014; Duraikannu et al., 2018; Krishnan et al., 2018; Poitras et al., 2019), we designed a non-viral small interfering RNA (siRNA) to knock down functional Pcdh-γ in adult sensory neurons. Due to the diversity of isoforms in the Pcdh-γ gene, we designed our siRNA against the constant, cytoplasmic region of the Pcdh-γ as this region is common across all translated Pcdh-γ proteins (sequence provided by the Lefebvre lab, Kohmura et al., 1998; Wu and Maniatis, 1999). This strategy has been shown to be effective in other experiments as well (Dallosso et al., 2009). Using adult sensory neuron cultures, we incubated naïve mouse DRG neurons in the presence of either the Pcdh-γ siRNA (Pcdh-γ KD), or a scrambled sequence siRNA (Scr). These cultures were incubated for 72 h to allow for sufficient neurite extension. qRT-PCR tests show a significant knockdown of the Pcdh-γ gene after 72 h incubation (Figure 2.8A) compared to the Scr treatment (Mann-Whitney; n = 3; p = 0.04, Scr relative fold expression = 1.20, Pcdh-γ = 0.17).Following neurite extension, cells were fixed and processed for NF200 expression to label neurites. Images were taken of each individual neuron for processing using the Neuromath software (Rishal et al., 2013), which processes neurons for neuron count, neurite length, branching points, and other parameters. Sprouted neurons treated with Pcdh-γ siRNA showed a significant increase in the average overall neurite extension (Welch's t-test; Pcdh-γ KD = 4382±231 a.u. (±SEM), 95% CI [3646, 5119]; Scr siRNA = 2560±409, [1256, 3864]; p = 0.01, Figure 2.8B). Further, sprouted Pcdh-γ KD neurons had more branching points (Pcdh-γ KD = 127±7; Scr siRNA = 70±11; p = 0.007, Figure 2.8D), suggesting an increase in complexity. Pcdh-γ KD neurons also exhibited a trend towards hosting the longest branch (Pcdh-γ KD = 372±27 a.u.; Scr siRNA = 281±29; p = 0.06, Figure 2.8C), but this failed to reach significance. Finally, 55% of neurons sprouted following Pcdh-γ KD, compared to 42% that sprouted following Scr treatment (Pcdh-γ KD = 55%; Scr siRNA = 42%; p = 0.15, Figure 2.8E). Figure

2.8F show example micrographs of the outgrowth of neurons treated with Pcdh-γ siRNA (top row) and Scr siRNA (bottom row).We also measured average neurite outgrowth on neurons that had experienced a sciatic nerve crush prior to culturing (Injured, Inj), compared to contralateral neurons that did not experience a crush (Contralateral, Con). Injured cultures were incubated for 24 h post-plating as injured neurons tend to have more robust outgrowth following an injury. To maintain accuracy in our outgrowth analysis, we elected to fix cells after 24 h to limit axon density for analysis by the software. What we found was unexpected: the increased neurite outgrowth seen in naïve animals treated with Pcdh-γ siRNA (Figure 2.8B) was lost following an injury (Figure 2.8G). This was the case for both injured and contralateral Pcdh-γ KD neurons (t-test, Pcdh-γ KD Inj = 2630±337 a.u., [1557, 3703]; Scr Inj = 3044±197, [2416, 3672], p = 0.34); Pcdh-γ KD Con = 3096±246, [2315, 3878]; Scr Con = 3266±487, [1715, 4817], p = 0.77, Figure 2.8G). However, we found that injured neurons had longer branches (Figure 2.8H; t-test, Pcdh-γ KD Inj = 374±9a.u., [347,401]; Pcdh-γ KD Con = 279±12, [240, 318], p = 0.001; Scr Inj = 346±10, [313, 380]; Scr Con = 273±24, [197, 349], p = 0.046), but only the Pcdh-γ KD Inj had significantly less branching points (Figure 2.8I; t-test, Pcdh-γ KD Inj = 78±13, [38, 118]; Pcdh-γ KD Con = 125±12, [87, 163], p = 0.036); Scr Inj = 110±13, [70, 151]; Scr Con = 148±26, [64, 232], p = 0.26, Figure 2.8G). These two measures could be interpreted together as more directed growth following injury, with neurons sending out fewer neurites, but investing more energy into growing them further.

It should be noted however, that considering the drop seen in Pcdh-γ mRNA and possibly protein levels following an injury (see section 2.3.2), it is possible that the Pcdh-γ levels are naturally lower in injured animals compared to naïve animals. Though we see levels starting to increase by the time of harvesting and culturing (72 hpi), it is possible the overall level of Pcdh-γ

is naturally lower, so the Scr neurons would have approximately the same amount of Pcdh-γ remaining as the neurons treated with Pcdh-γ siRNA.

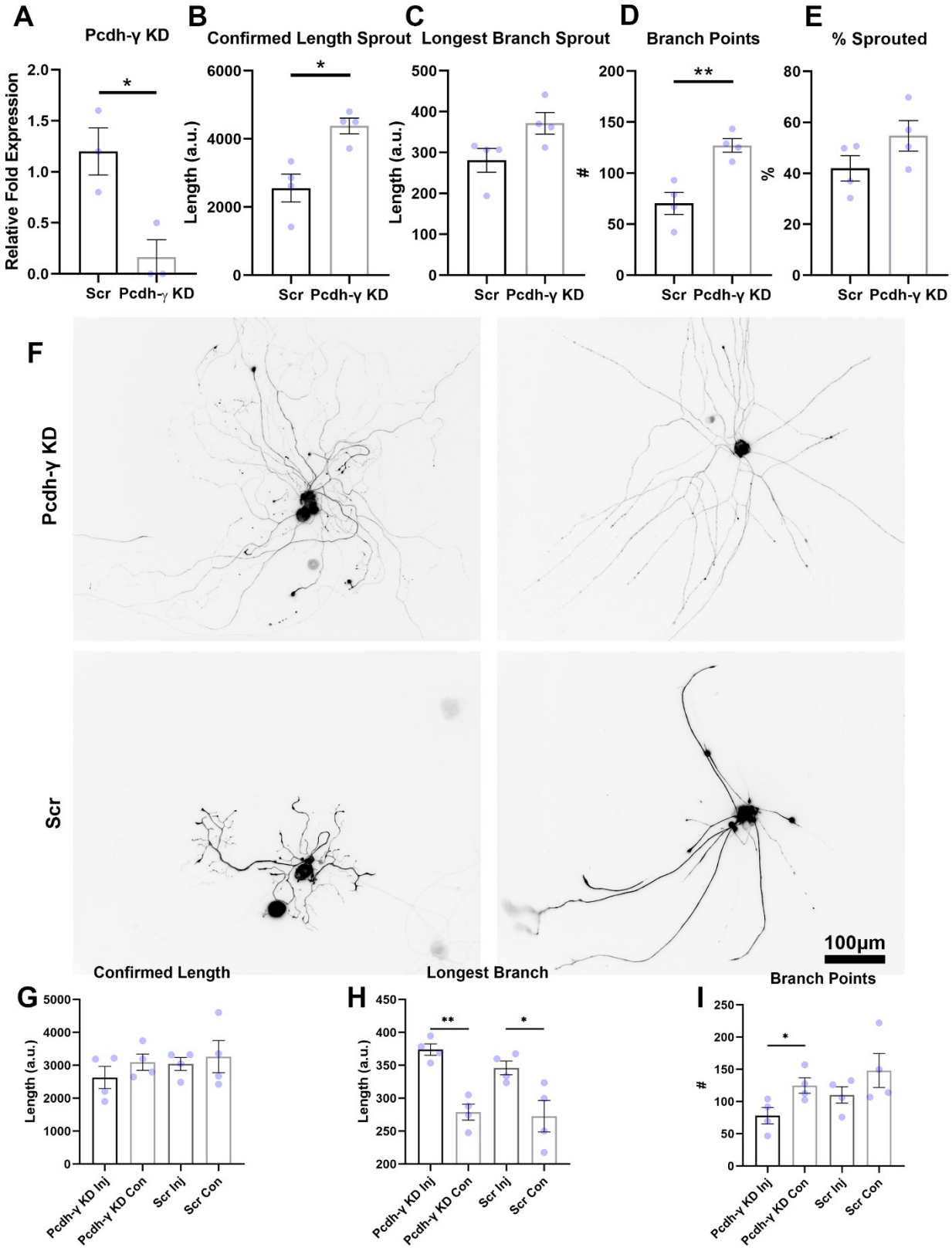
A
Pcdh-γ KD
Relative Fold Expression
2.0
1.5
1.0
0.5
0.0
*
Scr
Pcdh-γ KD
B
Confirmed Length Sprout
Length (a.u.)
6000
4000
2000
0
*
Scr
Pcdh-γ KD
C
Longest Branch Sprout
Length (a.u.)
500
400
300
200
100
0
Scr
Pcdh-γ KD
D
Branch Points
#
200
150
100
50
0
**
Scr
Pcdh-γ KD
E
% Sprouted
%
80
60
40
20
0
Scr
Pcdh-γ KD
F
Pcdh-γ KD
Scr
100μm
G
Confirmed Length
Length (a.u.)
5000
4000
3000
2000
1000
0
Pcdh-γ KD Inj
Pcdh-γ KD Con
Scr Inj
Scr Con
H
Longest Branch
Length (a.u.)
450
400
350
300
250
200
**
*
Pcdh-γ KD Inj
Pcdh-γ KD Con
Scr Inj
Scr Con
I
Branch Points
#
250
200
150
100
50
0
*
Pcdh-γ KD Inj
Pcdh-γ KD Con
Scr Inj
Scr Con

Figure 2.8: *Pcdh-γ KD in vitro increases neurite extension and branching points following 72 h incubation, but this effect is lost in pre-injured neurons following a 24 h incubation.* A: qRT-PCR results showing knockdown of Pcdh-γ following administration of Pcdh-γ siRNA or a scrambled control (Scr) (n = 3; Mann-Whitney; $p = 0.04$). Pcdh-γ KD neurons exhibited longer average neurite growth (B, n = 4; t-test; $p = 0.01$), and more branching points (D, n = 4; t-test; $p = 0.007$). They showed a trend towards having a longer branch, as well as sprouting more often (C, $p = 0.06$, E, $p = 0.15$). F: Representative images of Pcdh-γ KD neurons (top row) or neurons treated with a Scr siRNA (bottom row). Neurons with a confirmed outgrowth of a value close to the mean of their group are shown in this image. G, H, I show average confirmed length, longest branch, and branching point results of neurons taken animals that had experienced a peripheral nerve injury 72h prior to culturing (n = 4). Neurons were taken from either the ipsilateral side of the injury 72h (Inj), or the contralateral side (Con). Neurons were incubated for 24h as opposed to 72h in A-F. Injury appears to prevent the increased neurite growth in all groups, but Inj neurons (Pcdh-γ and Scr) appear to show longer branches (t-test; Pcdh-γ KD Inj vs. Pcdh-γ KD Con $p = 0.001$, Scr Inj vs. Scr Con $p = 0.046$), and in the case of Pcdh-γ KD neurons, less branching points (t-test; Pcdh-γ KD Inj vs. Pcdh-γ KD Con $p = 0.036$. Scr Inj vs. Scr Con $p = 0.26$). * = $p < 0.05$, ** = $p < 0.01$. Error bars indicate ±SEM. a.u., arbitrary units.

Tracings of 20 randomly selected cells per experiment with the injured animals were selected for Sholl analysis (Pcdh-γ KD Con, Scr Con n = 4, Pcdh-γ KD Inj, Scr Inj n = 5). These cells were incubated for 24 h following plating. A Sholl analysis involves counting neurite crossings of shells, which are concentric circles placed every 10 μm from the centre of the soma (see Figure 2.9A, B). These numbers were then averaged per experiment and reported in Figure 2.9C, D. A two-way ANOVA identified a main effect of injury ($F(1, 170) = 19.317$, $p < 0.001$). Bonferroni pairwise comparisons indicated that this effect is likely driven by the difference between the Pcdh-γ KD Inj group and the Pcdh-γ KD Con group (t-test; $p = 1.0 \times 10^{-4}$). Notably, the Scr Con group was also significantly different from the Scr Inj group (t-test; $p = 0.02$). This is reflected in the area under the curve analysis in Figure 2.9D (t-test; Pcdh-γ KD Con = 367.5±27.1, Pcdh-γ KD Inj = 224.7±16.3, $p = 0.004$, Scr Con = 311.6±22.2, Scr Inj = 230.6±20.1, $p = 0.046$). There was no significant difference between the siRNA treatments ($F(1, 170) = 0.212$, $p = 0.65$). These data suggest it is the injury that decreases the number of shell crossings at early lengths of outgrowth and the effect is potentiated if Pcdh-γ KD occurs,

pointing to lessened proximal outgrowth and complexity in the setting of longer overall growth. There was no significant difference between groups when the injury condition was constant (t-test; Scr Con vs. Pcdh-γ KD Con $p = 0.31$; Scr Inj vs. Pcdh-γ KD Inj $p = 0.78$).

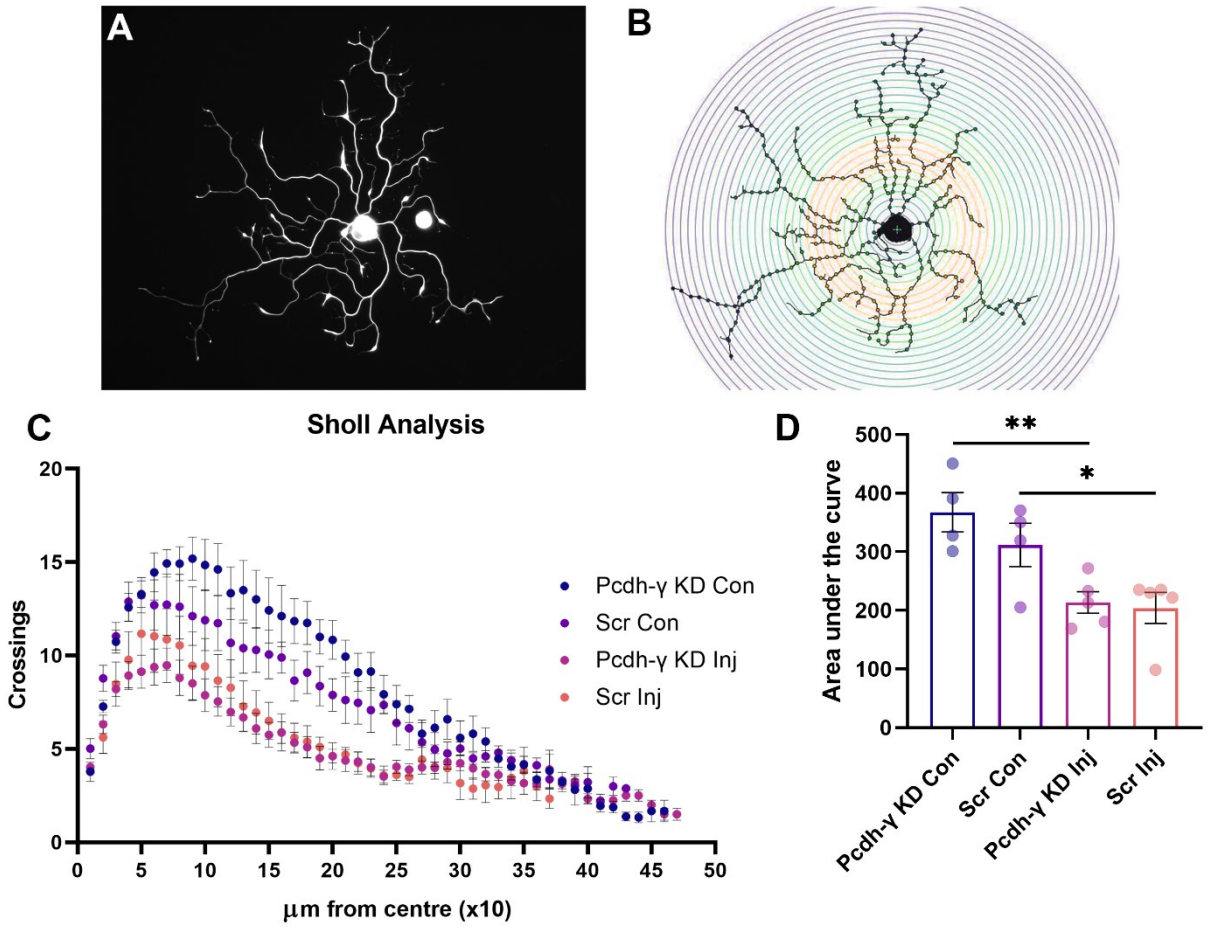

Figure 2.9: *Injured neurons show a decrease in Sholl crossings during their initial outgrowth.* Pcdh-γ KD contralateral neurons show greater arborization, but this effect is lost following injury. A: micrograph of Pcdh-γ Con neuron. B: analyzed tracing with Sholl shells placed every 10 µm. C: Sholl quantification ±SEM. 20 randomly selected cells were taken and averaged from each experiment, after a 24 h incubation. D: quantification of area under the curve measurements ±SEM. (t-test; Pcdh-γ KD Con vs Pcdh-γ KD Inj $p = 0.004$, Scr Con vs. Scr Inj $p = 0.046$). (Pcdh-γ Con: n = 4, Scr Con: n = 4, Pcdh-γ Inj: n = 5, Scr Inj: n = 5.) * = $p < 0.05$, ** = $p < 0.01$. Con, contralateral; Inj, injured; Scr, scrambled siRNA.

2.3.4. *Pcdh-γ KD prevents self-crossings following a peripheral nerve injury.*

We next investigated whether the phenomenon of self-avoidance was lost in the absence of Pcdh-γ in both injured and contralateral cultured adult sensory neurons, such as it is in Pcdh-γ mutant Purkinje and starburst amacrine cells (Lefebvre et al., 2012). Dissociated DRGs were plated and allowed to grow for 24 h in the presence of Pcdh-γ siRNA to knock down the mRNA (Pcdh-γ KD Inj/Con), or a scrambled siRNA (Scr Inj/Con). Neurons were fixed, processed for NF200, and imaged such that the majority of the neurite spread was contained within a single image (see Figure 2.10). Images were run through Neuromath to generate a standardized tracing of the neurites (Figure 2.10B). The first randomly selected 25 cells per condition per experiment was analyzed (Pcdh-γ KD Inj: n = 214, Pcdh-γ KD Con: n = 210, Scr Inj: n = 207, Scr Con: n = 206). Neurons were analyzed separately, not grouped across experiments justified by the measure being intrinsic to the cell, and likely independent of other surrounding cells, compared to neurite extension which can be influenced by plating density (Parnas and Linial, 1997; Radio et al., 2008). Intersections between sibling neurites were labeled manually and cross-referenced using the overlaid Neuromath generated image (Figure 2.10C). Any intersections of neurites not detected by Neuromath were excluded. If an image contained two cells that were sprouting and it was unclear which neurites belonged to which cell, that image was excluded.

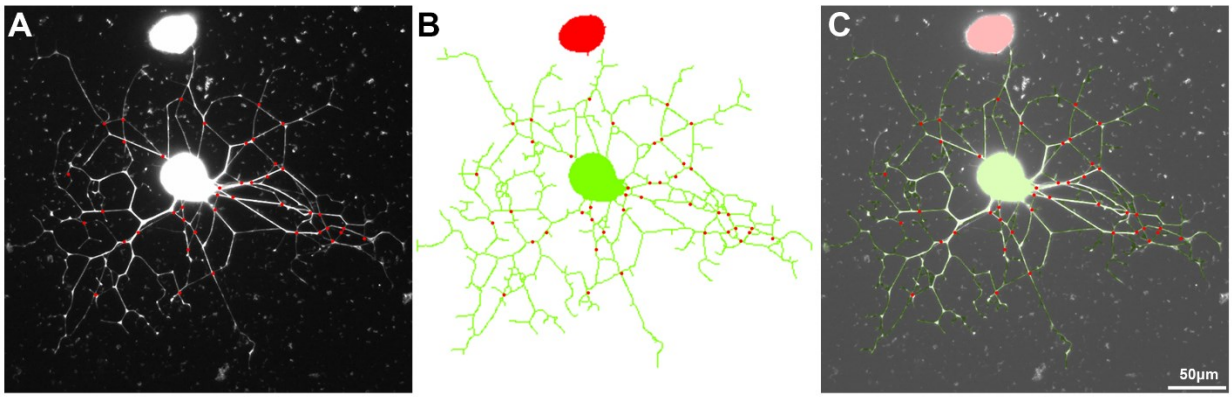

Figure 2.10: *Self-intersection analysis example.* Images were taken of neurons with the majority of the neurite spread contained in an image (A), and processed through Neuromath, which generates a tracing of the neurites (B). Intersections were labeled manually on the original image, and the tracing was overlaid (C) to help exclude intersections between neurites which were not picked up by the Neuromath software.

Contrary to much of the CNS Pcdh-γ literature showing increased self-crossings following Pcdh-γ removal, we found that the injured Pcdh-γ KD neurons showed significantly fewer intersections per cell compared to the rest of the groups (Mann Whitney; Pcdh-γ KD Inj = 15.1±1.4 intersections (mean±SEM), Pcdh-γ KD Con = 24.3±1.7, $p < 0.0001$, Figure 2.11A). Despite a trend in the same direction, we did not identify a significant difference between Pcdh-γ KD Inj and Scr Inj (Mann Whitney; $p = 0.10$). In Figure 2.11B, the quartiles in the violin plot (dashed lines), illustrates that 50% of injured neurons, regardless of siRNA treatment, contained less than 9 intersections/cell (median values; Pcdh-γ KD Inj: 8 intersections/cell, Scr Inj: 8.5 intersections/cell), compared to the contralateral neurons (median values, Pcdh-γ KD Con:19 intersections/cell, Scr Con: 16 intersections/cell). A two-way ANOVA was conducted and we found a main effect of injury, ($F(1,837) = 6.445$, $p = 0.01$), and a main effect of treatment ($F(1,837) = 4.609$, $p = 0.03$), but we also had a significant interaction between injury and treatment ($F(1,837) = 5.112$, $p = 0.02$). Figure 2.11C illustrates that the interaction was likely

driven by injury. This suggests that, specifically in neurons that lacked Pcdh-γ, the injury was the driving force to decrease intersections. Since the number of intersections is likely correlated to the amount of neurite outgrowth, we then assessed whether the lower number of intersections was due to the fact that the Pcdh-γ group showed the lowest amount of average neurite outgrowth in the neurons analyzed (Pcdh-γ KD Inj: 2477±120 a.u. (±SEM), Pcdh-γ KD Con: 2871±144, Scr Inj: 2920±153, Scr Con: 3085±154). We conducted a regression to visualize the relationship between intersections and confirmed neurite length (Figure 2.11E, Pcdh-γ KD Inj R^2 = 0.363; Pcdh-γ KD Con R^2 = 0.367; Scr Inj R^2 = 0.361; Scr Con R^2 = 0.367). The slopes suggest that the Scr Inj group (red line) has the greatest number of intersections/cell, and this increases most dramatically as the neurite extension increases. Slopes and 95% confidence intervals are graphed in Figure 2.11F, with the Scr Inj group showing no overlap with any other group (Pcdh-γ KD Inj slope = 6.8 intersections per 1000 confirmed length, [5.8, 7.8]; Pcdh-γ KD Con slope = 7.6, [6.7, 8.6]; Scr Inj slope = 10.8, [9.4, 12.2]; Scr Con slope = 8.2, [7.0, 9.3]). This is interesting, as the Scr Inj group also showed fewer intersections compared to the Scr Con group (Scr Inj = 23.5±2.5, Scr Con = 24.0±2.0, p = 0.04). This finding, alongside the ANOVA interaction in Figure 2.11C, highlights a unique role of Pcdh-γ. At a high level of neurite outgrowth, the dichotomy effect injury has on self-intersections becomes clear. It is theoretically dependent on the presence of Pcdh-γ, with an intact Pcdh-γ allowing the formation of more intersections, and the removal of Pcdh-γ preventing the formation of intersections.

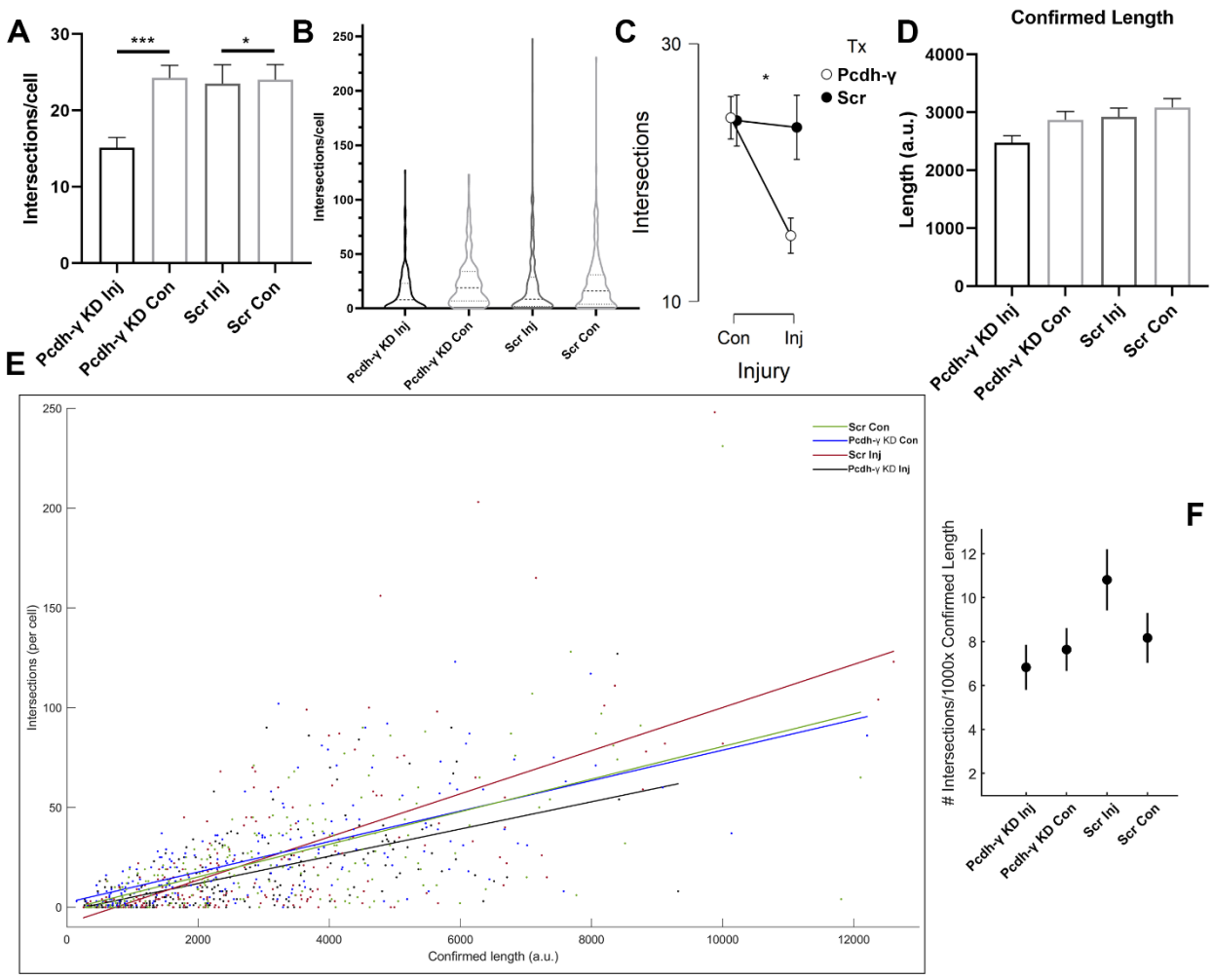

Figure 2.11: *Injury influences the number of self-intersections in cultured DRG neurons, and is tied to the presence of Pcdh-γ.* A: Bar graph showing number of intersections per cell in each group. Both injury groups showed less intersections per cell compared to their respective contralateral groups (±SEM, Mann Whitney; Pcdh-γ KD Inj vs. Pcdh-γ KD Con $p < 0.0001$, Pcdh-γ KD Inj vs. Scr Inj $p = 0.10$, Scr Inj vs. Scr Con $p = 0.04$). B: violin plot illustrating distribution and quartile ranges of intersections per cell for each group. (Median, thick dashed line). C: A significant interaction between treatment and injury is likely driven by injury in the Pcdh-γ KD group (±SEM, two-way ANOVA $p = 0.02$). D: Box plot of confirmed length per group. E: Regression of intersections and confirmed length of all groups (Pcdh-γ KD Inj $R^2 = 0.363$; Pcdh-γ KD Con $R^2 = 0.367$; Scr Inj $R^2 = 0.361$; Scr Con $R^2 = 0.367$). F: Slopes and 95% confidence intervals plotted for each group. * = $p<0.05$, *** = $p<0.001$. Pcdh-γ KD Inj: n = 215, Pcdh-γ KD Con: n = 211, Scr Inj: n = 208, Scr Con: n = 207. a.u., arbitrary units.

We also assessed neighbour crossings *in vitro*. We selected images that contained at least two neurons with neurites that were long enough to reach each other but did not necessarily cross. Since we could not be unequivocal of the origin of all neurites, we conducted an estimate of intersections of neurites we were confident belonged to separate cells. The difference between the contralateral Pcdh-γ KD and Scr groups was non-significant, however this is likely due to low statistical power, as a post hoc power analysis reveals a strong effect size of 0.9, and we can achieve significance with 33 replicates at a threshold of $\alpha = 0.05$. If by increasing our numbers we achieve significance, that would suggest these neurons are not participating in neighbour avoidance, or tiling (Mann-Whitney; n = 4, Pcdh-γ KD Con = 4.3±0.6 intersections; n = 3, Scr Con = 3.3±0.1 intersections; $p = 0.40$; Figure 2.12A). The Injured groups showed no significance (t-test; n = 4, Pcdh-γ KD Inj = 3.5±0.2 intersections; n = 4, Scr Inj = 3.8±0.5 intersections; $p = 0.34$). There were no significant differences comparing the effect of injury within treatment groups (t-test, Pcdh-γ KD Con vs Pcdh-γ KD Inj $p = 0.14$, Scr Con vs. Scr Inj $p = 0.19$). To get a more comprehensive view, we also conducted a binary analysis, assigning a value of 1 to neurons that intersect with their neighbours at any point, and a value of 0 to neurons that do not intersect. This allowed us to calculate a percentage of encounters that result in intersections with their neighbours. We saw a different result emerge: Injured Pcdh-γ KD neurons show increased instances of intersecting neighbouring neurites compared to Injured Scr neurons, with contralateral Pcdh-γ KD neurons exhibiting a higher but nonsignificant percentage of neurons intersecting compared to contralateral Scr neurons (t-test; Pcdh-γ KD Inj = 76±6%; n = 4, Scr Inj = 64±5%; $p = 0.03$; Pcdh-γ KD Con = 66±8%; n = 4, Scr Con = 47±15%; $p = 0.17$, Figure 2.12B). There were no significant differences comparing the effect of injury within treatment groups (t-test, Pcdh-γ KD Con vs Pcdh-γ KD Inj $p = 0.18$, Scr Con vs. Scr Inj $p = 0.19$).

Regardless of the measure or the injury condition, we found that the Pcdh-γ KD groups show more neighbour intersections than their Scr controls. It could be interpreted that while Pcdh-γ KD neurons typically engage in less self-intersections as seen in the above analyses, they appear to engage more in neighbouring intersections, which would support the idea that Pcdh-γ allows the neuron to recognize self from non-self, and facilitate tiling with other neurons of the same type. One limitation in this assay was the identification of neurons of the same DRG subtype. There are numerous subtypes of DRG neurons that terminate in different sensory endings (ie. nociceptors vs. light touch mechanoreceptors), which would theoretically need to organize within their own subtype, so each have equal coverage. To fully establish whether DRG neurons are tiling with other similar cell types, we would need to examine instances of two like-subtypes interacting, compared to two unlike-subtypes.

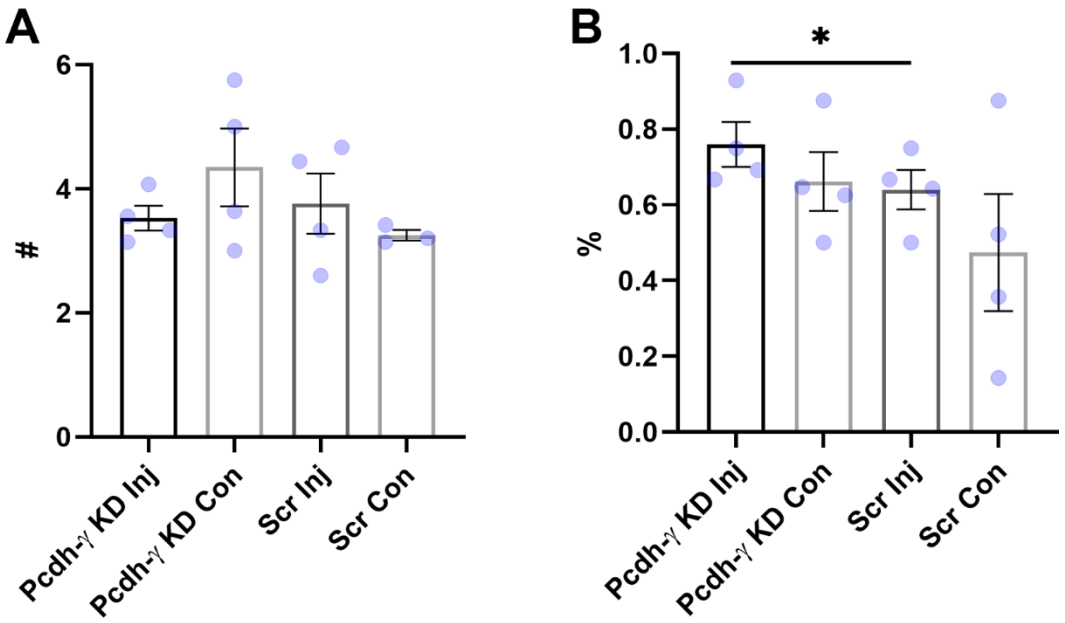

Figure 2.12: *Intersections between neighbouring cells.* Neurons treated with Pcdh-γ siRNA or Scr siRNA were either administered a sciatic nerve injury (Inj), or not (Con), and intersections were either quantified, counting only those that were confidently arising from separate neurons (A, Mann-Whitney; Pcdh-γ KD Con (n = 4) vs Scr Con (n = 3) $p = 0.40$), or neuron pairs were classified as "intersecting" or "not intersecting", and a percentage of encounters that were "intersecting" was calculated (n = 4, t-test; Pcdh-γ KD Inj vs Scr Inj $p = 0.03$)* = $p < 0.05$. Error bars indicate ±SEM.

2.3.5. *Effect of Pcdh-γ knockdown in vivo*

To confirm whether the increased neurite extension seen *in vitro* will be present *in vivo*, we aimed to knockdown Pcdh-γ *in vivo* and evaluate whether there would be increased innervation densities of sensory neurons in the footpad. We also carried out behavioural assays to analyze whether changes identified translated into a functional behavioural phenotype. Using previously described methods from our lab (Christie et al., 2014; Zubkow, 2018), we employed a non-viral strategy to knockdown Pcdh-γ using siRNA locally administered directly to the nerve and footpads following a sciatic nerve injury. Mice were administered either Pcdh-γ or Scr siRNA both locally to the nerve crush site, as well as injected directly into the footpad 3x/week. Behavioural and electrophysiological testing was conducted prior to the injury (Day 0), as well as on Days 14 and 28 prior to harvesting.

Following a 28-day recovery protocol, qRT-PCR analysis was conducted to measure the effect of Pcdh-γ gene knockdown at the level of the footpads as well as the DRG compared to mice administered scrambled negative control sequence siRNA (Scr). There was no significant knockdown of Pcdh-γ mRNA in the footpad following Pcdh-γ siRNA administration (Mann-Whitney; Pcdh-γ KD = 0.6±0.1 RFE; Scr siRNA = 1.0±0.1 RFE; p = 0.09, Figure 2.13), as well in the DRG, no such knockdown was observed (t-test; Pcdh-γ KD = 1.2±0.1 RFE; Scr siRNA = 1.0±0.2 RFE; p = 0.34). A power analysis showed a strong effect size for the footpads at 1.92, requiring 7 replicas to achieve significance. The DRGs had a medium effect size of 0.54, requiring 76 replicates for a significant difference to be achieved. Based on this, we cautiously interpret a successful knockdown in the footpads, but not for the DRGs.

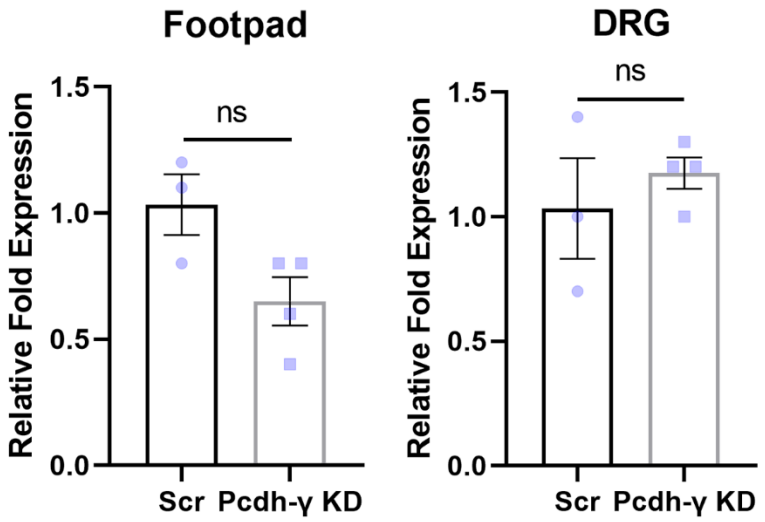

Figure 2.13: *qRT-PCR results from footpad and DRGs from mice treated with Pcdh-γ siRNA, or a scrambled control (Scr).* Scr: n = 3, Pcdh-γ KD: n = 4. Mann-Whitney; Footpad p = 0.09, DRG p = 0.34. Error bars indicate ±SEM. DRG, dorsal root ganglion; ns, non-significant

2.3.5.1. Mice treated with Pcdh-γ siRNA show no significant differences in nerve conduction analyses compared to controls

Nerve conduction analyses were also performed on the ipsilateral footpads (Pcdh-γ KD siRNA: n = 10, Scr siRNA: n = 5, Figure 2.14) at several timepoints following the sciatic nerve crush (0 days prior to injury, 14 days, 28 days) to measure compound motor action potentials (CMAPs, Figure 2.14A-C) and sensory nerve action potentials (SNAPs, Figure 2.14D-F). Recordings containing volume conduction or other interference were excluded by a blinded evaluator. At 14 days, average CMAP amplitudes in both groups were reduced compared to baseline, as expected following injury, and there were no significant differences between either group at 14 days (t-test; CMAP Baseline; n = 10, Pcdh-γ KD=10.5±0.9 mV; n = 5, Scr = 11.4±1.4 mV, p = 0.59; Figure 2.14A. 14 days; n = 9, Pcdh-γ KD= 0.8±0.3 mV; n = 4, Scr = 0.7±0.5 mV, p = 0.87; Figure 2.14E). Due to nonrecordable responses, we were not able to compute CMAP conduction velocities (CV) at 14 days. At 28 days, there was a slight

improvement, but not significantly different between the two groups (t-test; CMAP 28 days; n = 6, Pcdh-γ KD=1.8±0.5 mV; n = 4, Scr = 1.0±0.3 mV, $p = 0.26$; Figure 2.14H.) This improvement was not significant between 14 days and 28 days within groups (t-test; Pcdh-γ KD $p = 0.11$, Scr $p = 0.63$).

SNAP average amplitudes were also reduced at 14 days compared to baseline following injury, and were not significantly different between Pcdh-γ KD and Scr groups (t-test; SNAP Baseline; n = 9, Pcdh-γ KD= 17.1±2.6 μV; n = 5, Scr = 14.1±3.9 μV, $p = 0.51$; Figure 2.14C. 14 days; n = 10, Pcdh-γ KD= 0.2±0.1 μV; n = 4, Scr = 0.3±0.1 μV, $p = 0.94$; Figure 2.14F). SNAP CVs were also decreased at 14 days, and were similar between the two groups (t-test; SNAP CV Baseline; n = 9, Pcdh-γ KD= 37.6±3.0 m/s; n = 5, Scr = 41.2±4.1 m/s, $p = 0.48$; Figure 2.14D. 14 days; n = 10, Pcdh-γ KD= 5.2±3.8 m/s; n = 4, Scr = 6.3±3.8 m/s, $p = 0.87$; Figure 2.14G). Similar to the CMAPs, there was a slight improvement in both SNAP average amplitudes and average CVs at 28 days, but again these were not significantly different between Pcdh-γ KD and Scr groups (t-test; SNAP 28 days; n = 10, Pcdh-γ KD= 3.5±1.6 μV; n = 3, Scr = 5.6±2.8 μV, $p = 0.52$; Figure 2.14J. SNAP CV 28 days; n = 10, Pcdh-γ KD= 11.0±2.8 m/s; n = 3, Scr = 18.3±2.2 m/s, $p = 0.19$). There was a significant improvement of CV recordings in the Scr group between 14 and 28 days, ($p = 0.04$), as well as a trend, albeit not significant, towards improvement in SNAP average amplitude in the Pcdh-γ KD group ($p = 0.07$).

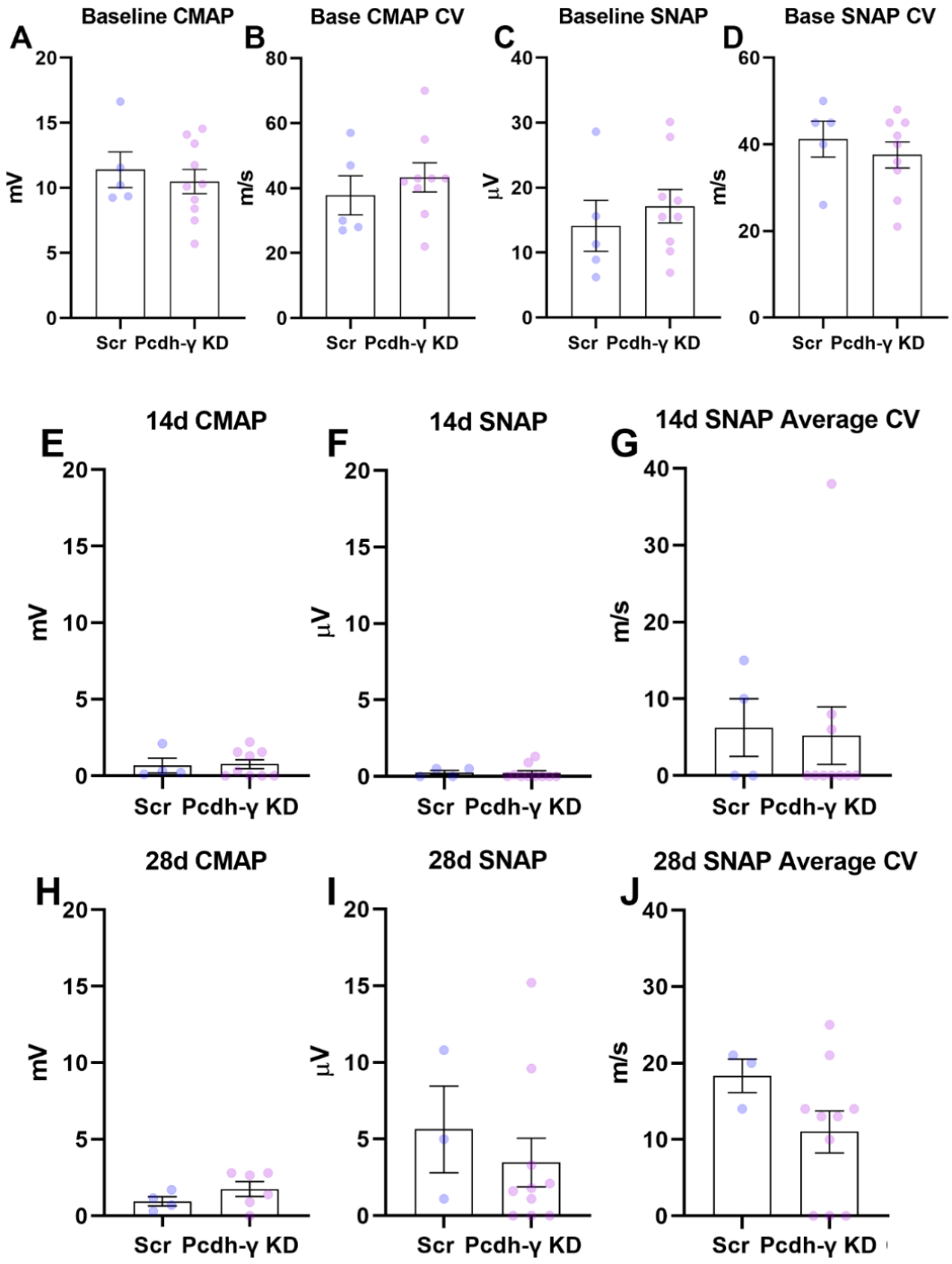

Figure 2.14: *Pcdh-γ KD animals show no significant differences in nerve conduction analyses at 0, 14, or 28 days.* Compound motor action potentials (CMAPs, A-C) and sensory nerve action potentials (SNAPs, D-F) were measured from animals 0 (A-D), 14 (E-G), and 28 days (H-J) after injury. Conduction velocities (CVs) are shown in B, D, G, J. t-tests were conducted for all comparisons. Both groups show no differences at 14 days, consistent with a successful nerve crush (CMAPs ($p = 0.87$), SNAPs, ($p = 0.94$), or in SNAP CVs ($p = 0.87$). However, there were also no significant differences in improvement between treatment groups at 28 days in either the CMAPs ($p = 0.26$), SNAPs, ($p = 0.52$), or in SNAP CVs ($p = 0.19$). Error bars indicate ±SEM.

2.3.5.2. Mice treated with Pcdh-γ siRNA did not show significant differences in behaviour assays

Thermal and mechanosensitivity tests were conducted at Day 0 prior to injury, Day 14, and Day 28 to track changes in sensitivity throughout the regeneration period, with the results plotted in Figure 2.15. Mechanosensitivity testing was done using Von Frey fibres on the ipsilateral (injured) foot, and the force to achieve consistent (75%) paw withdrawal was recorded. This test allows quantification of functioning nociceptors (Kruger, 2001 p.23; Bradman et al., 2015). While the responses are consistent between animals treated with Pcdh-γ siRNA (grey bars, n = 10) and the Scr siRNA (black bars, n = 5) at 14 days (t-test; Pcdh-γ KD = 0.70±0.10 g (mean±SEM); Scr = 0.76±0.19 g; $p = 0.77$), there was a nonsignificant trend towards the Pcdh-γ KD group exhibiting increased sensitivity by 28 days (t-test; Pcdh-γ KD = 0.60±0.07 g; Scr = 0.80±0.18 g; $p = 0.24$, Figure 2.15A). There was no difference at baseline (t-test, $p = 0.20$). Percent change was also calculated for each individual between timepoints, and there were no significant differences between groups (t-test; Baseline-14 day, Pcdh-γ KD = -25±12%, Scr = -45±7%, $p = 0.28$; 14 day-28 day, Pcdh-γ KD = -6±11%, Scr = -27±35%, $p = 0.30$; Baseline-28 day, Pcdh-γ KD = -31±13%, Scr = -24±27%, $p = 0.78$; Figure 2.15C).

Thermal sensitivity testing was also completed using the Hargreaves apparatus, and time measured for paw withdrawal was recorded for the ipsilateral foot (Figure 2.15B, D). There were no significant differences recorded between either group (Figure 2.15B, t-test; Baseline, Pcdh-γ KD = 8.9±0.8 s (mean±SEM), Scr = 9.4±1.1 s, $p = 0.74$; 14 days, Pcdh-γ KD = 7.3±0.5 s; Scr = 7.8±1.2 s; $p = 0.67$; 28 days, Pcdh-γ KD = 8.0±0.7 s; Scr = 7.3±1.4 s; $p = 0.64$; Figure 2.15D, t-test; Baseline-14 day, Pcdh-γ KD = -13±10%, Scr = -12±15%, $p = 0.97$; 14 day-28 day, Pcdh-γ

KD = -13±11%, Scr = -5±15%, $p = 0.36$; Baseline-28 day, Pcdh-γ KD = -9±7%, Scr = -11±27%. $p = 0.90$).

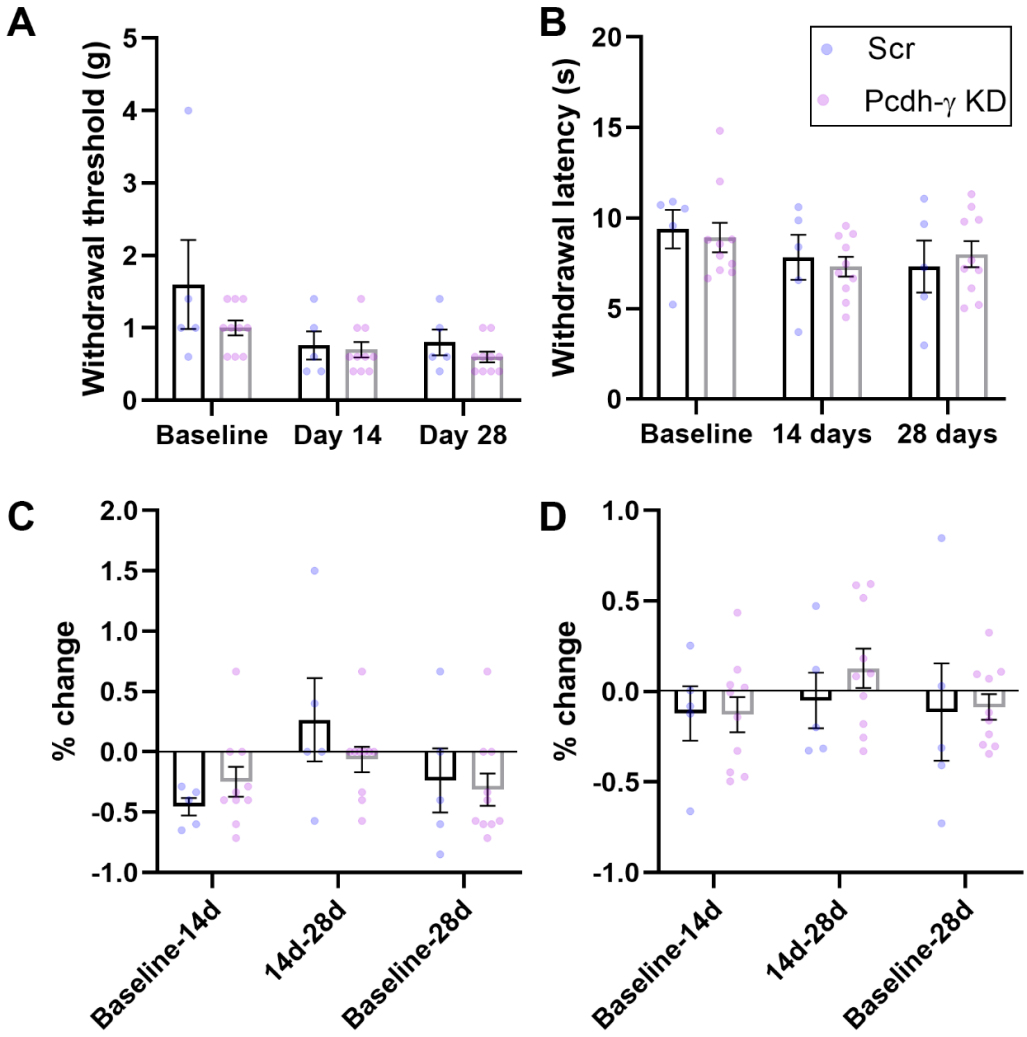

Figure 2.15: *Mice treated with Pcdh-γ siRNA did not show any significant differences in behaviour compared to animals treated with Scr siRNA*. Von Frey (A, C) and Hargreaves (B, D) analyses were conducted on animals treated with Pcdh-γ siRNA (grey bars) and a scrambled control (Scr, black bars). Weight to withdraw was recorded as a group average, (A, t-test; Baseline $p = 0.20$, Day 14 $p = 0.77$, Day 28 $p = 0.24$), or a % change across subjects (C, t-test; Baseline-14 d $p = 0.28$, 14 d-28 d $p = 0.30$, Baseline-28 d $p = 0.78$). Time to withdraw was recorded as a group average (B, t-test; Baseline $p = 0.74$, Day 14 $p = 0.67$, Day 28 $p = 0.64$), or a % change across subjects (D, t-test; Baseline-14 d $p = 0.97$, 14 d-28 d $p = 0.36$, Baseline-28 d $p = 0.90$). No significant differences were recorded. Pcdh-γ KD: n = 10, Scr n = 5. Error bars indicate ±SEM.

2.3.5.3. Mice treated with Pcdh-γ siRNA show preliminary evidence of an increase in epidermal reinnervation compared to contralateral controls

Anatomical observations of skin innervation were completed with the help of Mr. Honyi Ong for his undergraduate thesis work. Following the 28day recovery period, animals were sacrificed, and footpads harvested and processed for PGP9.5 expression. Fibres crossing the epidermal-dermal border were quantified per area and the results are presented in Figures 2.16 and 2.17. Representative confocal images are shown in Figure 2.16.

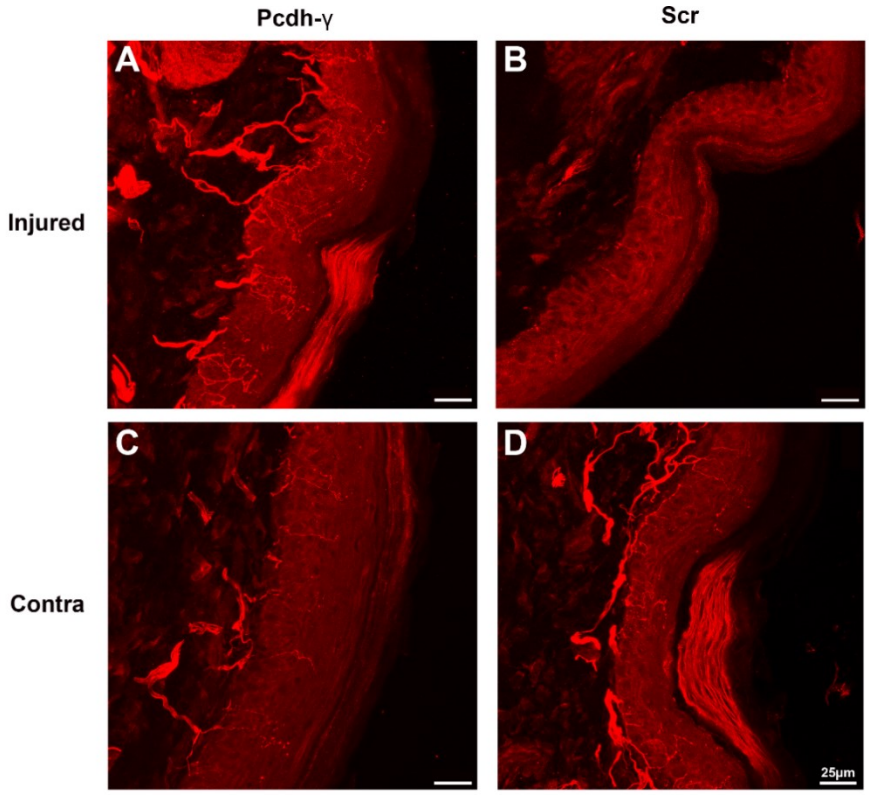

Figure 2.16: *Representative images of footpad innervation*. Animals were treated with Pcdh-γ siRNA (left column) or a scrambled control (Scr, right column), after being subjected to a sciatic nerve crush (injured, top row), or not (Contra, contralateral, bottom row). Sections were processed for PGP9.5 (red) to show sensory neurons penetrating the epidermis. Scale bar = 25 μm.

Fibres were quantified under four parameters: number of fibres per mm^2 (Figure 2.17A), number of fibres per mm of superficial length of epidermis (Figure 2.17B), number of horizontal fibres (as defined as those that show a 0° to 45° deviation from the surface of the skin) per mm^2 (Figure 2.17C), and number of vertical fibres (as defined as those that show a 45° to 90° deviation from the surface of the skin) per mm^2 (Figure 2.17D). Footpads treated with Pcdh-γ siRNA did not show any significant differences (Figure 2.17C), compared to contralateral control footpads. Interestingly however, the ipsilateral side had a higher density of fibres compared to the contralateral side, which has previously not been seen before in work using similar injury models, recovery times and mice. On average, there were 1218±343 fibres/mm^2 in the injured footpads (n = 3), and 659±135 fibres/mm^2 in the contralateral side (Mann-Whitney; p = 0.40). There were 189±52 fibres/mm in the Pcdh-γ KD group, and 135±13 fibres/mm in the contralateral footpad (Mann-Whitney; p = 0.70). There were 298±57 fibres/mm^2 growing in a horizontal trajectory in the injured footpads, and 125±3 fibres/mm^2 in the contralateral footpad (Mann-Whitney; p = 0.10). Finally, injured footpads in the Pcdh-γ KD group showed an average of 921±286 vertical fibres/mm^2 compared to the contralateral footpads, which only had 535±82 vertical fibres/mm^2 (Mann-Whitney; p = 0.70). The one animal in this experiment that was administered a scrambled siRNA (Scr) was included but due to insufficient sample numbers was not included in the analysis (Scr Inj fibre density = 558 fibres/mm^2, Scr Con = 1286 fibres/mm^2). Due to laboratory (pandemic) constraints, we were limited in the number of animals we could run. Based on the data collected from these three animals, we applied a power analysis between the density/mm^2 averages of the contralateral and ipsilateral Pcdh-γ KD siRNA groups to see how many animals that would need to be analyzed based on current trends observed. A moderate effect size of 0.77 was calculated, and given an alpha of 0.05, we estimated that we might require

24 animals to observe a significant difference between the two groups based on the data here. Similar power analyses for the other measurements were conducted and show similar results (fibres/mm; effect size = 0.48, n = 58. Horizontal fibres/mm^2; effect size: 1.74, n = 7, Vertical fibres/mm^2; effect size = 0.61, n = 37). Since all required n are in reasonable ranges, we cautiously conclude that, with larger sample sizes, we can achieve a statistically significant difference between groups.

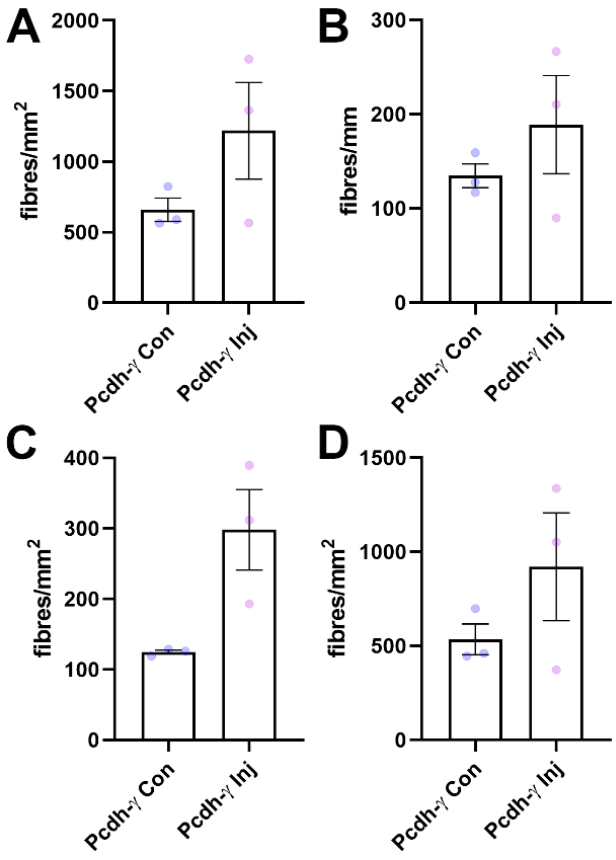

Figure 2.17: *Footpads treated with Pcdh-γ siRNA show no significant differences compared to their contralateral footpads.* Innervation densities were quantified per area (A, Mann-Whitney; $p = 0.40$), per length of epidermis (B, Mann-Whitney; $p = 0.70$), horizontal fibres per area (C, Mann-Whitney; $p = 0.10$) and vertical fibres per area (D, Mann-Whitney; $p = 0.70$). n = 3. Error bars indicate ±SEM. Con, contralateral; Inj, injured. Non-significant results are likely due to low power, see text for details.

These findings together with the electrophysiology and behavioural data in sections 2.3.5.1 and 2.3.5.2 suggest that, while we see heightened innervation following Pcdh-γ knockdown, this does not accompany measurable functional improvements following reinnervation.

2.4. Discussion

The present study was the first in-depth analysis of the expression and possible function of the gamma subcluster of the clustered protocadherin group (Pcdh-γ) in the mammalian peripheral nervous system. Using a systematic approach to characterize the expression of Pcdh-γ in the peripheral system, followed by a targeted Pcdh-γ knockdown through siRNA, we contribute some insights to the protocadherin literature and suggest its role within the context of peripheral nerve injury.

2.4.1. *Expression and response to injury*

Pcdh-γ is expressed throughout the peripheral nervous system, though most notably in the dorsal root ganglion (DRG) cell bodies, consistent with prior reports (Wang et al., 2002; Prasad et al., 2008). There is expression of Pcdh-γ protein in the sciatic nerve as well the terminal endings, however at such low levels they are challenging to detect through traditional immunohistochemical approaches. It is possible Pcdh-γ is present in Schwann cells, as there are reports of Pcdh-γ expression in other glial cells (Molumby et al., 2016), however we did not identify convincing labeling of them. One question that remains is its potential expression within the keratinocytes, as there is some evidence of Pcdh-γ expression in non-neuronal cells (Frank et al., 2005). Our immunoblots and immunohistochemistry supported this possibility. There is evidence that the level of Pcdh-γ expression is at its peak at the end of the second post-natal

week, with a slight decrease in RNA expression in adulthood (Frank et al., 2005), which supports the developmental roles Pcdh-γ likely fills in contrast to possible maintenance roles. As such, given that there are several molecules important in development that have a re-emergence following peripheral nerve injury (see Hilton and Bradke, 2017 for review), we were interested to evaluate whether Pcdh-γ also exhibits a similar temporal profile. We note a decrease of mRNA at 36 h post injury, which may represent the neurons prioritizing other proteins in its early injury response as the axon prepares for extension (Zochodne, 2008; Senger et al., 2018). We predict there is a corresponding change in protein expression levels, but at present we lack statistical support. Although some genes remain lower following injury, we saw a rise of Pcdh-γ mRNA to normal levels by 72 h post injury. While we did not investigate later time points, which may show an increase after 72 h, there must be a reason Pcdh-γ has active synthesis relatively soon following the injury. Indeed, knocking down Pcdh-γ after neurons have established their sensory arbour during development does not alter the phenotype (Garrett et al., 2012), which suggests they exert their effects during the growth phase. Therefore, in the context of regeneration following injury, we suggest that Pcdh-γ may assist in the axonal extension phase following injury of the peripheral neuron, but on a specific timetable.

Pcdh-γ was detected widely across DRG neurons (Figure 2.3A-F, 2.4A-F), suggesting a widespread role in peripheral sensory neurons. However, this does not accurately describe a possible pattern of a more segregated isoform expression. Certain isoforms are linked to specific functions, likely through specific internal signaling pathways mediated by unique juxtamembrane domains (Chen et al., 2017; Li et al., 2017; Garrett et al., 2019; Carriere et al., 2020), and some isoforms are preferentially expressed in certain CNS neuron populations such as Pcdh-α C2 in serotonergic neurons, and Pcdh-γ A12 in granule cells (Wang et al., 2002; Frank et

al., 2005; Chen et al., 2017). Ongoing collaboration efforts with the Lefebvre lab hope to address these issues within the PNS. Considering the role of the Pcdh-α C2 isoform in axon guidance of serotonergic neurons (Chen et al., 2017), as well as the role all Pcdhs play in facilitating proper olfactory glomeruli organization (Mountoufaris et al., 2017), it is possible DRG neurons destined to innervate the same region or dermatome may preferentially fasciculate together, guided by Pcdh isoform identity, to bring them to the same target destination. This would also explain the finding that DRG projections are topographically conserved at both the central (spinal cord) and peripheral (skin) terminal ends. As cells would express the same isoforms on both central and peripheral projections, this would allow similar relationships with other neurons at both ends, despite arising from spatially segregated DRGs (Esumi et al., 2005; Zylka et al., 2005; Kaneko et al., 2006; Kuehn et al., 2019).

2.4.2. *Effect of Pcdh-γ knockdown in vitro*

A common method for delineating the role of a protein is to determine how the cell functions in its absence. By designing a siRNA to the constant region of the Pcdh-γ gene, we were able to target most if not all Pcdh-γ proteins available for the cell to use. We unexpectedly found that the outgrowth of naïve, cultured DRG neurons following Pcdh-γ KD was significantly greater than those treated with a scrambled siRNA control. This was surprising, as much of the literature reports an associated decrease in dendritic growth and complexity (Garrett et al., 2012; Lefebvre et al., 2012; Suo et al., 2012).

However, a recent paper by Molumby and colleagues (Molumby et al., 2016) suggests that an incomplete decrease in Pcdh-γ isoform diversity paradoxically increases neuronal outgrowth, which is facilitated by increased instances of homophilic binding. In their study, they found that when pyramidal neurons expressing a single isoform grew in an environment where

the surrounding astrocytic population shared its Pcdh-γ isoform signature, there was enhanced growth compared to an environment with incongruent isoforms. With incomplete knockdown that follows the use of siRNA, it is possible that by decreasing the overall amount of Pcdh-γ, the remaining isoforms have an increased likelihood of matching, leading to increased homophilic binding, and to the observed increased neurite outgrowth.

However, this finding of increased growth following Pcdh-γ knockdown was lost following an injury. Injured neurons in both Pcdh-γ and Scr siRNA groups showed a similar decrease in Sholl crossings. Considering the drop in Pcdh-γ expression following injury as shown in section 2.3.2, the similar results we see between groups here may be because the Pcdh-γ levels in the Scr group are naturally lower, bringing it in line with the levels following Pcdh-γ siRNA KD. However, this does not explain why injured Pcdh-γ KD neurons show a dramatic decrease in self-intersections compared to Scr, when the level of outgrowth was controlled for. This is interesting in light of the current literature showing the role of Pcdh as an enabler of self/non-self avoidance through homophilic repulsion, and exhibit increased self-crossings following Pcdh-γ removal (Lefebvre et al., 2012; Kostadinov and Sanes, 2015; Molumby et al., 2016; Chen et al., 2017; Lefebvre, 2017). Further, much of the research done investigating self crossings have been done in cells that arborize in a single plane (ie. starburst amacrine cells, Purkinje cells, Lefebvre et al., 2012). While it is not known whether peripheral sensory neurons arborize in a planar orientation, this may also explain why we see contrasting results. Indeed, there are instances in non-planar neurons such as hippocampal pyramidal cells where self-avoidance is not clearly demonstrated (Garrett et al., 2012; Suo et al., 2012).

While we did not observe the same self-avoidance following injury, the story is different in neighbouring cell intersections. We noted that neurons with Pcdh-γ KD showed increased

encounters resulting in neighbour intersections. Overall, perhaps peripheral sensory neurons engage in tiling, where neurons avoid others of the same subtype (Grueber and Sagasti, 2010; Jan and Jan, 2010), more so than self-avoidance, which are better exemplified in complex, planar neurons such as starburst amacrine or Purkinje cells (Lefebvre et al., 2012). Indeed, recent evidence suggests PNS sensory neurons do engage in tiling with other neurons of the same subtype (Kuehn et al., 2019).

In addition, much of the literature on Pcdh has been focused on the dendritic arbours, while our data focuses on axons of peripheral sensory cells. There are many differences between the two terminal ends. In addition to the morphology of the endings themselves, dendrites typically have increased protein production due to the presence of a more robust rough endoplasmic reticulum (reviewed by Ramírez and Couve, 2011). Axons have lower protein production, as well they can express different proteins than dendrites, such as GFAP and PI3K during growth periods, leading to the possibility that they are guided differently (Sargent, 1989; Banker, 2003; Shi et al., 2003). However, the few reports on Pcdh in axons provide promising results that Pcdh plays similar roles in both axons and dendrites (Chen et al., 2017; Mountoufaris et al., 2017).

2.4.3. *Pcdh-γ knockdown in vivo*

While we did not get a significant knockdown of the footpad mRNA using Pcdh-γ siRNA, our power analysis suggests more this is due to lack of statistical power. However, mRNA levels in the DRG were decidedly less influenced, and were not impacted by the siRNA at the time point studied. This is possibly due to a compensatory mechanism by the neuron, with the DRG producing more protein to the Pcdh-γ deficient terminal endings. Alternatively, this could also be due to the mechanism in which we delivered siRNA. We delivered siRNA directly

to the footpad, but not to the DRG, which relied on retrograde transport of the siRNA. As well, levels of knockdown vary over such a long timeframe.

We saw no statistically different electrophysiological or behavioural results between groups of animals treated with Pcdh-γ or Scr siRNA at 28 days, however it is possible a longer time frame is needed to see functional differences. Despite these physiologic results, we did see an increase in epidermal innervation in the injured footpad compared to a contralateral control, following Pcdh-γ treatment. This is novel, as we have not encountered instances where the injured footpad at 28 days shows higher axon innervation levels compared to pre-injury levels, regardless of treatment. Historically, in experiments with similar mice, interventions and timepoints, uninjured (contralateral) footpads typically exhibit an innervation density of approximately 800 fibres/mm^2 (Toth et al., 2006; Zubkow, 2018; Poitras et al., 2019), with injured footpads measured at 28 d following a complete crush never exceeding 600 fibres/mm^2. However, despite comparable contralateral measures of footpad innervation, in two out of three of our injured Pcdh-γ samples, we measured over 1300 fibres/mm^2 (see Figure 2.18). The limitation of this finding is that further sample numbers are required to verify this result.

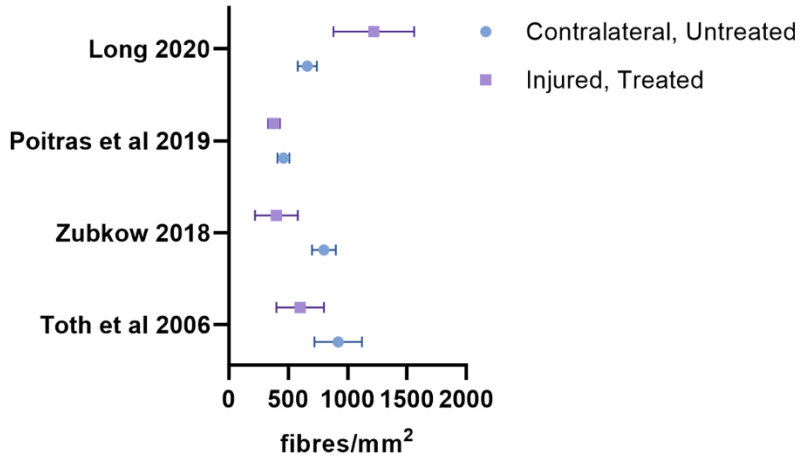

Figure 2.18: *Comparison of historical footpad innervation data from our lab.* Contralateral, control values were taken and compared to the injured, treated condition that showed the greatest fibre density per article. Plotted ±SEM. (Data taken from Toth et al., 2006; Zubkow, 2018; Poitras et al., 2019).

Pairing the histological findings with our *in vitro* outgrowth data suggests a very interesting role of Pcdh-γ during regeneration. With the Pcdh-γ mRNA levels intact, we see stable outgrowth, sensitivity, and innervation. This might be due to the increased diversity of Pcdh-γ subtypes available, imposing growth limitations on neurons. This follows the current theory that Pcdhs possess tumour suppressing abilities (Novak et al., 2008; Banelli et al., 2012; Dallosso et al., 2012; Severson et al., 2012). By adding an incomplete knockdown of the mRNA, we are effectively decreasing the diversity, facilitating homophilic binding, and increasing neurite extension and outgrowth, as demonstrated by Molumby et al. (2016).

However, it is worth highlighting the apparent contradiction between our injured *in vivo* data with our injured *in vitro* data. While we see decreased outgrowth and decreased intersections in injured animals *in vitro*, we see apparent increased epidermal innervation *in vivo*. The likely explanation is the timescale; our *in vivo* experiment examined innervation at 28 days post injury, while our *in vitro* studies are conducted at 72 h post injury, when neurons are

mounting their cell response (Zochodne, 2008). Knowing that manipulation of certain molecules is particularly effective at distinct time frames following injury, (Christie et al., 2014; Zubkow, 2018), there appears to be an appropriate time in which Pcdh-γ should be silenced to enhance neurite regeneration. Another possible explanation is through the potential expression of Pcdh-γ in keratinocytes. If there is Pcdh-γ present in keratinocytes, the incomplete knockdown and therefore decreased diversity of Pcdh-γ isoforms in keratinocytes may provide a proliferative environment for invading axons into the epidermis, which would explain why we see increased growth following Pcdh-γ knockdown *in vivo*, and also why we do not see the enhanced growth *in vitro* as keratinocytes are absent. However, this does not provide an answer to why we see increased outgrowth in naive cultures treated with Pcdh-γ siRNA.

Finally, the incongruency between the physiological and histological measures should also be addressed. The lack of statistical differences between the SNAP amplitudes at 28 days likely exists because SNAP recordings tend to reflect the larger diameter axons, which typically do not penetrate the epidermis (Krarup, 2004; Zochodne, 2008; Themistocleous et al., 2014), which would explain why we see a higher density of them in our histology, but no difference electrophysiologically. Similarly, SNAPs are recorded more proximal than the skin innervation examined in our histology. It is possible that the smaller fibres show selective increased regeneration, while the larger diameter axons have yet to regenerate to the same degree. This may be explained by isoform specificity, especially if certain sensory neuron types have certain Pcdh-γ sensitivities. However, we would expect some reflection of a higher density of smaller diameter, temperature sensitive, axons in the Hargreaves test which we did not see. Checking for coldness sensitivity may also be a valuable assay to isolate the smaller Aδ fibres without stimulating the larger-caliber axons (Hovaguimian and Gibbons, 2011), or assessing autonomic

function. However, qualitative responses are difficult to measure in animals (Misra et al., 2008). Overall, it should be noted that the lack of physiological differences between groups may reflect that the regenerated axons are not fully mature enough to carry out their designated function at the time point measured.

2.5. Limitations

Due to time constraints warranted by the recent pandemic, sample sizes are a significant limitation in this project, with several experiments limited to an n = 3. With more samples, it is possible we could strengthen many of the effects we see based on our current means and standard deviations. Another limitation of this study is the possible expression of Pcdh-γ in non-neuronal cells, such as satellite cells, Schwann cells, and keratinocytes, which may be driving some of the results we see instead of it being intrinsic to the neurons. However, these were not observed in careful DRG and sciatic nerve stains indicating that any expression would be low level and potentially of limited importance. Pcdh-γ is known to be expressed in astrocytes (Wang et al., 2002; Molumby et al., 2016), but at the time of writing, there are no reports of expression in other glial cells (Hirayama et al., 2012).

While there has been no evidence that sex is linked to differential Pcdh-γ expression and therefore function, likely due to the genes localization to an autosome, it is possible there are epigenetic factors present in either sex that may influence the transcription rate of particular isoforms.

Another important consideration when using siRNAs is the chance of off target effects, however a prior study using siRNA to two separate targets of the constant region of Pcdh-γ saw very similar results, suggesting there are little to no off-target effects (Dallosso et al., 2009). We routinely compare experiments to scrambled sequence siRNA controls.

2.6. Future Directions

As with all science, more questions have arisen from this project than have been answered. First, it would be prudent to conduct a larger temporal profile analysis of expression levels of Pcdh-γ following injury, to investigate if maybe there is a larger response, we are missing in our limited sampling times. As well, we are curious to see if we would identify comparable impacts in transgenic animals. Since global Pcdh-γ knockouts are perinatally lethal, we are currently in the process of breeding conditional Pcdh-γ knockout mice (Pcdh-γ^{fcon3}, Lefebvre et al., 2008) with an Advillin-Cre line (Zurborg et al., 2011) to limit the knockdown of Pcdh-γ to the peripheral sensory neurons. Since this would ensure a full genetic knockout, we would be able to see if epidermal hyperinnervation following injury persists in the total absence of neuronal Pcdh-γ. However, if Pcdh-γ is expressed in keratinocytes, we should see no difference to wild type controls, as that expression will not be altered in the transgenics. Further, using the transgenic animals would allow us to see what would happen to the organization and innervation density of peripheral sensory neurons during development into intact adults, in contrast to regeneration.

We are currently collaborating with the Lefebvre lab to conduct some Pcdh-γ individual isoform mapping through fluorescent *in situ* hybridization (FISH). Not only would this help us detect Pcdh-γ expression in the keratinocytes, it will also help us visualize the isoform diversity both before and after siRNA application.

As well, it would also be interesting to visualize the patterns of sensory innervation in the skin with single cell resolution. We are also currently in the process of breeding Brainbow animals (Cai et al., 2013) with our Advillin-Cre line, to elucidate the extent of innervation a

single neuron is responsible for, and if these neurons are segregated in space, or if they are intertwined. Recent developments suggest the former (Kuehn et al., 2019).

As mentioned above, there is evidence for preferential isoform expression in certain cell populations, we want to investigate whether there is a preferential expression of specific isoforms across all peripheral sensory neurons, or if there is a preferential distribution between different neuronal subtypes. As there are different types of peripheral sensory neuron, we would like to see if different subtypes express similar isoforms. It is understood that each isoform likely has a different intrinsic signalling pathway due to their unique juxtamembrane domain (Dallosso et al., 2012; Mah et al., 2016; Carriere et al., 2020), which leads to even more questions that may have implications for targeting regeneration in peripheral nerves. Particularly, if expression of a specific isoform is shown to have higher regenerative outcomes, over-expression of such isoform could be looked at as a therapeutic strategy.

2.7. Conclusion

Peripheral nerve regeneration has provided us with a unique approach to studying how the nervous system re-patterns itself following a disruption in function, and how this mechanism is likely not random. Peripheral nerve regeneration is challenged by roadblocks, both physical and chemical. While indeed there is the capacity for more spontaneous regeneration than seen in the CNS, this regeneration is often incomplete, and poorly understood (Zochodne, 2012). Clustered protocadherins appear to play a significant role in regeneraion, and this project has only uncovered our gap in knowledge in how it works to pattern the distribution of sensory axons. This study provides evidence that Pcdh-γ acts as a restrictor of neurite extension, as well as influences tiling for proper, functional innervation. Recently, there is evidence that Pcdh acts as a tumour suppressor, a familiar molecule to the regenerative community (Dallosso et al.,

2009; Mah et al., 2016; Duraikannu et al., 2019), which corresponds to the data we find. When Pcdhs are silenced, or methylated, as in several cancers (Waha et al., 2005; Novak et al., 2008; Dallosso et al., 2009; Banelli et al., 2012; Severson et al., 2012), there is unhindered growth. Clearly, further understanding is critically needed, as any molecule that enhances regeneration could potentially be manipulated to become a therapeutic treatment. As well, the results we see could also help our understanding of Pcdhs role in numerous diseases and sensory disorders in humans, as the protein sequence is highly conserved between mouse and human (Wu, 2001). The next chapter will examine how sensory systems maintain their exceptionally specific patterning beyond the terminal endings through their primary projections, and how these patterns are also conserved across species.

Chapter 3: Primary projections of the VIIIth nerve in two species of snakes: the western diamondback rattlesnake (*Crotalus atrox*) and the amazon tree boa (*Corallus hortulanus*).

This work was completed under the supervision of Dr. Douglas Wylie, from September 2015 - April 2018.

Abstract

Rotational movement detection occurs within the anterior, horizontal, and posterior semicircular canals within the vestibular labyrinth, and the structure has remained the same across many organisms. The signals generated within the vestibular labyrinth in response to rotational movement are then carried into the brainstem via the VIIth nerve (vestibulocochlear) and terminates on the vestibular complex.

The termination pattern of each semicircular canal has been described in many vertebrates; however technological constraints limited them to only tracing a single canal in a single animal. Using a novel *ex vivo* preparation for two previously undescribed vertebrates, juvenile brains from Western Diamondback Rattlesnakes (*C. atrox*) and Amazon Tree Boas (*C. hortunalus*) were isolated and placed in cold, oxygenated Ringer's solution. This allowed us to isolate each semicircular canal branch and apply individual tracers to allow us to visualize the termination pattern of all three canals within a single animal. We hypothesize the *ex vivo preparation* will allow us to confirm that the primary afferent termination of the semicircular canals of both snakes will be similar to that previously described in other vertebrates.

Consistent with previous descriptions of primary afferent terminations of the VIIIth nerve, we found that the termination pattern of the three semicircular canals was similar in both species of snake, with the anterior, horizontal, and posterior canals all terminating in spatially separate regions in the vestibular complex. In addition, we observed primary afferents from both the anterior and posterior canals terminating in the lateral anterior cerebellum, suggesting the snake vestibulocerebellum is localized to this region.

The vestibular cerebellum is an ancient sensory system that shows remarkable conservation in its primary afferent terminations in the vestibular complex within the brainstem. By tracing afferents from each semicircular canal within a single animal, we were able to confirm the overall projection patterns are similar across vertebrates, suggesting the separation of semicircular canal afferents are maintained for higher up processing.

Abbreviations:

VDesc	descending vestibular nucleus
VDL	dorsolateral vestibular nucleus
VM	medial vestibular nucleus
VVL	ventrolateral vestibular nucleus

3. *Introduction*

Comparative neurobiology provides a powerful strategy to bring unique context while studying the nervous system. Through observing the similar mechanisms and organization that arose either through conservation mechanisms or independent evolution, we can make educated assumptions as to how a certain system works. Some of the most conserved systems in the brain are the sensory systems (Hodos and Butler, 1997), as they evolved to allow organisms to safely interact with the environment, improving food identification, scavenging abilities, and predator avoidance. While some sensory systems show modifications, which are likely driven by the unique requirements of the ecological niche the organism fills (Hodos and Butler, 1997; Osorio and Vorobyev, 2008), some are intricately conserved. While the outside environment may vary, the internal environment of the body is more constant, but no less important for survival. This project will examine the vestibular system in a snake, an animal that significantly differs from other limbed vertebrates, such as a pigeon or monkey, but still demonstrates similar organization at the first level of sensory processing.

3.1.1. *Ophidian cerebellum*

In contrast to mammalian and avian cerebellums, the ophidian cerebellum, or the cerebella of snakes, is much simpler in structure. Consisting of a single dome of cells, the snake cerebellum lacks folia and instead appears to be a small flap that tilts caudally, partially covering the fourth ventricle (Larsell, 1926; Larsell and Jansen, 1967; Bangma, 1983; Voogd and Glickstein, 1998; Aspden et al., 2015). The presence of the three cellular layers of the cerebellum is maintained, but the postulated gross classification of the cerebellum has been contested (Larsell and Jansen, 1967). Due to the simplicity of the snake cerebellum structure, and the limblessness of the species, some have questioned the origin and diversity of afferent

connections (Larsell, 1926; Larsell and Jansen, 1967; Nieuwenhuys, 1967; Bangma, 1983). They postulate that the entire cerebellum subsists of only a vestibulocerebellum, a small part of the mammalian cerebellum, such that "in 'lower' vertebrates as reptiles, the cerebellum is dominated by vestibular afferents and connections from the nucleus of the basal optic root,…all related to the control of eye, head, and neck movements." (Bangma, 1983). Few studies have investigated the cerebellar afferent inputs in reptiles, and even less in the past 30 years. Bangma (Bangma and Donkelaar, 1982; Bangma, 1983) conducted HRP retrograde tracer studies on *Python regius,* however the technique did not provide the level of resolution achievable today. Currently, we have much finer neural tracing tools available to us (see Newlands and Perachio, (2003) for a review in mammals), and these would allow us to make more accurate observations of the conservations and variances seen across the reptilian class.

3.1.2. *Vestibular labyrinth and the VIIIth nerve*

Compared to the cochlea, the vestibular system as a sense had not been studied until the 19th century when Pierre Marie Flourens linked the semicircular canals to balance and coordination of the head and eyes in pigeons (Wiest, 2015). The vestibular labyrinth is a continuous structure filled with a potassium-rich endolymph fluid, which the movement and inertia of transfers kinetic energy to the hair cells, which confer acceleration information of translational and rotational movement of the organism. Divided into two organ systems, the otoliths (utricle and saccule) transduce translational movement, while the semicircular canals transduce rotational movement about several axes (Kandel et al., 2000 p.918). The individual neurons arising from the hair cells within the vestibular labyrinth coalesce and travel into the brainstem via the VIIIth cranial nerve, the vestibulocochlear nerve. In reptilians, this nerve feeds the papilla basilaris, a mammalian homologue to the organ of Corti (Larsell and Jansen, 1967),

the lagena (Harada et al., 2001), and semicircular canals. The semicircular canals have three branches: a horizontal branch, which lies in the horizontal plane, and an anterior and posterior branch, which are oriented 90^{o} from each other with the anterior canal existing in the vertical axis oriented 45^{o} from the midline, and the posterior canal existing in the vertical axis oriented 135^{o} from the midline. These canals contain the hair cells that transduce movement of the endolymph from within the canals, which is maximized by rotation about the axis of the canal. Hair cells then project fibres to the vestibular ganglion, or Scarpa's ganglion, and from there send axons to the brainstem and the cerebellum (Kandel et al., 2000).

3.1.3. *Primary vestibular afferents*

While many experiments have investigated the primary terminations of the VIIIth nerve in vertebrates, the methods used were limited. Degeneration experiments were favoured in early studies of vestibular projections, but it was soon discovered that the degeneration often stopped at the level of the ganglion, so attempts to isolate a single end organ were futile (Carpenter et al., 1972; Foster and Hall, 1978). Retrograde and anterograde tracers were then used, however only a single canal was stained due to the monochromatic nature of the dyes available at the time (HRP, WGA-HRP, cobalt staining, etc. Matesz, 1979; Barbas-Henry and Lohman, 1988; Burian and Gstoettner, 1988; Dickman and Fang, 1996). To our knowledge, there has been no report of heterochromatic tracings of primary vestibular afferents from all three semicircular canal branches within a single animal.

Despite tracing primary afferents in multiple animals, primary vestibular afferents have been described projecting to various complexes in addition to the vestibular complex and cerebellum. The accessory vestibular nuclei, cerebellar nuclei, and various extra-vestibular

regions such as the abducens nuclei, the cochlear nuclei, and the reticular formation all receive primary projections as well. (see Newlands and Perachio, 2003 for review).

This project aims to answer two problems; can we individually trace all semicircular canals simultaneously in a single animal, and can we confirm the projection patterns of primary vestibular afferents in the snake to compare them to other animals that have been previously investigated? To tackle this, we used an *ex vivo* whole mount preparation of two species of juvenile snake, the Western Diamondback Rattlesnake, *Crotalus atrox* and the Amazon Tree Boa, *Corallus hortulanus.* These two species were chosen since their natural occupancy covers terrestrial and aerial habitats respectively, as different niches may require differing vestibular demands.

3.2. Methods

3.2.1. *Animal Care*

In vitro experiments were performed on isolated brains of two juvenile Western Diamondback rattlesnakes (*Crotalus atrox)*, and three juvenile Amazon Tree Boas (*Corallus hortulanus)* with the help of Drs. Maximilian Bothe, Tobias Kohl and Harald Luksch. The snakes were bred in captivity in the Department of Zoology at the Technical University of Munich. Snakes were kept on a 12:12 h light:dark cycle in a 22-30°C temperature range, with a diet of pre-killed mice and water ad libitum. Care and maintenance of these animals followed the established guidelines for venomous snakes and their use in these experiments was approved by the Government of Upper Bavaria, (Regierung von Oberbayern, 55.2-1-54-2532.6-9-12), the corresponding overseeing body responsible for animal care.

3.2.2. *Ex vivo whole mount preparation*

The snakes were anaesthetized using inhaled isofluorane via an induction chamber until the tail pinch reflex ceased. Snakes were then administered a cocktail of ketamine (40 mg/kg) and xylazine (20 mg/kg) intramuscularly. The snakes were placed supine, and the thoracic cavity was opened to perfuse transcardially with ice cold oxygenated Ringer's solution (in mM: 96.5 NaCl, 31.5 $NaHCO_3$, 4 $CaCl_2$, 2.6 KCl, 2 $MgCl_2$, and 20 D-glucose, pH 7.4). Following decapitation and removal of the lower jaw, the remaining dorsal part of the skull was transferred and fixed with needles ventral side up in a Sylgard-lined petri dish (Dow Corning, Wiesbaden, Germany), filled with ice cold Ringer's solution that was maintained at 4-8°C.

To access the VIIIth nerve, the brains were isolated from the surrounding tissue and bone while submerged in Ringer's solution. The nerve is encapsulated in a bony sheath, which was carefully opened to reveal the three branches of the VIIIth nerve (See Figure 3.1).

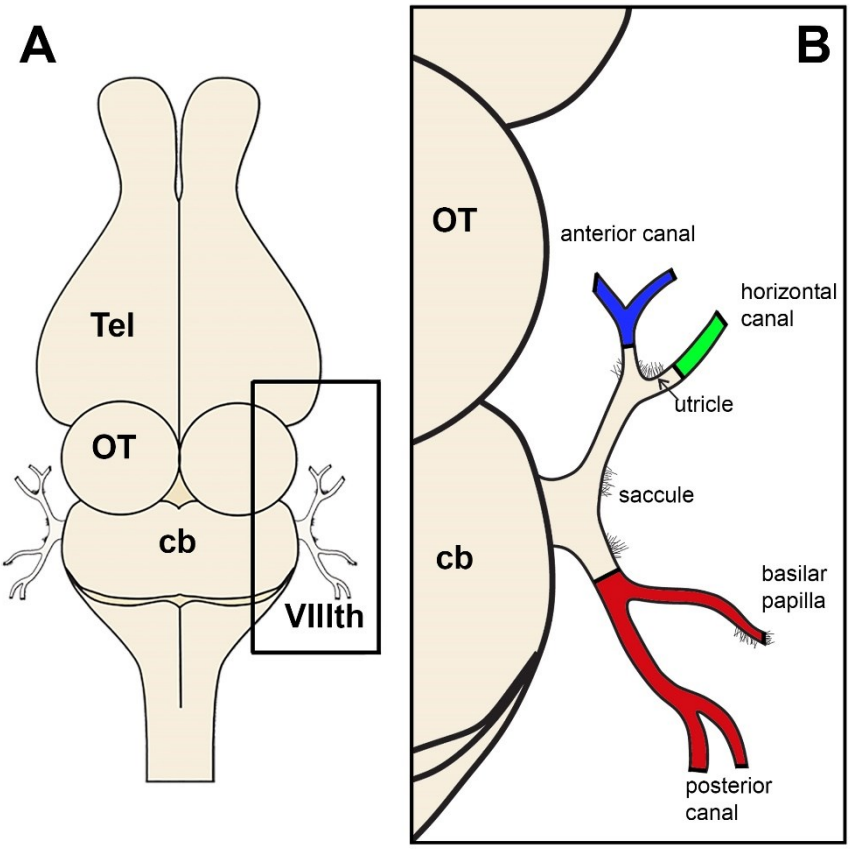

Figure 3.1: *Schematic of C. atrox brain with VIIIth nerve exposed.* A, whole brain schematic. Right, area within box enlarged to illustrate the anterior branch, containing afferents from the anterior canal, horizontal canal, utricle and saccule, and the posterior branch, containing afferents from the posterior canal and the basilar papilla. Colours represent scheme used throughout paper. Tel, telencephalon; OT, optic tectum; cb, cerebellum; VIIIth, vestibulocochlear nerve.

3.2.3. *Nerve tracer application*

Only one side was stained per procedure. The anterior, horizontal, and posterior branches were identified and isolated for the application of fluorescent tracers. Application of the fluorescent tracers was performed immediately after extraction. Using a syringe filled with petroleum jelly, a waterproof bowl was created around the isolated nerve branch and sealed to prevent spread of tracer to neighbouring tissue. The bowl was then cleared of Ringer's solution and filled with distilled water. The nerve was then cut and allowed to rest for 30 seconds to

prevent the resealing of the cut nerve ends. The distilled water was then replaced with either Dextran Texas Red (Dextran, Texas Red®, 3000 MW, Lysine fixable, Invitrogen, Carlsbad, CA), Dextran Fluorescein (Dextran, Fluorescein and biotin, 3000 MW, anionic, Lysine fixable (Micro-Emerald), Invitrogen), or Neurobiotin 350 (NeurobiotinTM 350, 573 MW, Vector Laboratories Inc., Burlingame, CA), at 5% in 0.1 M phosphate buffer. Each colour was used once per brain to identify individual projections from each branch. The scheme was kept consistent except for one snake, where the red and blue colours are flipped (seen in Figure 3.4). The basilar papilla branch was stained the same colour alongside the posterior branch as sufficient isolation between the two branches was not possible. The tracer was left for 15 min to allow uptake by the cut nerve endings. Remaining tracer was removed, and the preparations were washed with cold Ringer's solution, and maintained in 8°C Ringer's for 24-48 h to allow transfer.

3.2.4. *Tissue processing*

After incubation, the brains were fixed in 4% paraformaldehyde in 0.1 M PBS, pH 7.4, for a minimum of 24 h. Brains were then cryoprotected in a 30% sucrose/0.1 M PBS until they sank and were then embedded in 10% gelatin and cryoprotected once more. Frozen serial sections were cut through the cerebellum using a sliding microtome at 50 μm thickness in the coronal plane. The tissue was then mounted directly onto gelatinized slides for imaging (Leica DMRE), equipped with appropriate fluorescence filters (rhodamine, FITC, and DAPI). Images were acquired with a Retiga Exi FAST Cooled Mono 12-bit camera (Qimaging) and Openlab imaging software (Improvision). Adobe Photoshop was used to manipulate brightness and contrast.

3.2.5. *Microscopy*

Fluorescent images were acquired in three channels at 10X (rhodamine, Dextran Texas Red; FITC, Dextran Fluorescein; and DAPI, Neurobiotin) and overlaid for concurrent visualization. Images were stitched together in Photoshop. Following image capture, slides were subsequently Nissl stained with thionine and imaged once more to localize the terminals within the boundaries of the vestibular nuclei. Images were overlaid in Photoshop. Due to some tissue shrinkage following the Nissl protocol, images were mildly transformed so the gross landmarks of the section were consistent with the original fluorescent image.

3.2.6. *Reconstruction*

The VIIIth ganglion was reconstructed as a lateral projection by measuring the spread of the fluorescent cell labeling dorsoventrally for each section through the nerve. Based on the rostro-caudal distance between sections and the dorsoventral length of cell body distribution, we could approximate the shape and distribution of the cell bodies within the ganglion.

The brainstem and cerebellum sections were imported into Photoshop and overlaid. Sections from each snake were mapped out using notable landmarks including the nucleus motorius ventralis n. trigemini (trigeminal motor nucleus), the nucleus olivarius superior (superior olive), the nucleus parvocellularis medialis, and the nucleus motorius nervi facialis (facial motor nucleus), as described by Warner, (1935) and Bangma, (1983). Sections were aligned with other series from different samples of the same species based on landmarks. Sections were then traced for vestibular nuclei and overlaid to ensure congruency between biological replicates. An average outline of the brainstem, cerebellum, and vestibular nuclei were then drawn. From here, fluorescent images were overlaid, and terminal endings were mapped out

across the nuclei and reported as below. The terminal areas from all replicates were then overlaid on the average section and marked. Species were analyzed separately.

3.3. Results

3.3.1. *Nomenclature*

Based on the cytoarchitecture and location of the cell bodies from the thionine stained images (Warner, 1935, 1945; Matesz, 1979; Bangma, 1983; Ten Donkelaar et al., 1983), four vestibular nuclei and a cochlear nucleus were identified. While we expected to find two distinct cochlear nuclei, nucleus angularis and nucleus magnocellularis as per Warner, (1935), we failed to see any consistent distinct boundaries in our preparations. For consistency, we will refer to them as a single unit, the cochlear nucleus, in the dorsomedial region of the medulla. While this does not confirm the non-existence of two distinct nuclei, the projections present were concentrated in the caudal aspect of the cochlear nucleus, suggesting a proclivity of terminals to target the region of nucleus angularis, as nucleus magnocellularis is expected to be located further rostral (Warner, 1935). The vestibular nuclei identified include the medial vestibular nucleus (VM), the descending vestibular nucleus (VDesc), the ventrolateral vestibular nucleus (Deiter's, VVL), and the dorsolateral vestibular nucleus (VDL). We did not find a superior vestibular nucleus, which is consistent with Weston, (1936), though this was only found in turtles. These nuclei were identified in the dorsal half of the brainstem, situated near the midline. The tangential nucleus was not readily distinguished in either snake. The vestibular nuclei take up a larger rostrocaudal extent than the cochlear nuclei, which were much more confined.

3.3.2. *Organization of the Scarpa's ganglion*

The VIIIth nerve enters the brainstem at the level of the superior olive and the root is approximately 400 μm in width in both snakes. The VIIIth ganglion, also called Scarpa's ganglion (Alexander, 1901), was reconstructed from the sections based on fluorescing cell bodies in *C. atrox* and a predicted lateral projection is shown in Figure 3.2A-G. *C. hortulanus* was shown to have a similar organization (Figure 3.2H). Afferents from the posterior and anterior branches of the VIIIth nerve arrive at the ganglion separately, with the cell bodies from the posterior branch (innervating the posterior canal as well as the auditory structures) located dorsally in the caudal half of the ganglion (red). Originally described as a dorsal (cochlear) and ventral (vestibular) root of the VIIIth nerve (Weston, 1936), the ganglia is separated into two populations of cells. However, since the cochlear root also contains projections from the posterior canal, and in the snake both branches are situated in the same horizontal plane, we will refer to the cochlear root as the posterior branch, and the vestibular root as the anterior branch. Ganglion cell bodies from the anterior branch, which receive projections from the anterior (blue) and horizontal (green) canals, are located ventrally in the rostral half of the ganglion and show a high degree of overlap. This mingling of cells in the centre of the ganglion is likely because the anterior and horizontal branches coalesce before reaching the ganglion, whereas the posterior branch remains separate until the ganglion itself. Further rostrally however, cell bodies receiving input from the anterior canal exist with minimal overlap.

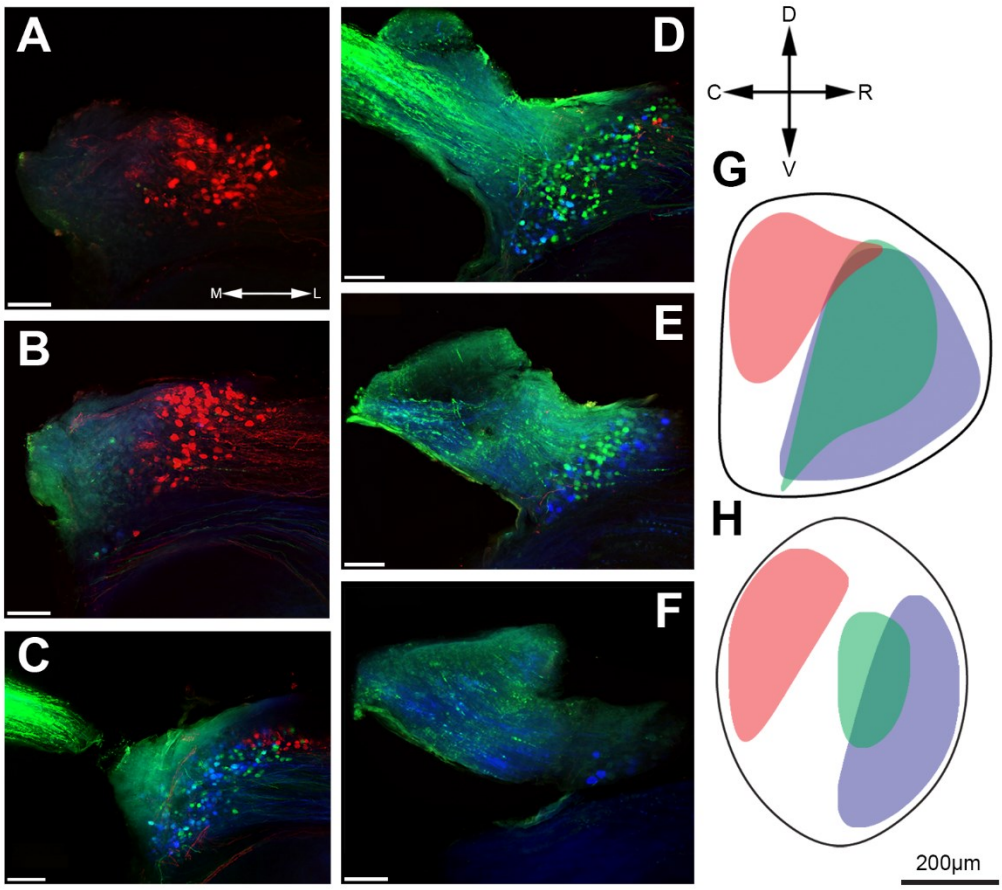

Figure 3.2: *Reconstruction of cell body organization in Scarpa's ganglion in C. atrox and C. hortulanus.* A-F: Serial coronal sections of the VIIIth nerve of *C. atrox* from caudal (A) to rostral (F). A reconstructed lateral view of the ganglia is shown in G, *Crotalus atrox* and H, *Corallus hortulanus.* Coloured regions represent area of cell body labeling within the nerve. Blue, anterior canal; green, horizontal canal; red, posterior branch; M, medial; L, lateral; D, dorsal; V, ventral; R, rostral; C, caudal. Scale bars in A-F = 100 µm.

3.3.3. *Auditory and vestibular nuclei in Crotalus atrox and Corallus hortulanus*

To map out and compare the two species of snakes, several notable nuclei were used as landmarks and are shown in Figure 3.3. The trigeminal motor nucleus and the Vth nerve root were identified as entering the brainstem rostral to the start of the VIIIth nerve in both species. The nucleus was identified at the same level as the respective nerve root, as a dense cluster of large, multipolar cells located ventrolateral to the vestibular nuclear complex. The superior olive

and the facial motor nucleus were located around the level of VVL, with the superior olive located ventrolateral to the reticular complex. The trigeminal motor nucleus spanned a large rostrocaudal range of *C. atrox* but was much more confined in *C. hortulanus.* The superior olive nucleus had the largest rostrocaudal extent across snakes, reaching almost 700 μm in length in one *C. atrox* sample (approx. 500 μm in *C. hortulanus*).

The cochlear nucleus was identified by small, densely packed cells in an oval shaped nucleus in the dorsomedial-most region of the brainstem. In both species, it is located just caudal to the entrance of the VIIIth nerve, and travels caudally to the obex, a narrowing of the 4th ventricle into the central canal that acts as a conventional boundary between the hindbrain and the spinal cord. VDesc was the largest nucleus in the complex, located lateral to the midline, and was dorsally bordered by the cochlear nucleus. Medially, VDesc was bordered by VM, which runs ventromedial to VDesc, adjacent to the 4th ventricle. Both nuclei travel to the obex caudally and were cut off sharply at the rostral aspect by VVL in *C. hortulanus* but had some overlap with VVL in *C. atrox*. VVL is a long flat nucleus, denoted by large diamond shaped cell bodies at the entrance of the VIIIth nerve. VVL was slightly more rostrally situated in *C. hortulanus*. This nucleus was very short, but wide in the mediolateral aspect. Finally, VDL was furthest rostral, traveling from the entrance of the VIIIth ganglion to the cerebellar peduncle. Overall, the organization of the vestibular nuclei were consistent in both snakes.

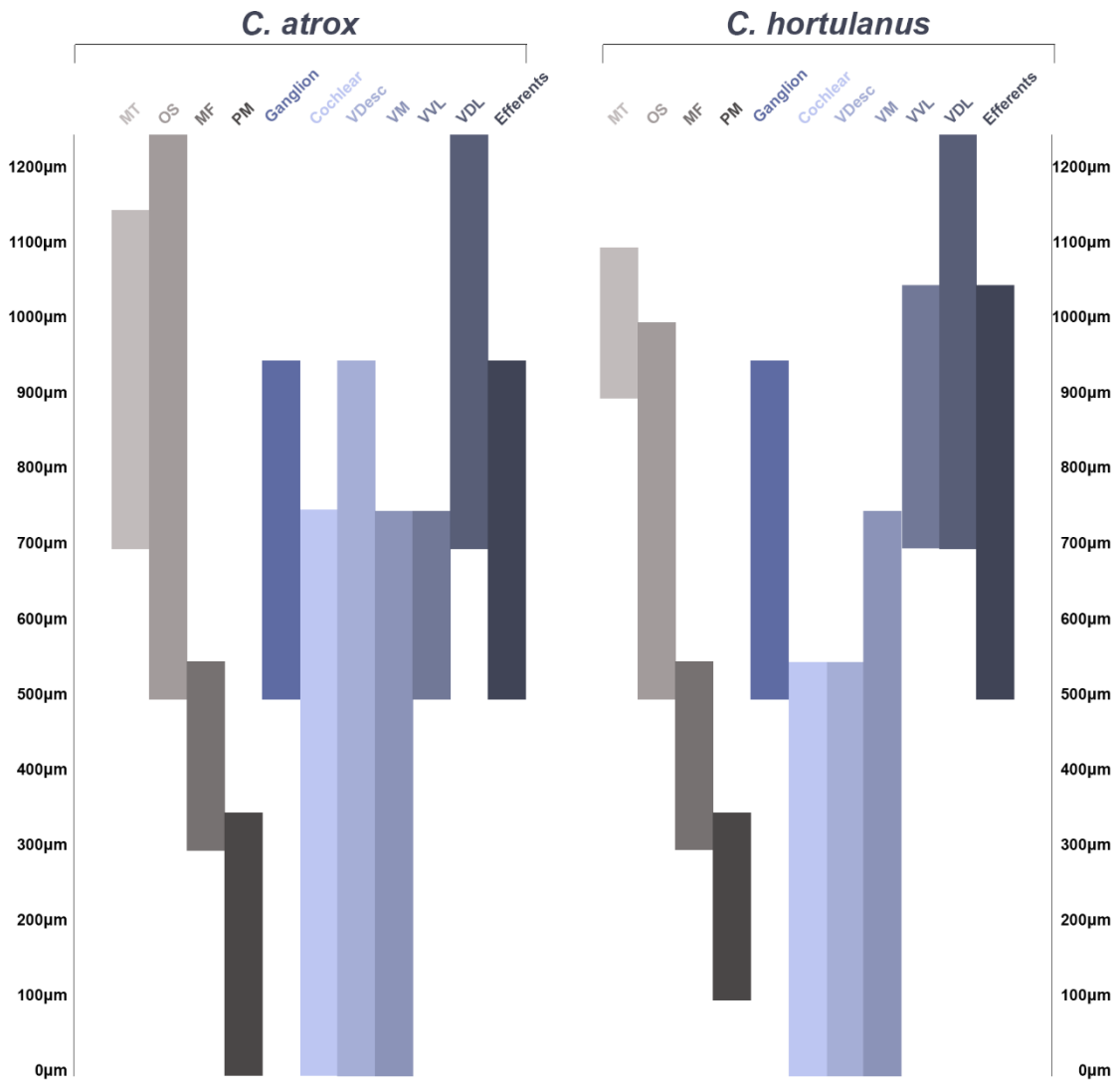

Figure 3.3: *Mapping of landmarks and vestibular nuclei in C. atrox and C. hortulanus.* Includes data from two *C. atrox* and three *C. hortulanus* snakes and aligned based on landmark nuclei. 0µm denotes the obex at the caudal most end of vestibular complex and appearance of vestibular nuclei and travels rostrally. Bars denote the appearance of nuclei, entrance of Scarpa's ganglion, and appearance of efferent cell bodies. MT, nucleus motorius ventralis n. trigemini; OS, nucleus olivarius superior; MF, nucleus motorius nervi facialis; PM, nucleus parvocellularis medialis; VDesc, descending vestibular nucleus; VM, medial vestibular nucleus; VVL, ventrolateral vestibular nucleus; VDL, dorsolateral vestibular nucleus.

3.3.4. *Primary vestibular projections to the brain stem*

All projections were seen in the ipsilateral side of the vestibular nuclear complex (Figure 3.4). The VIIIth nerve enters the brainstem at the level of the cochlear nuclei, and bifurcates into two branches, one ascending branch which goes to innervate more rostrally located nuclei such as the VDL, and a descending branch which travels to innervate more caudal nuclei such as VM and VDesc. All canals had projections that went through both ascending and descending tracts.

Terminals from the anterior and posterior canals appeared throughout the vestibular complex in both snakes, with the horizontal canal terminals appearing in sections nearby the VIIIth nerve root. Interestingly, horizontal terminals in *C. atrox* appeared in more caudal sections, with very few terminals reaching the VDL, whereas horizontal branch terminals showed a more rostral bias in *C. hortulanus* with virtually no terminals present in the cochlear nucleus. Consistently, terminals from the three canals were oriented with the posterior terminals terminating in the dorsomedial-most aspect of the nuclear complex, with the anterior branches ventrolateral to that, and the horizontal terminals ventrolateral to the anterior branches.

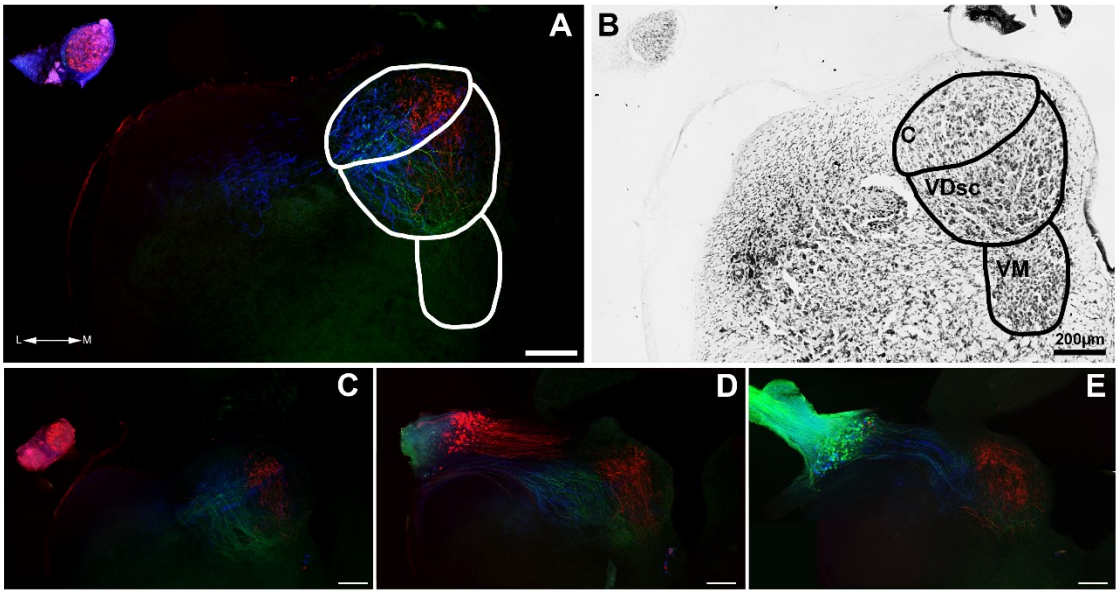

Figure 3.4: *Tri-colour tracer distribution of primary vestibular afferents to the vestibular nuclear complex in C. atrox from caudal (A) to rostral (E).* Note the inversion of the colour scheme for this figure. A, C-E show fluorescent images of the anterior canal (red), horizontal canal (green) and posterior branch (blue) taken at 10X.Sections were then Nissl stained and used as reference to identify nuclei containing terminals (B). C, cochlear nucleus; VDsc, descending vestibular nucleus; VM, medial vestibular nucleus; L, lateral; M, medial. Scale bars = 200 µm.

The cochlear nucleus received projections from the anterior, horizontal, and posterior canals in *C. atrox,* with the horizontal canal appearing in further rostral sections (Figure 3.5). The anterior projections terminated in the central region of the nucleus, whereas the posterior canals terminated dorsomedially. The horizontal terminals were found in the ventrolateral aspect of the cochlear nucleus, after traveling through the termination zones of the anterior canal. The nucleus expands the same length in *C. hortulanus,* however projections from the horizontal canal were not seen in the cochlear nucleus in all samples. There were anterior terminals within the central region of the nucleus, with the posterior canal terminating in the centro-ventromedial aspect. The horizontal canal from one sample terminated in the ventrolateral aspect.

The VDesc is one of the largest vestibular nuclei in these two species of snake and received projections from all three canals. While there were horizontal canal fibres coursing through the nucleus, few terminals were seen rostral to the cochlear nuclei in *C. atrox,* while horizontal terminals of *C. hortulanus* were only seen in the rostral most part of VDesc. Terminals arising from the anterior canal of *C. atrox* projected to the central region of the nuclei, with a lateral bias in rostral regions. Horizontal terminals laid lateral to anterior terminals. The posterior canal terminated consistently in the dorsomedial aspect of the nuclei, with terminals traveling ventrally in the nucleus towards the central area. In *C. hortulanus* this pattern was continued, with anterior projections terminating to the central aspect of the nucleus, traveling more laterally in rostral regions. Horizontal terminals appeared ventral and lateral to anterior terminals, and posterior terminals were found in medial regions of the nuclei.

VM is one of the longer nuclei within the vestibular complex of both snakes but is small in cross section and located adjacent to the fourth ventricle. *C. atrox* shows much fewer projections to VM, with only a small region receiving terminal endings from each canal. Again, the posterior branch terminates dorsally, with the anterior terminals lying ventral to that, and the horizontal ventrolateral to the anterior canal projections. *C. hortulanus* showed much more extensive projections arising from all branches to VM. Anterior projections appear more rostrally to the horizontal and posterior projections and terminate in the dorsal-central aspect of the nuclei. The horizontal projections consistently terminate in the ventrolateral aspect of the nucleus but were only present in a few sections. The posterior terminals were consistently dorsal, becoming more dorsolateral in rostral sections.

VVL is easily distinguished due to large motor-like cell bodies oriented in a long S shaped nucleus traveling mediolaterally at the level of the vestibular nerve entry. VVL receives

input from all branches in both snakes, with anterior projections centro-medial to the nucleus, horizontal projections ventromedial in caudal aspects of the nuclei, and posterior projections terminating in more medial regions of the nuclei in *C. atrox*. *C. hortulanus* also had horizontal canals terminating in more caudal regions of the nuclei and expressed the same termination orientation as *C. atrox.*

VDL is the most rostrally located nucleus in the vestibular complex and travels up into the cerebellar peduncle in both species. Some overlap was seen between anterior and posterior projections in *C. atrox*, but showed a mediolateral distribution of terminals, with posterior terminals more medial, anterior lateral to that, and horizontal terminals most lateral, but only in the caudal aspect of nuclei. *C. hortulanus* showed more terminals of all three branches but showed the same mediolateral distribution between posterior, anterior, and horizontal projections.

In summary, these projection patterns were relatively conserved between *C. atrox* and *C. hortulanus*. There is a consistent pattern of the posterior canal terminating in more dorsomedial regions of the brainstem, with the anterior canal terminals ventrolaterally positioned, and the horizontal canals terminating in yet more ventrolateral regions (see Figure 3.5, 3.6) There was some overlap in terminations between canals, however, after averaging across animals, the majority of terminals were present in separate but adjacent regions of the vestibular complex.

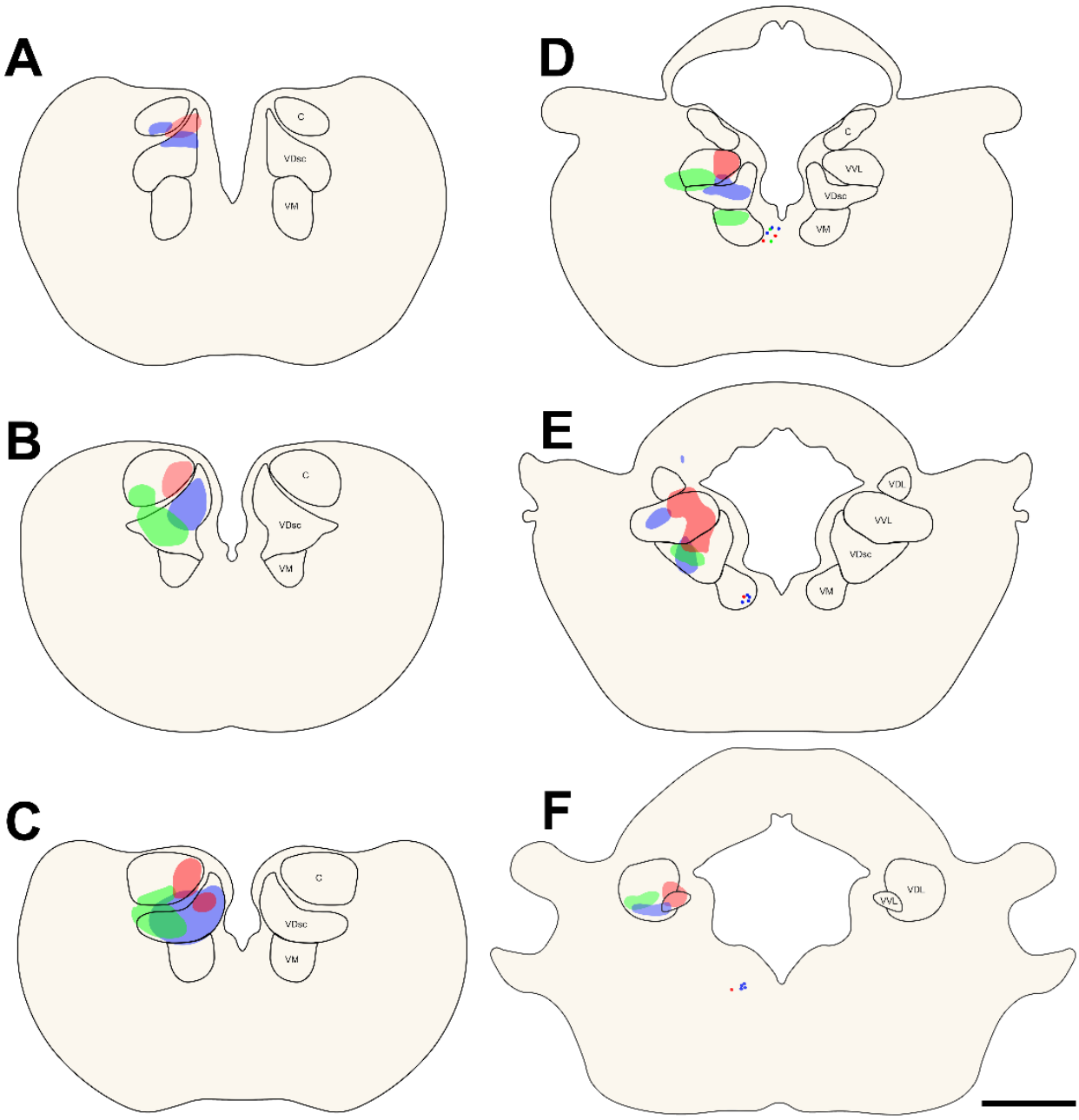

Figure 3.5: *Terminal endings from the anterior, horizontal canals and posterior branch in C. atrox, sample CA06.* Projections of the VIIIth nerve shown in coronal sections from caudal (A) to rostral (F). A single mossy fibre from the anterior canal can be seen in the lateral cerebellum in E. Efferent cells can be seen ventrolateral to the floor of the 4th ventricle in sections D-F. Blue, anterior canal; green, horizontal canal; red, posterior branch; C, cochlear nucleus; VDsc, descending vestibular nucleus; VM, medial vestibular nucleus; VVL, ventrolateral vestibular nucleus; VDL, dorsolateral vestibular nucleus. Scale bars =1000 µm.

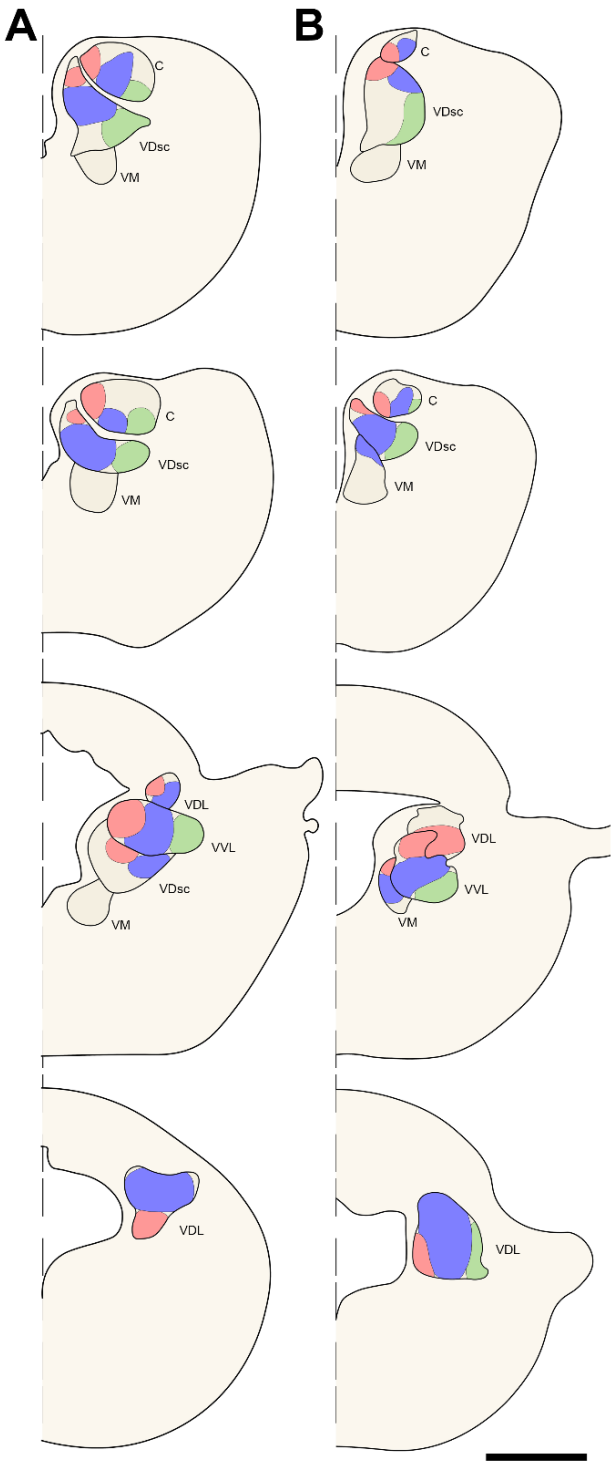

Figure 3.6: *Average terminal endings of the VIIIth nerve in C. atrox and C. hortulanus.* Data was collapsed over two C. atrox (A) and three C. hortulanus (B) cases. Blue, anterior canal; green, horizontal canal; red, posterior branch; C, cochlear nucleus; VDsc, descending vestibular nucleus; VM, medial vestibular nucleus; VVL, ventrolateral vestibular nucleus; VDL, dorsolateral vestibular nucleus. Scale bars =1000 µm.

3.3.5. *Primary vestibular projections to the cerebellum*

There were very few mossy fibres seen projecting to the cerebellum by 48h following tracer application (Figure 3.7). The mossy fibres seen were from the anterior and posterior branches in the anterior most section of the cerebellum, which corresponds to the base due to the flipped orientation (Aspden et al., 2015). Mossy fibre rosettes were found in the medial region within the cerebellar peduncle. No fibres were seen crossing the midline, nor were any fibres arising from the horizontal canal located. It is possible that there were projections that traveled further into the cerebellum; however, we saw no fibres traveling beyond the rosettes, suggesting that this was the terminal end of any fibres we traced.

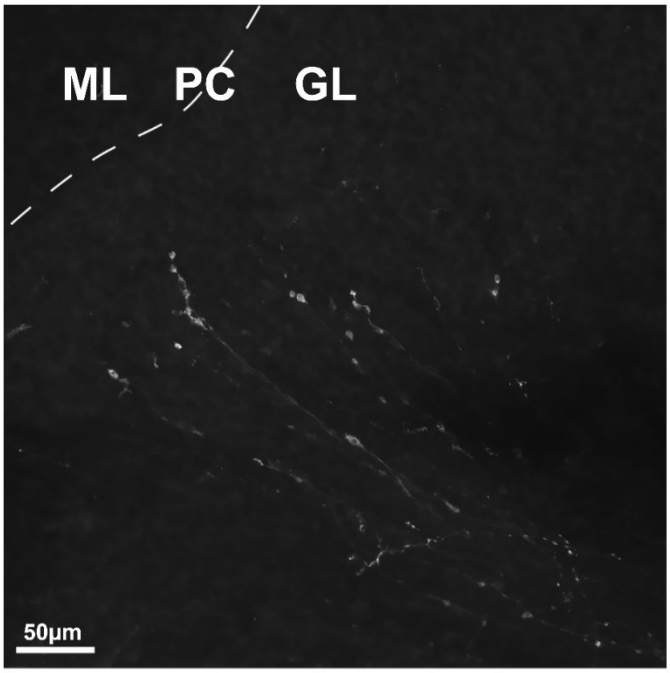

Figure 3.7: *Anterior canal projections terminating as mossy fibres to the lateral region of the anterior cerebellum in C. hortulanus.* Both posterior and anterior canals projected to the cerebellum as mossy fibres in both species (posterior not shown). Dashed line indicates Purkinje cell layer (PC). ML, molecular layer; GL, granule cell layer.

3.3.6. *Efferent cells*

Projections to the efferent cell clusters in both snakes travel caudally after entering the brainstem through the VIIIth nerve. At the level of nerve root, 29 total (range: 2-12 per snake, *C. atrox* avg = 7, *C. hortulanus* avg = 7.5) efferent cell bodies across five snakes were labeled with tracer from each of the canals, with some fibres traversing over the midline. Terminations of those fibres were not visible however, likely due to the duration of tracer transfer allowed. The locations of efferent cells varied between the species of snake, with the population of efferent cell bodies in *C. atrox* located more dorsolaterally, whereas *C. hortulanus* had a single cluster of efferent cells located alongside the midline ventral to the 4th ventricle (see Figure 3.8). This allowed for *C. atrox* to have two defined clusters bilaterally, which is consistent with other species (Goldberg and Fernandez, 1980; Dickman and Fang, 1996), whereas *C. hortulanus* only had a single, centrally located population (Figure 3.8). *C. atrox* efferent clusters were slightly caudal than those in *C. hortulanus*. There were a few cases of double labeling between all branches, but no cases of triple labeling, suggesting that any association may be limited to two canals at the level of the efferent cells.

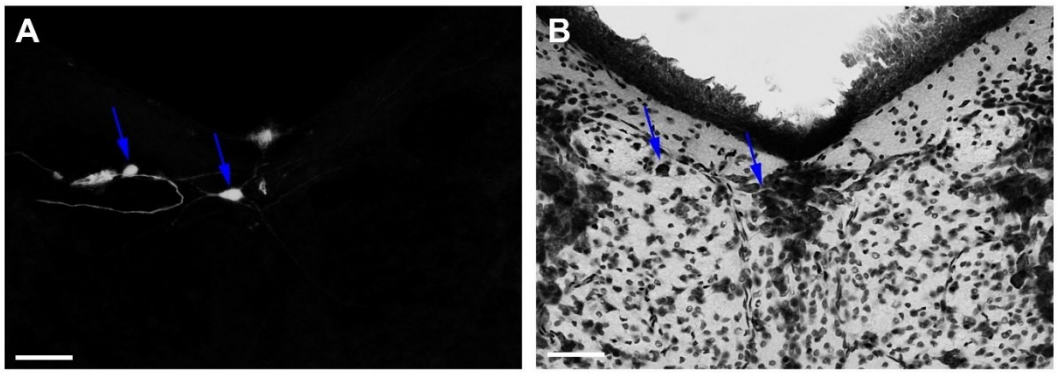

Figure 3.8: *Efferent cells in C. hortulanus from the anterior canal.* Corresponding fluorescent (A) and Nissl stained (B) images show cell bodies, with matching cell bodies labeled by blue arrows. *C. hortulanus* had efferent cell clusters in a single group ventral to the midline, while *C. atrox* had two bilaterally placed efferent cell groups dorsolaterally to the midline adjacent to the 4th ventricle. Scale bar = 50 μm.

3.4. Discussion

This project discusses the projection patterns of the VIIIth nerve in two species of snake and provides the first example of all three semicircular canals being compared simultaneously in a single preparation. In addition, we describe the projection patterns of each canal to the vestibular nuclear complex in two species of snake.

3.4.1. *Whole mount ex vivo preparation for anatomical tracing experiments*

The first description of the primary terminations of the vestibular complex was completed in 1885 by Flechsig and Bechterew, but the description was limited to projections of the either the vestibular (anterior) or cochlear (posterior) branch of the VIIIth nerve. Up until now, attempts to map out the vestibular projections have been limited to tracing primary afferents from a single canal per preparation (Kuruvilla et al., 1985; Dickman and Fang, 1996). Further, most experiments have been limited to tracing the entire anterior or posterior branch, combining the projections between anterior and horizontal canals in the anterior branch (Matesz, 1979; Miller and Kasahara, 1979; Barbas-Henry and Lohman, 1988; Burian and Gstoettner, 1988). In addition, all previous experiments used *in vivo* preparations. This experiment is the first instance where all three canals were stained simultaneously, within a single animal. This allows the advantage of comparing projections directly, without the need to account for natural variability between samples. The whole mount preparation provides access to the entire brain, and the *ex vivo* maintenance of the brain allows multi-day tracer transfer for long-distance transport. Despite using a different preparation, we were still able to match the same transfer times as the aforementioned studies, but the small size of the juvenile brains allowed even further transfer.

3.4.2. *Crotalus atrox and Corallus hortulanus share similar vestibular projection patterns with other vertebrates*

The organization of the vestibular and cochlear nuclei has changed little overtime, with similar organizations being found across vertebrates (Wilson and Felpel, 1972; Straka et al., 1997; Dickman and Angelaki, 2002; Highstein and Holstein, 2006). Primary afferent termination of the VIIIth nerve has been described in several vertebrates, including the monitor lizard, frog, pigeon, cat, and monkey, (Stein and Carpenter, 1967; Matesz, 1979; Mannen et al., 1982; Barbas-Henry and Lohman, 1988; Dickman and Fang, 1996), with each of the four major vestibular nuclei receiving inputs from all canals. The overall projection pattern to the vestibular nuclear complex is relatively consistent across vertebrates, but with some minor differences between the individual canal projections, primarily in the more rostral nuclei. Both *C. atrox* and *C. hortulanus* share similar projection patterns to the monitor lizard and frog, such that the posterior canal favours the dorsal regions of all described vestibular nuclei, while the anterior canal terminates ventromedially (Honrubia et al., 1985; Barbas-Henry and Lohman, 1988). Data from pigeon, monkeys, and cats were similar in more caudal nuclei, but the posterior canal projected more ventrally in rostral nuclei (Stein and Carpenter, 1967; Mannen et al., 1982; Dickman and Fang, 1996). Fibre diameter was not investigated in this project.

Terminations in the cerebellum were similar to those seen in snakes by others (Bangma, 1983), as well as in other reptiles studied, however we failed to see and horizontal canal afferents terminating as mossy fibres (frog, Matesz, 1979; cat, Mannen et al., 1982; pigeon, Schwarz and Schwarz, 1983; frog, Suarez et al., 1985). Because horizontal afferents have been traced in all other species listed above, we believe our tracer did not carry to the furthest reaches of the axon, and that there are indeed horizontal canal afferents terminating in the snake cerebellum. The termination pattern was similar as we only saw vertical canal afferents in a small region of the

cerebellum, traveling through the cerebellar peduncle and into the more lateral regions of the cerebellum. This is consistent with the projection location described by Mannen et al. (1982) and Honrubia et al. (1985) as the terminations traveled towards the cerebellar auricle, which has been likened to the flocculus (Larsell, 1926). However, it should be noted that there are slight variations across species and even within species, but the overall projection pattern seen here corresponds to other reptiles. This confined termination pattern contrasts to the purported theory that the snake cerebellum is only a vestibulocerebellum, and it is likely that there are afferents originating from other areas terminating in the cerebellum.

The efferent cell clusters were also similar to those studied in other animals, with *C. atrox* also having the clusters present bilaterally, which was consistent with pigeons and monkeys (Goldberg and Fernandez, 1980; Dickman and Fang, 1996).

3.4.3. *The primary vestibular system maintains separation between similar sensory features but lack upper levels of organization present in other sensory systems.*

In addition to the conservation of the general vestibular projection patterns, we also saw a consistent separation in the projections, which was previously difficult to describe in previous preparations. Recall the hypercolumns mentioned in the introduction. Each hypercolumn represents a receptive field, and each column contains groups of neurons sensitive to lines of different orientations within that receptive field (Hubel and Wiesel, 1963; Hubel et al., 1977). There are columns in somatosensory cortex for each receptive field too, each receiving slow and rapidly adapting mechanoreceptor projections that terminate in adjacent regions (Mountcastle, 1997; Kandel et al., 2000). Both systems share the higher level of organization of receptive fields and creates a repeating pattern as each receptive field has sensory projections for each stimulus feature collected. The vestibular system, however, does not have a traditional receptive field, as

its activation occurs through motion of the entire system. However, we see the same separation in projections of each canal. They each detect a direction of rotational acceleration, so it appears that the separation is between these features within the sensory system. Possibly, due to the lack of traditional receptive fields, the vestibular system projects to the vestibular nuclear complex as "one receptive field", but, similar to the other sensory systems, maintains separation between similar features collected by the system. However, this is not an absolute rule, as we did see some instances of overlap between terminals, but this may due to the visualization of terminals projecting to nearby neurons. Recordings from secondary vestibular neurons show that 88% of neurons receive input from a single canal only, with 10% receiving from two canals, and only 2% receiving input from all three canals (Straka et al., 1997), so while some degree of overlap is possible, the majority of secondary neurons appear to receive input from a single canal, supporting the theory of canal separation.

Are there further divisions within these clusters of cells that receive input from one of the three canals? The other sensory features detected within the vestibular labyrinth are accelerations due to translational movement, as opposed to rotational. The otolith organs, the utricle and saccule, detect acceleration in the horizontal and vertical planes respectively. There are reports that most secondary vestibular neurons receiving input from a single canal are occasionally paired with inputs from the otolith organs (Wilson and Felpel, 1972; Straka et al., 1997; Dickman and Angelaki, 2002). This functional innervation is conserved across frogs, primates, and pigeons, which suggests that this physiology would be consistent in the snake, which shares similar canal termination patterns. Our present experiment supports this theory that secondary vestibular neurons are primarily innervated by afferents from a single canal, however terminations from the otoliths may be overlapping. It would be interesting to see if there is a

repeating pattern of otolithic inputs (utricle and saccule) to each termination region of the semicircular canals.

3.5. Limitations

We saw only a few horizontal canal terminals, despite seeing many labeled cell bodies in the ganglia. This may be perhaps the uptake of the tracer was limited, as the canal was always stained with the same colour, whereas we have samples where the anterior and posterior tracers were alternated. This may have influenced our conclusion on the extent on the horizontal terminals, and in fact they may innervate much wider regions of the vestibular nuclear complex than seen in this project. As well, this would influence our conclusion on only seeing vertical canal fibres traveling to the cerebellum, and in fact there may be horizontal afferents terminating as mossy fibre rosettes in the granular cell layer, however our transfer time may have been too short for the transport of the green fluorophore. Further, the limited transfer time may cause us to underestimate the number of vertical canal projections to the cerebellum, however we did not notice a difference between our 24 and 48 h preparations, suggesting we had maximized our projection distance at 24 h and the extra day did not allow any further transfer. The molecular weight of the tracers is another concern, as the blue tracer had a much smaller molecular weight of 573 Da compared to 3 kDa, however since similar results were seen between samples where posterior and anterior tracers were flipped (Neurobiotin (573 Da) and Texas Red (3000 Da)), we are not concerned with this influencing our results. It is still possible however, that Dextran Fluorescein had poor uptake, transfer, or even visualization in this preparation.

3.6. Future Directions

Following the physiological data from Straka (1997), we would like to trace the projections from the otolithic organs. This would allow us to see if there is indeed a convergence of signals between an otolith and semicircular canal on a single secondary neuron. Not only would this perhaps unveil a further organizational layer within the primary vestibular system, this integration of translational and rotational signals may provide an interpretation of biologically relevant information that these neurons are specifically tuned to, and perhaps yet another pattern of neurons designated by function would emerge.

As well, to further investigate other afferent inputs to the ophidian cerebellum, we would also like to trace spinocerebellar and corticocerebellar projections in the snake brain to confirm the presence or absence of the spinocerebellum and neocerebellum in the snake. Since we only saw projections from the vestibular system terminating in the base of the snake cerebellum, which corresponds to the posterior lobe due to the inverted positioning, it is possible that the rest of the cerebellum receives inputs from other regions of the nervous system. The follow up experiment would involve the injection of retrograde tracers into the anterior lobe of the cerebellum and tracing fibre terminations in the spinal cord and the forebrain of the snake.

3.7. Conclusion

The vestibular system is an ancient sensory system seen in a wide range of vertebrates and has remained remarkably unchanged over time. We found consistencies within two species of snake that occupy different ecological niches, and these consistencies were also shared in other non-reptilian vertebrates. Because of the unique preparation used, this project has also highlighted a further, less discussed result of the consistent separation of terminals based on the semicircular canals they originate from. In the context of other physiological data collected from

single secondary neurons, we support the idea that there is a separation of similar sensory inputs maintained at the level of primary sensory cortex, and these provide just a single layer of organization. Despite lacking certain characteristics other sensory systems have such as multiple receptive fields, the same general organizational principles are adhered to, where similar features collected within a system are maintained separately. This is consistent with other instances in sensory cortex with a hierarchical, modular system, where divisions are driven by stimulus features. The next chapter will investigate another level of sensory processing, where these modular systems maintain and exploit this separation of features, but integrate between sensory systems.

Chapter 4: Modulation of complex spike activity in Zebrin immunopositive and immunonegative regions in the pigeon (*Columba livia*) vestibulocerebellum

This work was completed under the supervision of Dr. Douglas Wylie, from September 2015 - April 2018.

Abstract

The cerebellum is composed of parasagittal stripes as defined by its inputs, outputs, and molecular expression. The most common molecular marker studied is aldolase C, also known as Zebrin II (ZII), which is expressed in an alternating pattern where you have regions on Purkinje cells that express ZII, (ZII+), interdigitating with regions of Purkinje cells that express little to no ZII (ZII-). However, the function of these ZII+/ZII- stripes is yet to be elucidated. In the pigeon vestibulocerebellum, a ZII+/- stripe pair represents a functional unit and contain Purkinje cells that are all sensitive to a particular pattern of optic flow stimuli.

Using the pigeon vestibulocerebellum as a model, we investigate electrophysiological differences between these ZII+ and ZII- halves within a functional unit. We hypothesize that, because of the segregated inputs and outputs traveling to ZII+ and ZII- zones, there will be electrophysiological differences between the two groups of cells.

Through single cell recordings from ZII+ and ZII- Purkinje cells within the pigeon vestibulocerebellum, we found that ZII+ cells exhibited greater modulatory depth compared to ZII- cells in response to their preferred optic flow stimuli. We suggest that these differences are due to differing circuitry within each ZII+/- stripe, including inputs originating from different sensory modalities. This separation of sensory input to each stripe may participate in the fine tuning of the vestibulo-ocular reflex, by integrating inputs from both visual and vestibular sensory systems.

This separation of features is common within other sensory systems, and this project provides an example of how the separation of features may help in the integration between sensory modalities to achieve fine tuned responses to sensory stimuli.

Abbreviations

ANOVA	analyses of variance
AOS	accessory optic system
CF	climbing fibres
CS	complex spike
CTB	cholera toxin subunit B
HA	horizontal axis neurons
IO	inferior olive
LM	lentiformis mesencephali
LTD	long-term potentiation
LTP	long term depression
MI	modulation index
nBOR	nucleus of the basal optic root
PC	Purkinje cells
PCA	principle component analysis
ph	prepositus hypoglossi
PSTH	peristimulus time histogram
SI	sensitivity index
SR	spontaneous firing rate
SS	simple spike
VA	vertical axis neurons
VbC	vestibulocerebellum
VM	medial vestibular nucleus

VeS	superior vestibular nucleus
VOR	vestibulo-ocular reflex
ZII	Zebrin II

4. Introduction

Regions within the brain that process similar features have a patterned, modular organization, which can be used to construct a more comprehensive representation of a stimulus. The evidence of constancy seen in the organization of these modules across species highlights the importance of their existence. In the context of comparative neurobiology, we can see in real time the evolution of many sensory systems, from work conducted in planktonic larvae (Randel and Jékely, 2016), to the seminal work done in *Limulus* by Hartline et al. (1956), to current work on the primate eye. By tracing the evolutionary path of the organization of sensory systems, one common trait has emerged: a repeating, modular, hierarchical design. Within these sensory modules, commonly there are submodules, and we are still learning that even the simplest regions of the brain can be further broken down into simpler functions. This project will introduce another instance where function can be further subdivided within a modular sensory system.

4.1.1. *Gross cerebellar organization*

The cerebellum is one of the oldest structures of the brain, as well is the densest in terms of neuronal cell count (Lange, 1975; Herculano-Houzel, 2010). Housing more than 80% of the neurons in the brain, this density must be highly organized. Indeed, the cerebellum shows a repeating structure, as defined in work by Cajal (Ramon y Cajal, 1911). In fact, Cajal has stated that this circuit is so invariant that it constitutes a “law of biology” (Cajal 1911, Sultan and Glickstein 2007).

There are three layers that make up the cerebellar cortex that were mentioned in Chapter 3: most superficially lies the molecular layer, which contains the Purkinje cell (PC) dendrites and the axons of granule cells. The axons of the granule cells bifurcate and run parallel to the surface

of the cortex (hence their name, parallel fibres), orthogonally through the PC dendritic arbour. The PC somata are arranged in a layer one cell thick and make up the PC layer. Subjacent to the PC layer are the densely packed granule cell bodies, which give rise to the parallel fibres that course through the molecular layer. Interspersed in these layers are several classes of interneurons, including brush, basket, stellate, Lugaro, and Golgi cells (Barmack and Yakhnitsa, 2008; Craciun et al., 2019).

The mammalian cerebellum can be divided into a three parts: a medial section called the vermis, derived from the Latin term for "worm", two hemispheres, and a flocculonodular lobe (Glickstein and Voogd, 2009). Classically, these divisions have been linked to function based on the input each receives, with the vermis receiving spinocerebellar afferents (spinocerebellum), the hemispheres receiving cerebro-cerebellar afferents (cerebrocerebellum), and the flocculonodular lobe receiving vestibular afferents (vestibulocerebellum). Finally, there has been another naming device for these three divisions based on phylogeny: the neocerebellum (hemispheres), corresponding to the development of the hemispheres seen in late branching vertebrates such as mammals, the paleocerebellum (vermis), and the archicerebellum. The archicerebellum, or vestibulocerebellum, is named as it is the oldest phylogenetically (Larsell 1937). The vestibulocerebellum (VbC) offers a useful model for investigating cerebellar function, due to its overall conservation of structure across vertebrates (Pakan et al., 2007). To properly investigate the consistently patterned architecture and its role in physiology, it is important to pick a system that is evolutionarily conserved, such that connective patterns can be observed in the context of other organisms to help contribute potential ideas towards links to behaviour.

4.1.2. *Avian cerebellum*

The avian model offers many advantages to study the VbC as avian visual systems are very similar to humans as, compared to rats, they are diurnal, have accurate vision at distances, and are abundant. As well, the pigeon (*Columba livia*) has been studied for many years, often spurring many discoveries that are then made in mammals, and as such, the anatomy is well documented. There are also numerous similarities in gross morphology, histology and circuitry between the avian and mammalian cerebellum (Pakan 2007, Craciun 2019, Llinas and Hillman 1969)

4.1.3. *Vestibulocerebellum*

The VbC inputs and outputs have also been extensively documented (Langer et al., 1985; De Zeeuw et al., 1994b; Ruigrok, 2003; Voogd and Wylie, 2004; Pakan et al., 2008, 2010, 2014; Wylie et al., 2017; Craciun et al., 2018), as well as there have been some strides to start to define the function. The inputs to the VbC arrive via two sources. Mossy fibres synapse onto granule cells, and arise from the vestibular system, the spinal cord, and visual nuclei such as the lentiformis mesencephali (LM), and the nucleus of the basal optic root (nBOR). The second source of input come as climbing fibres (CF), which arise only from the medial column of the inferior olive. Outputs from the VbC travel via the PCs, which are the sole carrier of outgoing information from the cerebellum, down to the deep cerebellar and vestibular nuclei. There are two lobes within the pigeon VbC; folium IXcd and folium X, and interestingly, in folia IXcd, these inputs and outputs have been highly correlated with parasagittal zones (Pakan et al., 2010, 2014).

4.1.4. *Patterns within the VbC: Parasagittal zones*

While the cerebellum exhibits distinct structural regularity in cellular architecture across regions, there have been repeated anatomical and neurochemical descriptions of "zones" oriented parasagittally across the cerebellum (Apps and Hawkes, 2009). While there are many ways to elucidate this striking pattern, one of the most common ways has been through the immunoreactivity of PCs to the metabolic isoenzyme, aldolase C (Ahn et al., 1994), commonly referred to as Zebrin II (ZII). ZII is expressed in PCs in such a way that there are regions of cells that are positive for ZII expression (ZII+) that alternate with regions of PCs that express low to no ZII (ZII-), and this pattern is mirrored across the midline (see Figure 4.1A-B). This striped pattern is highly conserved across species, with high overlap between the avian and mammalian cerebellum (Sillitoe et al., 2005). In folium IXcd of the VbC, there are 7 pairs of +/- stripe pairs on each side of the VbC, and each consist of PCs that are directionally selective to particular patterns of visual optic flow (Graham and Wylie, 2012).

4.1.5. *Optic flow*

As mentioned in the introduction, the primary visual system breaks down stimuli into rudimentary features, which are then integrated with other visual inputs to be more representative of the true stimuli. The VbC, part of the accessory optic system, processes visual information in a similar fashion, selectively being tuned to a single aspect of the visual stimulus but is representative of something much larger (Simpson, 1984). Optic flow describes the large-scale, panoramic motion across the retina, created by movement of the organism through space. Similar to the modular organization of motion sensitive cells in visual cortex, PCs within the VbC are organized based on the direction of visual stimuli they process (Graham and Wylie, 2012).

To elaborate, in 2012, Graham and Wylie showed that clusters of directionally selective PCs are organized such that, in folium IXcd, they span a single ZII+/- stripe pair, termed a functional unit (see Figure 4.1C). There are several types of optic flow detected in pigeons and are organized with translational optic flow PCs being located more medially in the uvula (stripes P1-2, folium IXcd), and the rotational optic flow PCs located laterally in the flocculus (P4-7). PCs in the P1+/P1-med stripe pair are tuned to Contraction optic flow, which is generated as the pigeon moves away from an object. As pigeons have laterally set eyes, this optic flow field appears to move in a temporal to nasal direction. The next stripe pair, P1-lat and P2+med, have two types of interspersed PCs, responding either to Expansion optic flow (nasal to temporal motion), or Ascent optic flow (downward visual motion). Descent optic flow (upwards visual motion) cells are found in P2+lat/P2-. There is currently no description of visually sensitive PCs in stripes P3+/-. The PCs within the flocculus contain rotationally selective neurons. PCs in functional units P4+/P4- and P6+/P6- respond to rotation about a vertical axis (VA cells) arising from the midline, and PCs in functional units P5+/P5- and P7+/P7- respond best to rotation about a horizontal axis, oriented 45^{o} from the midline (HA cells). Folium X shares the same organization of optic flow sensitivities as the overlying uvula and flocculus, however all PCs are ZII+ (Pakan et al., 2007; Graham and Wylie, 2012). Mammals have been shown to share the same visual sensitivities (Graf et al., 1988; Yakusheva et al., 2013).

Remarkably, the rotationally selective neurons share the same frame of reference as the semicircular canals. The direction of optic flow VbC PCs are most sensitive to are generated by head rotations that maximally activate individual semicircular canals (Wylie and Frost, 1993; Wylie et al., 1998). For example, the horizontal semicircular canals are most sensitive to detect

rotation of the head about a vertical axis (eg. turning head left and right). This generates a left-right visual motion, which are detected by the VA PCs in the P4+/- and P6+/- functional units.

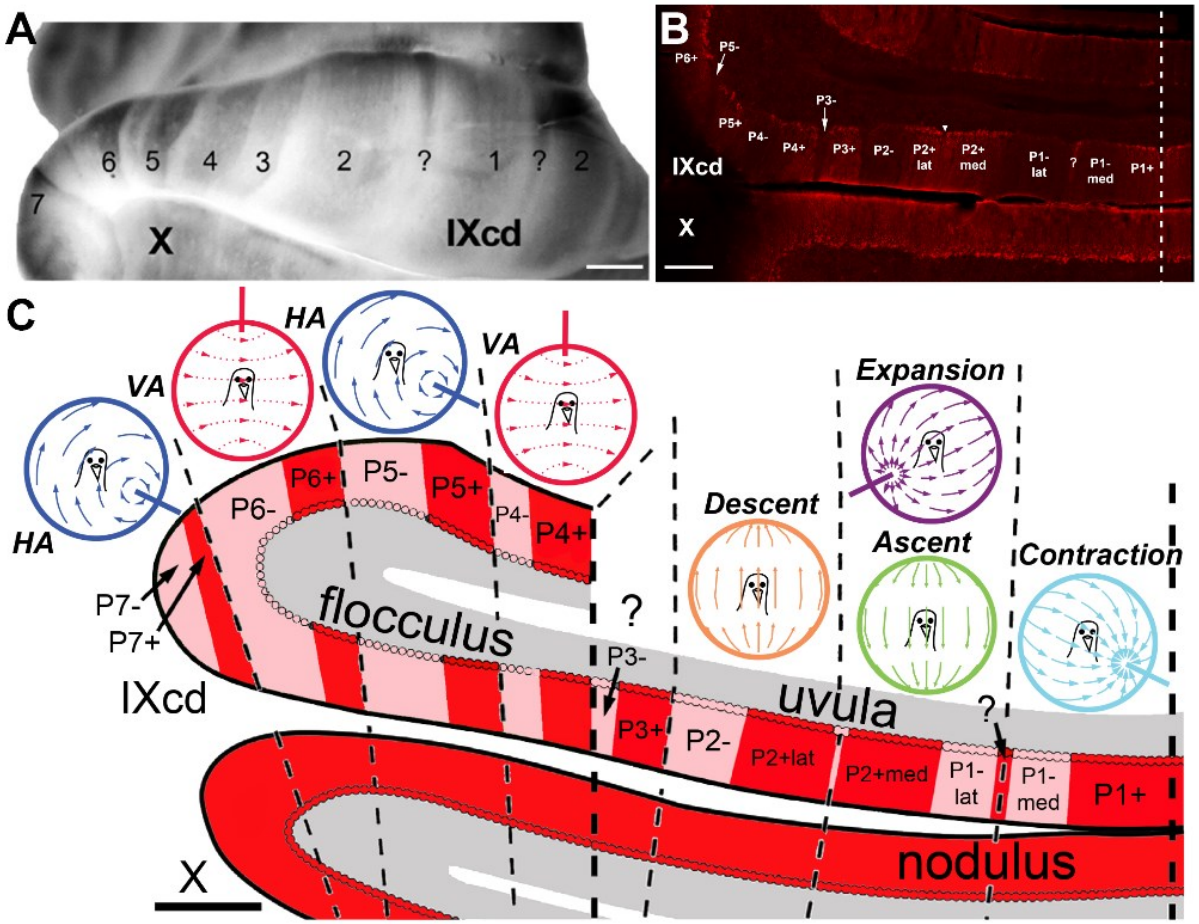

Figure 4.1: *Zebrin (ZII) expression in the pigeon vestibulocerebellum.* A: a whole mount of the pigeon vestibulocerebellum (folia IXcd and X) stained for ZII, with stripes indicated with numbers (adapted from Pakan et al 2007). Stripe 1 spans the midline. The ? between P1-lat and P1-med indicates a satellite ZII+ stripe that divides P1- into medial and lateral sections. B: immunoprocessed coronal section through IXcd and X stained for ZII. The arrow denotes a notch of no PCs dividing P2+ into medial and lateral halves. Note P7+/- is not visible. C: schematic of the section shown in B, showing ZII zones and the respective optic flow preference of the PCs. The uvula, which includes P1+, P1-med/lat, P2+med/lat, and P2- respond to translational optic flow, while P4+/-, P5+/-, P6+/-, and P7+/- respond to rotational optic flow. P3+/- has not been shown to exhibit any optic flow sensitivity. Scale bars: A = 500 μm, B = 300 μm, C = 400 μm. HA, horizontal axis; VA, vertical axis.

4.1.6. *Electrophysiology of Purkinje cells*

Recall the two main sources of input from section 4.1.3. PCs exhibit two distinct forms of action potentials, each arising from the two main sources of input in the circuit: simple spikes (SS), which arise from over 100,000 synaptic connections from parallel fibres onto the PC distal dendrites, and complex spikes (CS), which arise from the CFs synapsing on the proximal dendrites (Napper and Harvey, 1988). The waveforms of these spikes differ as well, with the CS exhibiting a longer duration, and being of a much greater amplitude. As well, a CS is composed of two parts, an initial sodium spike, followed by a calcium-driven plateau (Eccles et al., 1966; Schmolesky et al., 2002). Further, a CS causes a characteristic pause in SS firing from the PC, named the SS pause (Granit and Phillips, 1956; Simpson et al., 1996; De Zeeuw et al., 2011). In pigeons, it is the CS activity that is modulated by optic flow, and the focus of this project.

As the inputs to the VbC respect the boundaries defined by ZII zones, it is possible this will appear as variations in the electrophysiological signatures between them. Recently, there have been several studies trying to link ZII expression to distinct electrophysiological patterns. One notable finding demonstrates that ZII+ and ZII- PCs appear to differ with respect to mechanisms of synaptic plasticity during motor learning: ZII+ PCs tend to rely more on long term potentiation (LTP), and ZII- PCs rely on long term depression (LTD, Wadiche and Jahr, 2005; Paukert et al., 2010; Wang et al., 2011; Ebner et al., 2012, 2012; Hawkes, 2014; Zhou et al., 2014).

Following Graham and Wylie's (2012) description of ZII+/- PCs within a functional unit exhibiting the same optic flow sensitivities, we wanted to investigate if there is a difference in the modulation of CS activity between the ZII+ and ZII- cells within a functional unit.

4.2. Methods

4.2.1. *Animal care*

Electrophysiological recordings were obtained from 36 pigeons of either sex (*Columba livia*) obtained from a local supplier. All experiments were carried out according to approved standard operating procedures and complied with the University of Alberta Biosciences Animal Care and Use Committee, following guidelines set from the Canadian Council on Animal Care.

4.2.2. *Surgery and electrophysiological recording procedures*

Animals were anaesthetized using a cocktail of ketamine (65 mg/kg) and xylazine (8 mg/kg), injected intramuscularly, with supplemental doses to maintain surgical plane. Once the animals were fully anaesthetized, they were placed in a stereotaxic device (David Kopf Instruments, Tujunga, CA), adapted with pigeon ear bars and beak adaptor, such that the orientation of the skull conformed to the atlas of Karten and Hodos (1967). Recordings were obtained throughout the extent of the VbC, including the uvula (medial IXcd), the nodulus (medial X), and the flocculus (lateral IXcd and X) on the left side of the brain. The flocculus was accessed by removing the bone dorsal to IXcd and was enclosed within the radius of the anterior semicircular canal. To access the uvula and nodulus, the bone above the dorsal surface of folia VI and VII was removed, and penetrations were made vertically. Extracellular single unit recordings were made with glass micropipettes filled with a 2 M NaCl solution dyed with Fast Green, and pulled to a tip diameter of 3-5 μm. Electrodes were positioned and advanced using a hydraulic microdrive, and raw signals were amplified, filtered, and digitized using a data analysis system (1401plus, Cambridge Electronic Design, Cambridge, GBR), sampled at 16-33 kHz. Data analysis was done offline using Spike2 Software (Cambridge Electronic Design).

4.2.3. *Visual motion stimuli*

Complex spike (CS) activity recorded from the molecular layer was identified by a negative polarity action potential and lack of SS activity, whereas CS activity recorded from the Purkinje cell layer was identified by a positive CS action potential, with high frequency SS activity present in the negative polarity. CS activity was identified by a characteristic spontaneous firing rate of 1 Hz. This were further confirmed qualitatively with responsiveness to visual optic flow by moving a large stimulus within the visual field. This method has been used previously to identify CS activity (Pakan et al., 2011, 2014; Graham and Wylie, 2012). The stimulus was quite large, (~100° x 100° visual degrees) and consisted of visual noise (black lines and dots on a white background). This stimulus was moved by hand in various directions throughout the visual field while the modulation of the CS activity was monitored. This allowed the approximate location of the recording to be established; for example, a Descent cell shows preference for upward motion throughout the visual field and are localized within the ZII stripe pair P2+lat or P2-. Once a cell was adequately isolated, CS activity was then collected quantitatively, by projecting a large field visual stimulus onto a screen measuring 90° x 75° (height x width) that was positioned in the frontal visual field of the bird. The stimuli consisted of a drifting sinewave grating of an effective spatial and temporal frequency (0.5 cycles/degree at 0.5 Hz; Winship et al., 2005). Direction tuning was established by measuring CS firing frequency to motion in eight directions, 45° apart (Figure 4.2A). A sweep consisted of the grating moving in one direction for 5 s, followed by a 4 s pause, then 5 s motion in the opposite direction, followed by a 7 s pause (Figure 4.2B). A single trial consisted of 4 sweeps, such that

all 8 directions were presented, and responses were averaged over 3 to 8 trials per cell, depending on the stability of the signal.

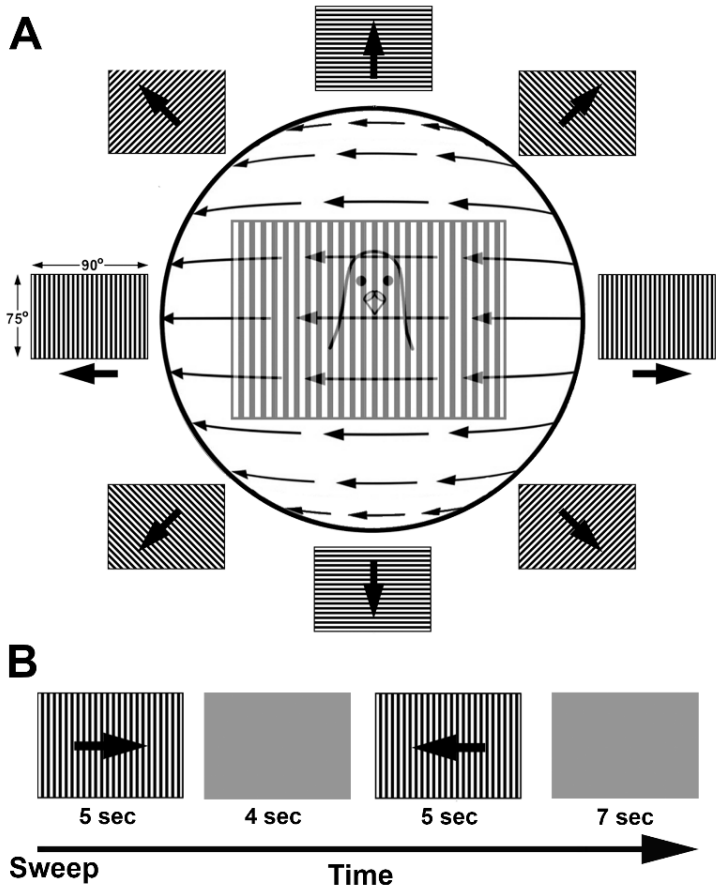

Figure 4.2: *Representation of stimulus presentation for CS direction tuning.* A: A large sinewave gradient was presented to the animal in its frontal field drifting in eight directions, 45° apart. B: Each sweep consisted of 5 seconds of motion drifting in one direction, followed by a 4 second pause, followed by 5 seconds of motion drifting in the opposite direction, followed by a 7 second pause. Each sweep was repeated until all 8 directions were presented, which constituted one trial.

4.2.4. *Recording site localization*

In order to track the ZII signature of multiple recorded cells in a single animal, recordings were obtained from up to three penetrations in the folia, each 100 μm apart in the medio-lateral dimension. At the last recording site, a small injection of fluorescent tracer was made such that

all recording locations could be reconstructed using stereotaxic coordinates. A glass micropipette (20 μm tip diameter) containing a 1% solution of cholera toxin subunit B (CTB, Life Technologies, Carlsbad, CA) replaced the recording micropipette, and the location was qualitatively verified through CS activity identification as described above. Once the location was determined, CTB was iontophoresed (4 μA; 7 s on, 7 s off) for 4 min at the same recorded depth as the recordings. This reliably resulted in CTB injections that were ~50 μm in diameter (see Figure 4.3K). Note that CTB was only used to mark locations and was not used as a retrograde tracer. We calculated our accuracy at injecting in a previously marked recording site at 34.6±6.6 μm (mean±SEM). Therefore, we discarded any data where the recording site was within 50 μm of a ZII+/- border within a functional unit. We are confident with this procedure in assigning ZII signatures to previously recorded cells, however we must acknowledge a limitation, as not all PCs within a ZII+ stripe are ZII+, and not all PCs in a ZII- stripe are ZII- (Wylie et al., 2017).

4.2.5. *Tissue harvesting and immunostaining*

At the end of all recording experiments, pigeons were deeply anaesthetized with an overdose of sodium pentobarbital (100 mg/kg) and were immediately perfused transcardially with PBS (0.9% NaCl, 0.1 M phosphate buffer), followed by ice cold 4% PFA in 0.1 M PBS, pH 7.4. The birds were decapitated, and the brains extracted and placed into 4% PFA at 4°C for 2 days. The brains were then cryopotected in 30% sucrose/0.1 M PBS until they sank and were embedded in 10% gelatin and cryoprotected once more. Frozen serial sections of the cerebellum were cut using a sliding microtome at 40 μm in the coronal plane. The tissue was then processed for ZII expression using previously established immunohistochemical techniques previously

described (Pakan et al., 2007, 2010, 2014; Graham and Wylie, 2012). Floating sections were rinsed in 0.1 M PBS for 3 x 5 min and blocked in a 10% normal donkey serum (Jackson ImmunoResearch Laboratories, West Grove, PA) and 0.4% Triton X-100 in PBS for 1 h at RT while shaking. Tissue was then incubated in 0.1 M PBS containing 0.1% Triton X-100 and the primary antibody, goat anti-Aldolase C (1:1000, sc-12065; Santa Cruz Biotechnology, Dallas, TX), for 5 days at 4°C while shaking. Sections were then rinsed 3 x 5 mins in PBS, and then incubated in the secondary solution for 3 h at RT while shaking (0.1 M PBS, 2.5% normal donkey serum, 0.4% Triton X-100, 1:200 Alexa Fluor 594, (Jackson ImmunoResearch), or Alexa Fluor 488 (Jackson ImmunoResearch)-conjugated AffiniPure donkey anti-goat secondary). The tissue was then rinsed once more 3 x 5 minutes in PBS before being mounted onto gelatinized slides, dried, and viewed with a compound light microscope (Leica DMRE) equipped with appropriate fluorescence filters (rhodamine and FITC). Images were acquired with a Retiga Exi FAST Cooled Mono 12-bit camera (Qimaging, Surrey, BC) and Openlab imaging software (Improvision, Coventry, GBR). Adobe Photoshop (Adobe, San Jose, CA) was used to adjust for brightness and contrast.

4.2.6. *Spike sorting analysis*

Spikes were sorted using Spike2 software, where an amplitude threshold was chosen to isolate spikes of interest. Spikes above threshold were then subjected to a template matching algorithm, which compared the shape of the waveform to subsequent spikes. In addition to qualitative assessments based on shape, the spikes were clustered based on a principal component analysis (PCA) in Spike2, which considered various aspects of the waveform including the position and amplitude of maxima and minima, duration, area under the curve, etc. A PCA graph was created (see Figure 4.3 F, J) where the three axes represent the top three

components that explain the most variance in descending order. For example, PC1 explains the most variance between the two populations, and PC2 explains the next most variance between the populations, etc. We only considered multiple spikes from a single recording to be arising from two different cells if the clusters in the PCA were non-overlapping (see Figure 4.3F, J). We further required the spontaneous firing rate of CSs to be consistent across the recording, near 1 Hz, with a minimal interspike interval of at least 100ms.

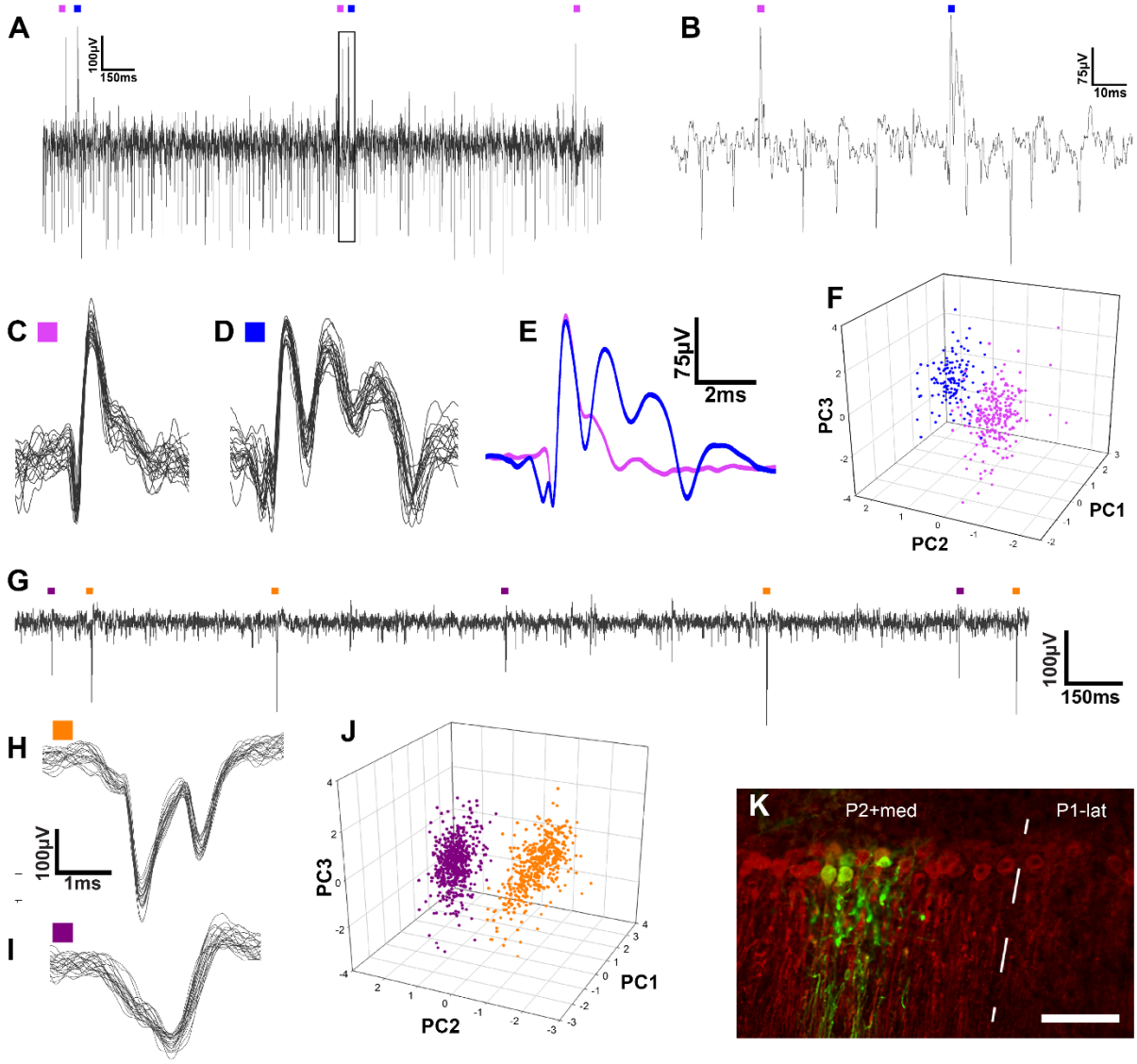

Figure 4.3: *Representative electrophysiologic recordings from the Purkinje cells in the vestibulocerebellum.* Recordings made from the Purkinje cell layer (A-F) show CS activity with a positive polarity, and the presence of SS activity (negative polarity). B is an expanded view of the boxed region in A. CS activity from two different cells were found using the Spike2 sorting software, and are denoted in pink and blue squares in A-F. Overlays of 20 CS of each type are shown in C and D, with the average waveform in E. Thickness of the line represents ±1 SEM. Although similar in amplitude, the two waveforms have clearly different profiles. F shows a principle component analysis graph generated by Spike2 for the two waveform populations shown in C and D. The axes PC1, 2, 3 refer to principle components generated by the PCA analysis in descending order of the variance explained. The two waveform clusters show minimal overlap, demonstrating that the waveforms are different in multiple aspects. G-J show a recording from the molecular layer, with the absence of SS and a negative polarity CS. Two CS

waveforms (orange and purple squares) were isolated. 20 waveforms are overlaid in H and I, showing two distinct waveforms. Note the difference in amplitude at the molecular layer level. J: PCA of the two waveforms from recording shown in G. K: typical recording site marked with green cholera toxin subunit B in the P2+med zone. This section was stained for ZII (red). Scale bar in K = 100 μm.

4.2.7. *CS modulation analysis*

We only analyzed cells that had a minimum of 3 trials, although most cells (91/173) had at least 4 trials. Directional tuning curves were made by plotting the average firing rate (calculated from the total number of CSs divided by the total duration of a drifting grating moving in a particular direction) as a function of each direction of visual motion, plotted using polar coordinates (ie. rightward motion plotted at 0º, upwards at 90º, leftwards at 180º, downwards at 270º). A modulation index (MI) was then calculated for each cell using the following equation:

$$MI = \frac{FR_{max} - FR_{min}}{FR_{max} + FR_{min}},$$

Where FR_{max} and FR_{min} represent the absolute maximal and minimal average firing rate values respectively. As the depth of modulation increases, MI approaches 1. While FR_{max} represents the cell's response to the "preferred direction", this is limited to our sampling interval of 45°. FR_{min} was occasionally not in a direction exactly 180° opposite the FR_{max}, but it was almost always between 135-225º from the FR_{max}. The MI represents the range of firing rates a cell displays.

A sensitivity index (SI) was also calculated using the equation defined by Vogels and Orban (1994):

$$SI = \frac{\sqrt{(\Sigma_n FR_n \times sin\theta_n)^2 + (\Sigma_n FR_n \times cos\theta_n)^2}}{\Sigma_n FR_n},$$

Where FR_n represents the average firing rate to direction *n* and *n* represents each of the eight directions of motion presented. This returns the magnitude of the mean vector, a measure of how tightly a cell is tuned. A higher SI represents narrower directional tuning. The SI is equal to 1 if the neuron only responds to a single direction and is inhibited by any deviation to that direction.

4.2.8. *Statistical analyses*

Data was subject to analyses of variance (ANOVAs), using R (R core team, 2012). In case of interactions between variables, planned comparisons were made within functional units (ie. ZII+ VA vs. ZII- VA cells), using t-tests with the default holm adjustment out of concern for the sample sizes. For some planned comparisons where group sizes were small, the Holm-corrected tests may be considered overly conservative, so we also ran non-parametric tests (Wilcoxon rank sum, R).

4.3. Results

4.3.1. *Electrophysiological recording sites*

Complex spike (CS) activity was recorded from 173 PCs at 122 recording sites. The majority of recordings only contained CS activity from a single cell (80), however 42 recordings had complex spikes arising from multiple cells, isolated with spike sorting (see Figure 4.3). 22 recordings were obtained at the PC layer and were identified due to the positive polarity of CS as well as the presence of an SS pause (ZII+ = 30±12 ms (mean±SD), ZII- = 27±12 ms). Examples of PC layer recordings and molecular layer recordings can be found in Figure 4.3A-E and 4.3G-J

respectively. CS activity was recorded from 148 cells in folium IXcd, and 25 in folium X. 86 cells in IXcd were localized to ZII+ stripes, and 62 cells were localized to ZII- stripes. As all PCs in folium X are ZII+, we recorded 111 cells from ZII+ regions and 62 from ZII- cells. Cells were recorded from all optic flow stripes in the VbC however we were unable to record any cells from the thin P7+ stripe.

4.3.2. *Spontaneous firing rate*

The spontaneous firing rate (SR) was determined for each cell by calculating the frequency of CSs during a period with no visual stimuli. The distributions of SR for all ZII+ and ZII- cells is shown in Figure 4.4. The average SR was significantly higher in the ZII- cells (1.14±0.31 Hz, mean±SD) compared the ZII+ cells (0.97±0.31 Hz), even when separated by folium (Figure 4.4C; t-test; $p = 0.001$). This result is replicated in mice where ZII- cells showed an average SR of 1.13±0.25 Hz and 0.92±0.28 Hz in the ZII+ cells (Zhou et al., 2014). Based on a one-way ANOVA (ZII-, ZII+ (X), ZII+ (IXcd)), the groups were significantly different ($F(2,170) = 5.548$, $p = 0.005$). Planned comparisons confirm that the SR of ZII- cells was significantly higher than ZII+ cells in IXcd (t-test; $p = 0.002$), and in X (t-test; $p = 0.03$). The SRs did not differ between the two groups of ZII+ cells in IXcd and X (t-test; $p = 0.92$). Since CSs occur due to activity in the inferior olive, the consistently higher SR seen in ZII- cells suggests that there is a segregation of circuitry that is detectable even in the absence of physiological stimuli. This is in contrast with Graham and Wylie, (2012), where they describe a functional unit as a ZII+/- stripe pair, but it appears their function may be further delineated.

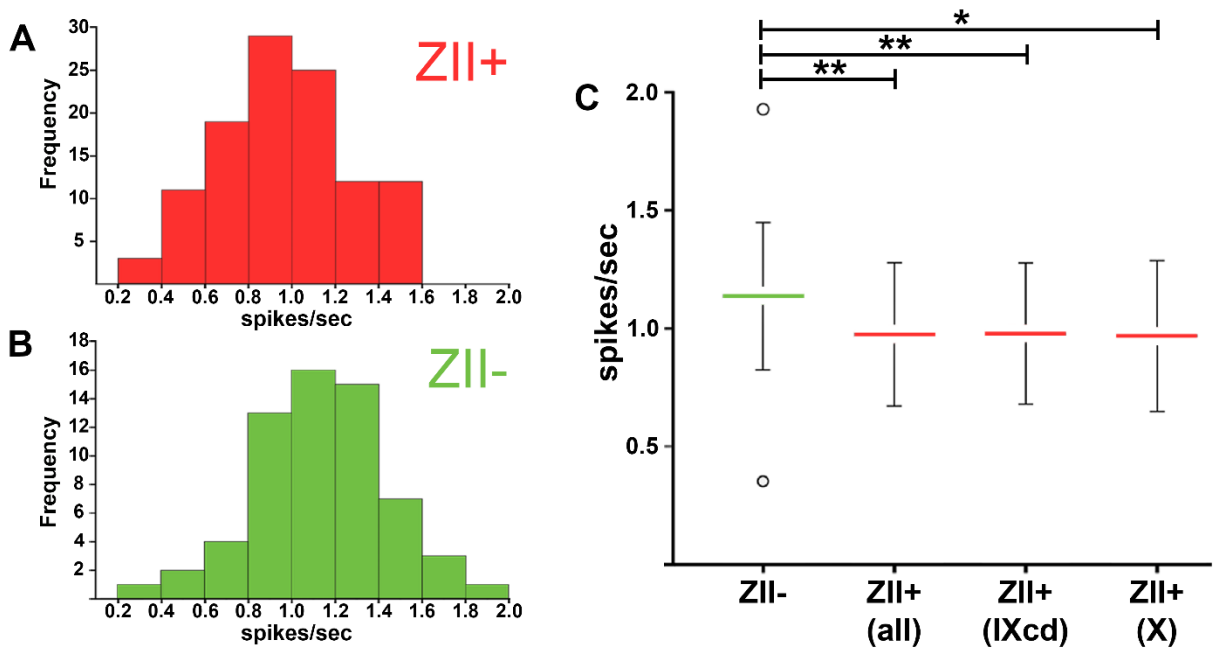

Figure 4.4: *Spontaneous firing rate (SR) of CS in ZII+ and ZII- PCs.* A-B: distributions of SRs of ZII+ PCs and ZII- PCs. C: average SR of all ZII- PCs, all ZII+ PCs, and ZII+ separated by folium (IXcd vs. X) is plotted with SD. Open circles denote outliers outside the 1st or 4th interquartile range. The ZII- PCs had a higher spontaneous firing rate of CSA relative to ZII+ cells (t-test, ZII- n = 62, ZII+ (all) n = 111, ZII+ IXcd n = 86, ZII+ X n = 25. ZII- vs ZII+ (all) $p = 0.001$, ZII- vs ZII+ IXcd $p = 0.002$, ZII- vs ZII+ X $p = 0.03$). *$p < 0.05$, **$p < 0.01$.

4.3.3. *Directional tuning of CS activity for ZII+ and ZII- cells*

Since PCs within the vestibulocerebellum (VbC) are directionally sensitive, we needed to control for each group's directional preference. This would allow us to compare the maximal excitation and inhibition rate in all groups of neurons to their respective preferred and anti-preferred stimuli. We calculated firing rates to all directions of stimulus presented and provide an example below in Figure 4.5 of VA neurons. VA cells prefer motion to the right and are inhibited by motion to the left. Figure 4.5 shows example traces of representative ZII+ and ZII- VA cells and their directional tuning of CS activity. Peristimulus time histograms (PSTHs) of their responses to motion in their preferred (right) and anti-preferred (left) directions are plotted in Figure 4.5C, E and I. Directional tuning curves are shown in Figure 4.5D, F, J, where the

average firing rate (spikes/s) is plotted as a function of direction in polar coordinates (black dots), and a curve was fitted to the data. The SR for each cell is represented by the grey circle. This allows us to visualize the change compared to SR in response to each stimulus direction. Note the oblong shape of the CS curve of the ZII+ cell in Figure 4.5D compared to the broader shape of the CS activity in the ZII- cell in Figure 4.5J. The asymmetry of the curve corresponds to the modulation index (MI, ZII+ = 0.81, ZII- = 0.41), with more asymmetrical curves representing a greater depth in modulation (greater change in firing rate compared to the SR). The narrow, pointed shape seen in the ZII+ cell is reflected in the sensitivity index (SI, ZII+ = 0.37, ZII- = 0.22), illustrating how the ZII+ cell is much more sensitive to a specific direction, and lowers its firing rate in response to deviations from that preferred direction. There is a lack of modulation in the SS activity (Figure 4.5E, F), which has been shown previously in ketamine-xylazine preps (Wylie et al., 1993), but has been detected in other models (Yakusheva et al., 2013). This data provides a visualization of the greater depth of modulation and sensitivity to visual motion ZII+ cells show compared to ZII-, as they exhibit greater excitation to motion in the preferred direction, and greater inhibition to motion in the anti-preferred direction.

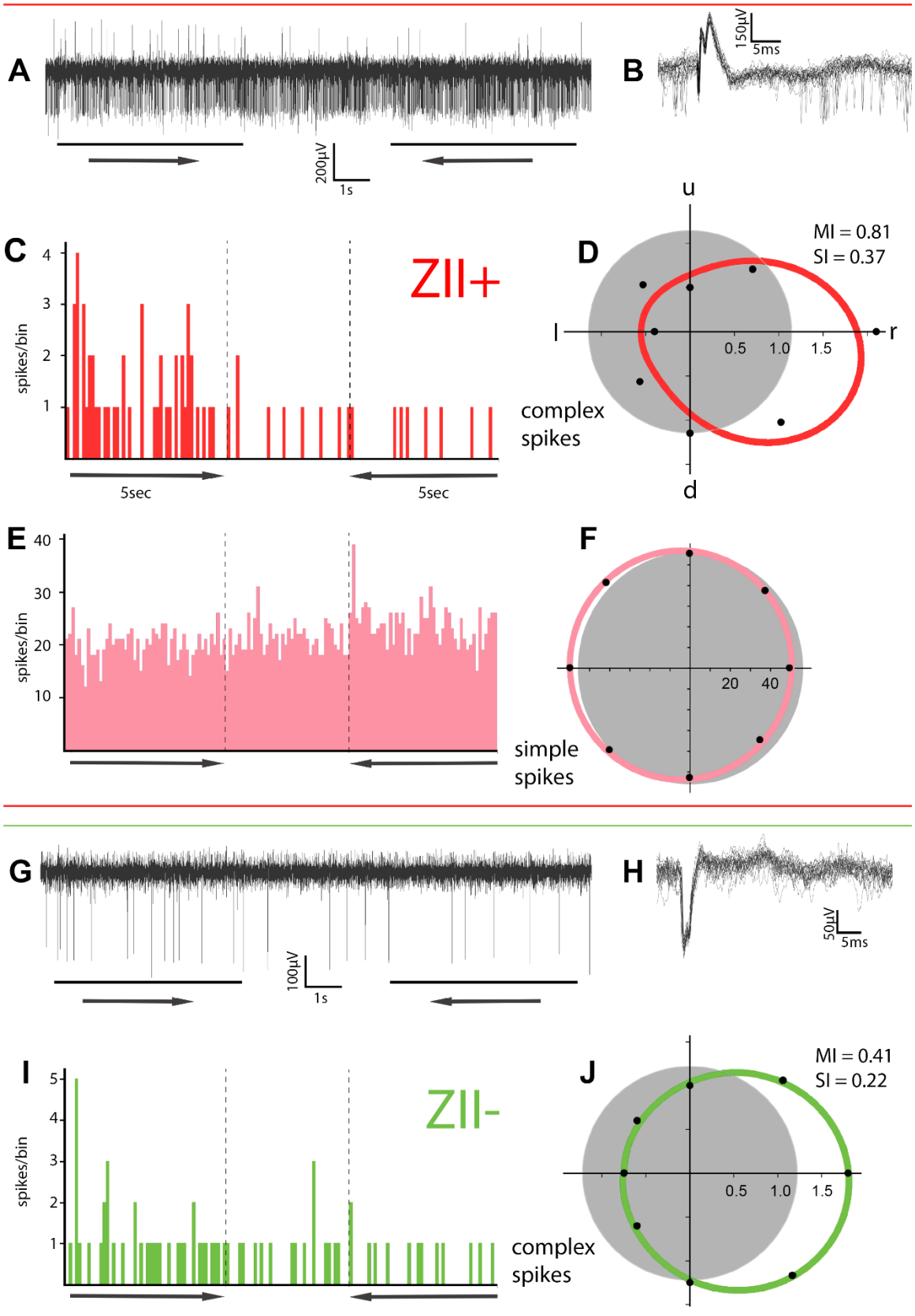
A
200µV
1s
B
150µV
5ms
C
ZII+
spikes/bin
4
3
2
1
5sec
5sec
D
u
l
r
d
MI = 0.81
SI = 0.37
0.5
1.0
1.5
complex
spikes
E
spikes/bin
40
30
20
10
F
20
40
simple
spikes
G
100µV
1s
H
50µV
5ms
I
ZII-
spikes/bin
5
4
3
2
1
J
MI = 0.41
SI = 0.22
0.5
1.0
1.5
complex
spikes

Figure 4.5: *Directional tuning of ZII+ and ZII- vertical axis (VA) Purkinje cells.* A-F data from ZII+ PCs. A: raw trace of CS activity from a Purkinje cell layer in response to 5 s motion in the preferred direction (rightward, black bar), followed by a 4 s pause, followed by 5 s of motion in the opposite (anti-preferred) direction (leftward, black bar). Note positive polarity of CS, while SS activity is negative. B: Overdraw of 20 CS from recording shown in A, also highlighting the SS pause following the CS. C: peristimulus time histogram (PSTH) of CS activity summed over 4 sweeps of motion to the preferred and anti-preferred direction. E: PSTH of SS from the same cell. SS does not show modulation in this preparation (see text). D, F: directional tuning curves for CS (D) and SS (F) where average firing rate (spikes/s) are plotted as a function of direction in polar coordinates (black dots). A Gaussian fit was fit to these plots (red, pink circles). Gray circle denotes spontaneous rate of the cell. G-J: Data is represented the same as A-F though these are from molecular layer recordings, thus SS is not present. u, up; d, down; r, right; l, left; MI, modulation index; SI, sensitivity index.

4.3.4. *Modulation and Sensitivity Indices of ZII+ and ZII- Purkinje Cells*

We calculated MI and SI for all cells, and the data is outlined in Figure 4.6 and Table 4.1. As we wanted to compare the ZII+ and ZII- cells within a functional unit (ie. ZII+ Descent vs. ZII- Descent cells), we performed a two-way ANOVA with ZII signature and functional unit as factors. Both VA functional units were combined as were the two HA functional units. Recall that MI is a measure of modulatory depth, with cells that exhibit dramatic increases and decreases in firing rate in response to preferred and anti-preferred stimulation having an MI value approaching 1. Cells that do not show changes to their firing rate would have an MI value would be approaching 0 and are not modulated by that stimulus. There were main effects of ZII signature for MI ($F(1,163) = 37.605$, $p = 6.3 \times 10^{-9}$) and functional unit ($F(4,163) = 12.105$, $p = 1.2 \times 10^{-8}$), with a significant interaction ($F(4,163) = 4.36$, $p = 0.002$). The main effect of ZII signature is shown in Figure 4.6C, with the average MI for ZII+ cells = 0.58±0.23 a.u. (mean±SD) and the average MI for ZII- cells = 0.39±0.18 a.u. The difference is maintained when comparing ZII- cells to ZII+ cells of either IXcd (t-test; $p = 2.4 \times 10^{-7}$), or X (t-test; $p = 1.4 \times 10^{-4}$). There was no difference between ZII+ cells in IXcd and X (t-test; $p = 0.43$). We plotted the

data divided by functional units in Figure 4.6D, with the results listed in Table 4.1. Note that the average MI for the ZII+ cells are consistently greater than the ZII- average MI in each functional group, which is likely driving the interaction. Although the number of cells varied between groups, the MI was significantly different for the Expansion/Ascent cells (t-test; $p = 8.1 \times 10^{-5}$) and VA units (t-test; $p = 0.005$) using parametric tests. Due to the lower sample sizes, we also used non-parametric statistics (Wilcoxon rank sum), and we saw that the Contraction group also becomes significantly different in MI ($p = 0.01$) in addition to the Expansion/Ascent ($p = 6.9 \times 10^{-5}$), and VA groups ($p = 7.4 \times 10^{-5}$). The higher MI in the ZII+ population suggests that ZII+ PCs exhibit greater excitation firing rates to their preferred directions and/or are more inhibited in response to their anti-preferred directions.

We also calculated the SI for each cell (shown in Figure 4.6E-H, Table 4.1). Recall that the SI represents how tightly tuned a cell it is to a particular direction and can be thought of as the magnitude of the vector sum of all responses. For example, cells that respond equally to all directions, or are broadly tuned, will have a vector sum close to zero which will result in an SI that approaches 0. Cells that are highly sensitive to a single direction will exhibit a larger vector sum, are more tightly tuned to that stimulus, and will have an SI that approaches 1. We saw similar trends as MI, with a main effect of ZII signature (two-way ANOVA; $F(1,163) = 43.431$, $p = 5.8 \times 10^{-10}$) and functional unit ($F(4,163) = 14.799$, $p = 2.5 \times 10^{-10}$), as well as a significant interaction ($F(4,163) = 4.297$, $p = 0.003$). The average SI was 0.26±0.14 a.u. (mean±SD) for the ZII+ cells, and 0.15±0.08 a.u. for the ZII- cells. Again, the difference of SI between ZII+ and ZII- cells is maintained even when the folia are analyzed separately (ZII- vs. ZII+ IXcd; t-test; $p = 1.1 \times 10^{-8}$, ZII- vs. ZII+ X; t-test; $p = 5.2 \times 10^{-5}$). There was no difference between the SIs for ZII+ cells in folium IXcd and X (t-test; $p = 0.41$). We show the data separated by functional units

in Figure 4.6H and Table 4.1, and see a similar pattern as we did in the MI. The SI is significantly different for the Expansion/Ascent (t-test; $p = 1.1 \times 10^{-4}$) and VA functional units (t-test; $p = 5.2 \times 10^{-4}$) using parametric statistics. The Contraction functional unit also shows significance when non-parametric statistics (Wilcoxon rank sum, R) are used ($p = 0.01$), alongside the Expansion/Ascent ($p = 8.0 \times 10^{-5}$) and VA ($p = 5.7 \times 10^{-5}$) functional groups. The greater SI values seen in the ZII+ cells suggest that these cells are much more sensitive to the actual direction of stimulus presented, showing a much quicker drop-in firing rate the further the stimulus is from its preferred direction.

Paired with the SR data, the larger MI and SI values seen in the ZII+ cells further support the idea that there is a discrepancy in the circuitry that innervates the ZII+ PCs, where the visual stimulus modulates the CS activity more effectively than ZII- PCs.

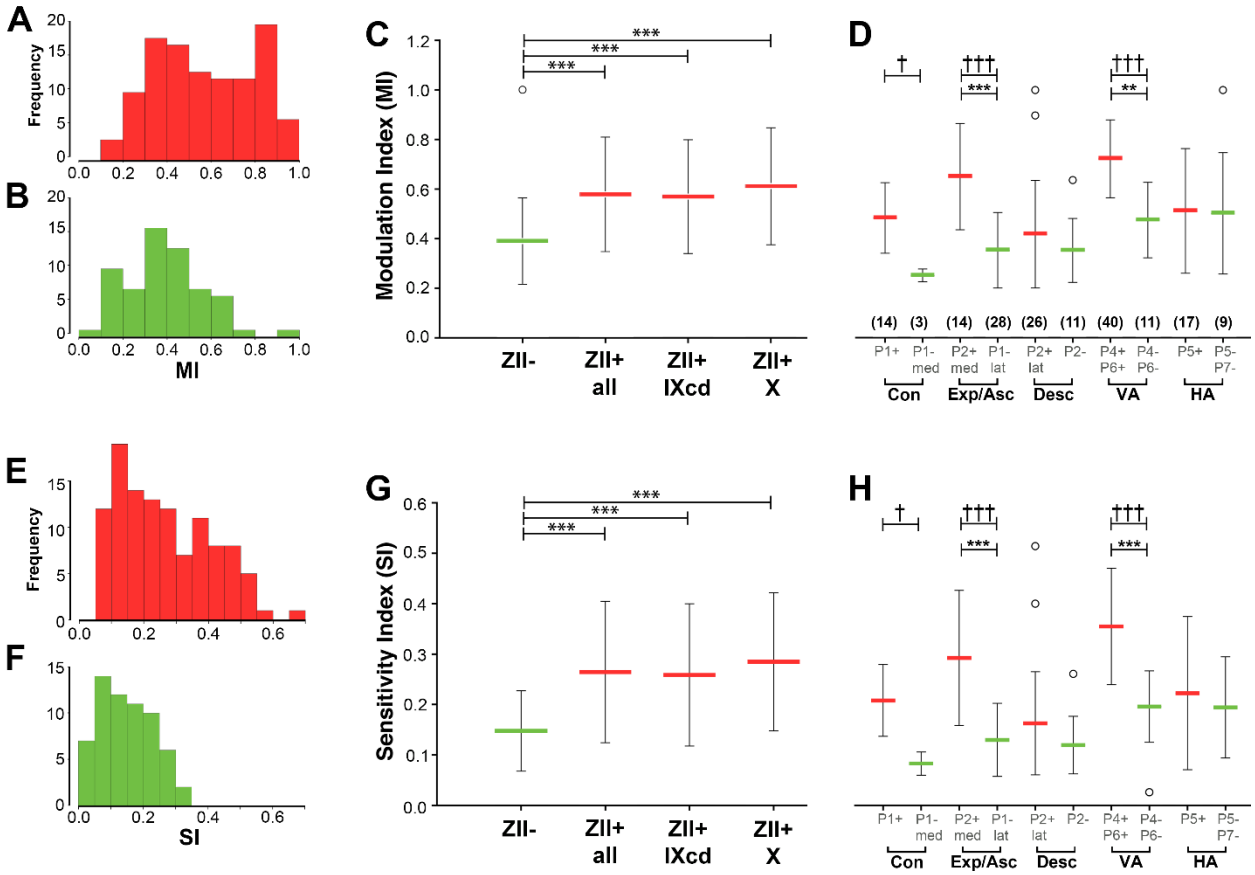

Figure 4.6: *Modulation (MI) and sensitivity (SI) indices for ZII+ and ZII- CSA.* A, B show distribution of MI values across ZII+ (red) and ZII- (green) PCs. C shows the mean ± SD of MI values between all ZII- PCs (n = 62), all ZII+ PCs (n = 111), and ZII+ PCs divided by folia IXcd (n = 86) and X (n = 25, ZII- vs ZII+ all $p = 8.1 \times 10^{-9}$, ZII+ IXcd $p = 2.4 \times 10^{-7}$, ZII- vs ZII X $p = 1.4 \times 10^{-4}$). Open circle denotes outlier outside the interquartile range. D: mean MI ± SD is shown for each individual stripe, so comparisons can be made within a functional unit. Brackets indicate n and apply to groups in H as well. E-H shows SI values in the same depiction as MI values in A-D (ZII- vs ZII+ all $p = 5.3 \times 10^{-11}$, ZII+ IXcd $p = 1.1 \times 10^{-8}$, ZII- vs ZII X $p = 5.2 \times 10^{-5}$). Outliers were included in analyses. (**$p < 0.01$, ***$p < 0.001$. Wilcoxon: † $p < 0.05$, ††† $p < 0.001$.) Con, Contraction; Exp, Expansion; Asc, Ascent; Desc, Descent; VA, vertical axis; HA, horizontal axis.

	Con		Exp/Asc		Desc		VA		HA	
	ZII+	ZII-	ZII+	ZII-	ZII+	ZII-	ZII+	ZII-	ZII+	ZII-
n	14	3	14	28	26	11	40	11	17	9
MI	0.48 ±0.14	0.25 ±0.03	0.65 ±0.22	0.35 ±0.15	0.42 ±0.22	0.35 ±0.13	0.72 ±0.16	0.48 ±0.15	0.51 ±0.25	0.50 ±0.25
p	1.00		$8.1x10^{-5}$*		1.00		0.005*		1.00	
p'	0.01*		$6.9x10^{-5}$*		0.68		$7.4x10^{-5}$*		1.00	
SI	0.21 ±0.07	0.08 ±0.02	0.29 ±0.13	0.13 ±0.07	0.16 ±0.10	0.12 ±0.06	0.36 ±0.12	0.2 ±0.07	0.22 ±0.15	0.19 ±0.10
p	1.00		$1.6x10^{-4}$*		1.00		$5.2x10^{-4}$*		1.00	
p'	0.01*		$8.0x10^{-5}$*		0.22		$5.7x10^{-5}$*		0.96	

Table 4.1: Averaged values of modulation index (MI), and sensitivity index (SI) for all recorded cells grouped by functional unit. Pairwise t-tests were used. Values of 1.00 have been inflated by the Holm adjustment and indicate non-significance. p values indicate results from pairwise t-tests. p' indicates results from the Wilcoxon rank sum test. Con, Contraction; Exp, Expansion; Asc, Ascent; Desc, Descent; VA, vertical axis; HA, horizontal axis.

Since the MI is a measure of the range of firing frequencies (ie. how high is the excitation firing rate, how low is the inhibited firing rate), it does not tell us which one is contributing to the magnitude of the MI. Therefore, we investigated whether the greater MI was related to either a greater increase in firing rate to preferred stimuli (excitation), or a greater decrease in firing rate to anti-preferred stimuli (inhibition). This is shown in Figure 4.7A for both ZII+ and ZII- cells, where the firing in response to the preferred stimuli (ie. maximal excitation) and the firing in response to the anti-preferred stimuli (ie. maximal inhibition) were plotted relative to SR. The data were normalized by subtracting the SR from the firing rates to preferred and anti-preferred

stimuli and averaged within groups. The maximal excitation rate was significantly greater for the ZII+ cells (ZII+ = 0.89±0.72 Hz (mean±SD); ZII- = 0.61±0.37 Hz; t-test; $p = 0.001$). Similarly, the maximal inhibition rate was also of a greater magnitude for all ZII+ cells (ZII+ = -0.47±0.27 Hz; ZII- = -0.35±0.23 Hz; t-test; $p = 0.002$). Figure 4.7B shows a mean wrapped Gaussian fit (thickness of line denoting ±1 SEM) across all directions of firing from all cells, with the preferred directions of each cell aligned to each other to show maximal and minimal firing rate differences. The gray circle, set to zero, denotes the spontaneous firing rate. This suggests that the difference in MI between ZII+ and ZII- cells is not due to either a greater excitation rate or a more inhibited rate, but rather both are of greater magnitudes (ZII+ show higher firing rates during excitation, and lower firing rates when inhibited). Again, the above data also helps suggest that the ZII+ PCs are more modulated than the ZII- PCs by visual input.

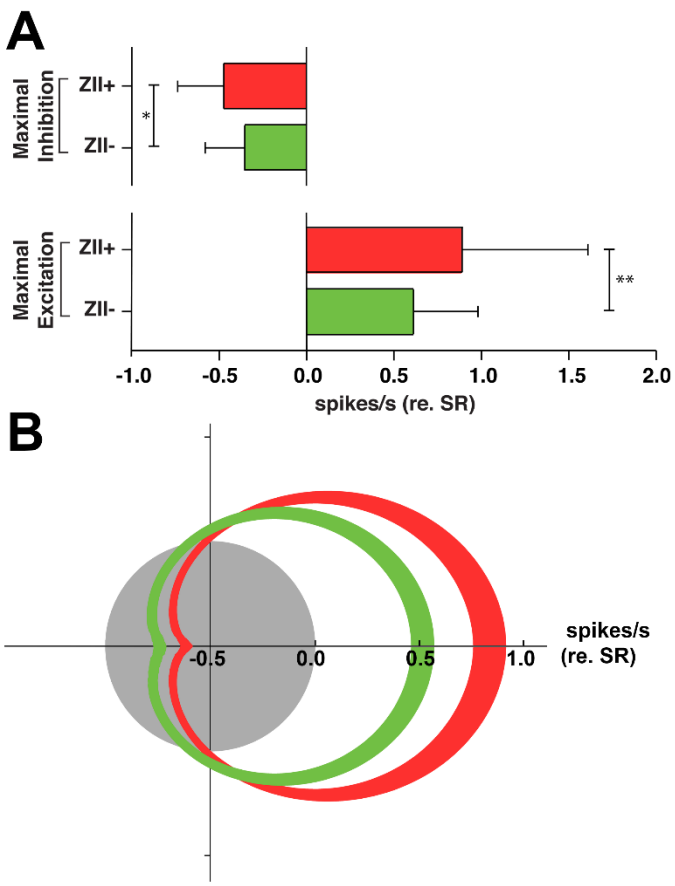

Figure 4.7: *Relative excitation and inhibition rates between ZII+ and ZII- PCs.* A: Histogram shows mean firing rates ±SD relative to the spontaneous firing rate (SR) during maximal excitation to motion in the preferred direction and maximal inhibition to motion in the anti-preferred direction of ZII+ and ZII- cells (ZII+ n = 111 ZII- n = 62, t-test, *p = 0.002, **p = 0.001) . B: comparison of tuning curves for all ZII+ (red) and ZII- (green) cells. Mean firing rates ±SEM (thickness of line) were plotted as a function of direction in polar coordinates. Gaussian fits for all tuning curves were rotated such that all the peaks aligned for more direct comparison. Gray circle denotes a spontaneous firing rate (set to 0 spikes/s).

4.3.5. *Temporal Dynamics of CS activity in ZII+ and ZII- Purkinje Cells*

Finally, we checked to see if this greater magnitude of firing rate modulation was sustained for the entire duration of the stimulus presentation, or if it was due to a burst of activity that skewed the overall firing rates. We binned the firing rates of all ZII+ and ZII- cells to look at three phases of the preferred (Figure 4.8A) and anti-preferred (Figure 4.8B) stimulus presentations. We observed an onset transient, (0-200ms) where the instantaneous CS activity is

on the order of several Hz (see also Figure 4.8C; 10ms bins). While there is a difference between ZII groups, this difference was not significant (t-test; $p = 0.10$). After the onset of stimulation (200-1000ms), the firing rate increases by almost double the SR for ZII+ PCs (t-test; ZII+ = 1.19±0.13 Hz, ZII- = 0.60±0.13 Hz (±SEM, above SR); $p = 0.005$). At this point, both ZII+ and ZII- cells show a sustained increase in firing rate for the remaining 4s of stimulus presentation (1000-5000 ms). The ZII+ cells maintain a faster firing rate over this final phase (t-test; ZII+ = 0.65±0.08 Hz ZII- = 0.40±0.05 Hz (±SEM, above SR); $p = 6.0 \times 10^{-4}$). To motion in the anti-preferred direction, the firing rate was stable and lower in the ZII+ PCs during both the 200-1000 ms phase, as well as the 1000-5000 ms phase (200-1000 ms; t-test; ZII+ = -0.57±0.04 Hz, ZII- = -0.33±0.08 Hz; $p = 0.01$; 1000-5000 ms; t-test; ZII+ = -0.41±0.03 Hz, ZII- = -0.28±0.04 Hz, (±SEM, below SR) $p = 0.01$). There was no difference between 0-200 ms (t-test; ZII+ = -0.10±0.10 Hz, ZII- = 0.21±0.17 Hz; $p = 0.12$). This data shows that ZII+ PCs show a sustained increase in firing rate to motion in the preferred direction, as well as a sustained decrease in firing rate to motion in the anti-preferred direction. Overall, the above data suggest that the ZII+ and ZII- PCs are involved in differing circuits, with the ZII+ PCs being much more sensitive to and modulated by visual input, although it is possible that the ZII- cells are preferentially modulated by other types of stimulus input.

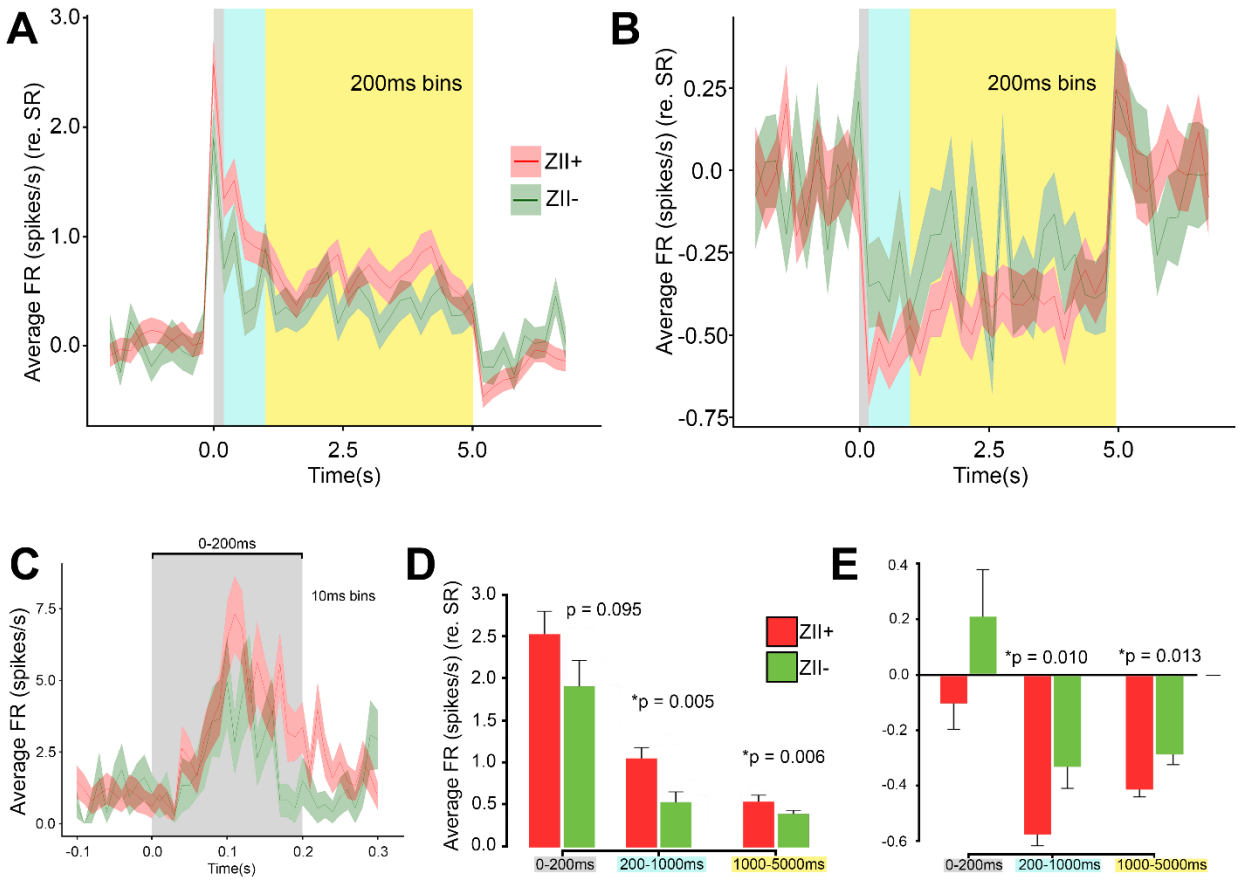

Figure 4.8*: Temporal firing rate dynamics of ZII+ and ZII- PC CSA in response to motion in the preferred and anti-preferred directions.* Peristimulus time histograms (PSTH) of CS activity in response to motion in the preferred (A) and anti-preferred directions (B). Firing rate (FR) is shown relative to SR. Bins are 200 ms, and the mean firing rate ±SEM (thickness of line) is shown for all ZII+ (red) and ZII- (green) cells. Each PSTH is divided into 0-200 ms (gray), 200-1000 ms (blue), and 1000-5000 ms (yellow) sections. C: 0-200 ms onset shows an initial transient spike in firing rate to motion in the preferred direction with 10ms bins. Note, the absolute firing rate is shown instead of the firing rate relative to SR as in A, B. D and E: comparisons of mean±SEM CS activity during the 0-200 ms, 200-1000 ms, and 1000-5000 ms sections in response to motion in the preferred (D) and anti-preferred (E) directions.

4.4. Discussion

Heterogenous molecular identities such as those defined by Zebrin (ZII) have been described in Purkinje cells (PCs) for more than 40 years (Apps and Hawkes, 2009), but only recently have researchers begun investigating physiological differences between ZII+ and ZII- PCs (Wadiche and Jahr, 2005; Sugihara et al., 2007; Ebner et al., 2012; Zhou et al., 2014; De

Zeeuw and Ten Brinke, 2015). In the present study, we provide evidence of a link between ZII identity and a physiological response to sensory stimuli, where ZII+ PCs exhibit a greater depth of complex spike (CS) modulation to optic flow, compared to the ZII- PCs within their functional unit.

Zhou et al. (2014) found that the spontaneous rate of CS activity in ZII+ and ZII- PCs differ: ZII- = 1.13±0.25 Hz (mean±SD), ZII+ = 0.92±0.28 Hz. Our results are near identical, with ZII- = 1.14±031 Hz, and ZII+ = 0.97±0.30 Hz. These are strikingly similar, especially when one considers the differences between the two studies: 1) Zhou et al (2014) uses awake rodents, while we examined anaesthetized pigeons. 2) Zhou et al (2014) examined the cerebellum more broadly, comparing ZII- PCs in the anterior lobe to ZII+ PCs in the posterior lobe, whereas we examined ZII+/- PCs within a single system (functional units within folia IXcd and X). Furthermore, these spontaneous rates are replicated once more in Xiao et al., (2014) from simultaneous recordings from ZII+/- in anaesthetized rodents. We emphasize the similarities of ZII patterning across the cerebellum in reptiles, birds, and mammals (Pakan et al., 2007; Wylie et al., 2016), and the similarities in CS spontaneous rate between ZII +/- cells across vertebrates further emphasizes that the associated physiology and underlying anatomy is conserved.

4.4.1. *CS activity modulation via circuitry*

We show that ZII+ PCs have a much greater increase in firing rates during excitation, and much lower firing rates during inhibition, resulting in a greater depth of modulation in response to visual stimulation compared to ZII- PCs. ZII+ PCs are also much more tightly tuned to the direction of visual stimulus presented. This difference is also sustained throughout the entire duration of the stimulus presentation and is not due to a transient increase or decrease in firing rate. However, this CS activity modulation is unlikely to be driven by the expression (or lack

thereof) of ZII, or of other molecular markers (Apps and Hawkes 2009). Instead, we believe that this difference is likely externally driven. CS activity is produced directly by inferior olive (IO) neurons through climbing fibres (CF), and these neurons have a special relationship with the PC such that when one CF fires, the PC it innervates will always fire in a one-to-one relationship (Eccles et al., 1966). As such, the changes in CS firing rate must be driven by the IO neurons, but what influences the firing of these neurons, and how is this change sustained? We suggest that the differences in modulation between the ZII+ and ZII- stripes in the VbC arise from a difference in circuitry through the IO, as depicted in Figure 4.9.

Modular units are common throughout the organization of the brain, and this is seen as well in the cerebellum. The cerebellum is divided into simple units, called the olivo-cerebellar circuit. A CF arises from the IO and synapses onto a single PC. The PC then projects a single axon down to the deep cerebellar nuclei, which in turn project back to the inferior olive (De Zeeuw, 1998). The standard olivo-cerebellar circuit is depicted as a closed loop: IO neurons project to PCs, which project to inhibitory neurons in the deep cerebellar nuclei, which project back to IO neurons. However, there are also open loop circuits where PCs project to regions of deep cerebellar nuclei that do not project back to the IO (De Zeeuw et al., 1994b), but rather target oculomotor regions or other areas. We propose that ZII+ and ZII- PCs in the pigeon VbC project to closed and open loops respectively, which accounts for differences in the depth of modulation to optic flow stimuli. This is illustrated in Figure 4.9 for the VA PCs.

The IO receives visual input from the accessory optic system (AOS) and the pretectum, which then travel via CFs to innervate PCs in the VbC. PCs in the VA zones (P4+/-, P6+/-) have been shown to project axons to distinct regions of the deep cerebellar nuclei: the core of the superior vestibular nucleus (VeS), the medial vestibular nucleus (VM), and the prepositus

hypoglossi (ph, Wylie et al., 2003). Further, it has been shown that the ZII+ PC terminals project to the VM and ph, but not the VeS core (Wylie et al., 2012). Since the VeS core receives PC innervation, but lacks ZII labeling, it is likely that it is the ZII- PCs from P4-/P6- that project to the VeS core, whereas P4+/P6+ PCs project to the VM and ph nuclei (Figure 4.9). Finally, albeit in mammals, it has been shown that only the VM and ph have inhibitory projections to the IO, completing the closed circuit (Balaban and Beryozkin, 1994; De Zeeuw et al., 1994a).

A similar argument can be made for the HA PCs in pigeon. HA zones P5+/- and P7+/- project to the medial region of VeS, the dorsolateral vestibular nucleus, and the infracerebellar nucleus. The latter two were shown to have heavy ZII+ terminal labeling, and the mammalian homologs have been shown to have inhibitory projections to the IO (De Zeeuw et al., 1994a; Wylie et al., 2012). There was no ZII labeling seen in the medial VeS, nor is there evidence of that region projecting to the IO.

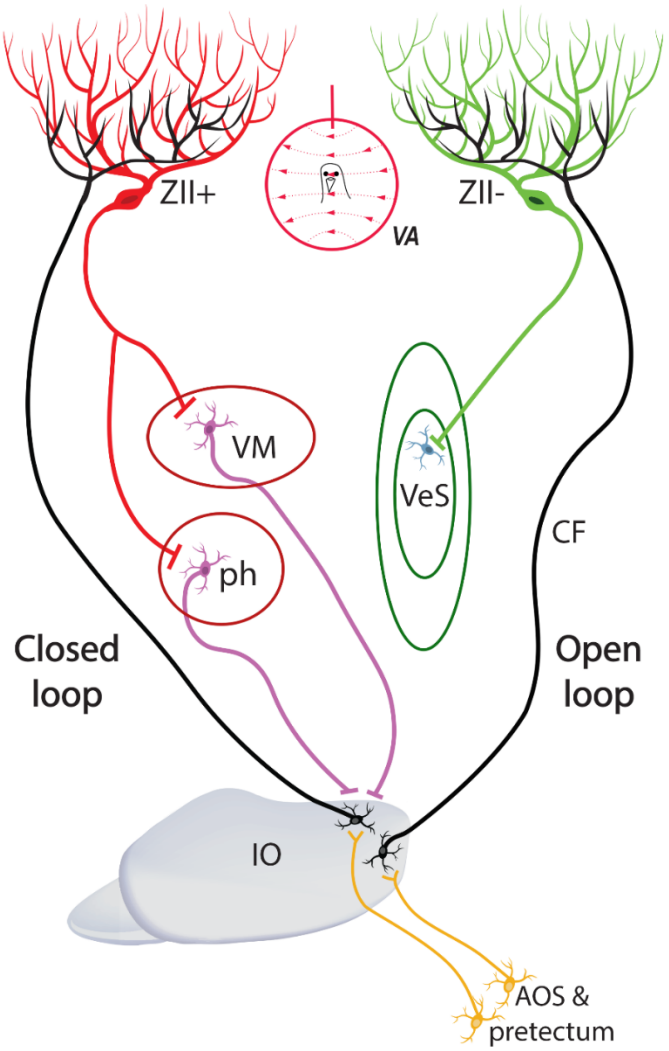

Figure 4.9: *Proposed open and closed loops of ZII+ (red) and ZII- (green) VA neurons.* ZII+ PCs in VA zones send inhibitory projections to the VM and ph, which normally inhibit the neurons in the IO that give rise to CFs. These CFs directly synapse onto the same PCs, creating a closed loop. When ZII+ PCs fire, they disinhibit the IO, they create a feed-forward circuit either enhancing activity during excitation or further inhibiting activity during inhibition. ZII- PCs in the VA zones project to the central core of VeS, which is not shown to project to the IO. This forms the open loop.VA, vertical axis; VM, medial vestibular nucleus; VeS, superior vestibular nucleus; CF, climbing fibre; ph, prepositus hypoglossi; IO, inferior olive; AOS, accessory optic system.

The proposed connectivity would explain differences in CS modulation depth to optic flow for the ZII+ neurons. The closed loop circuit provides the circuitry for a feed-forward mechanism through disinhibition and would account for the sustained, greater modulatory depth

exhibited by the ZII+ neurons. PCs are GABAergic (Ito, 1984), and the occurrence of a CS results in a profound inhibition of their target neurons (Blenkinsop and Lang, 2011). Thus, for a ZII+ VA PC, motion in the preferred direction would result in an increase in CS activity, resulting in significant inhibition of neurons in the VM and ph nuclei. This inhibition prevents the normally occurring inhibitory signals to the IO, which would release IO neurons from inhibition (disinhibition), increasing their overall firing rate and resultant CS activity. Overall, this would result in a further increase in CS activity to motion in the preferred direction. This follows for motion in the anti-preferred direction: ZII+ PCs would decrease firing onto the VM and ph nuclei, which would then exert their normal, inhibitive force on the IO, and decrease the resultant CS activity. The ZII- PCs do not experience this feed-forward activity, as the cerebellar nuclei they project to do not influence the neurons in the IO as do the ZII+ PCs.

There are other possible scenarios that could account for the differences in modulation of ZII+/- PCs. ZII+ and ZII- PCs of a functional unit receive CF input from separate, but adjacent regions of the IO (Wylie et al., 2017), so it is possible for these adjacent regions to receive differential input from the AOS and pretectum, but there is no indication for this in previous studies (Wylie, 2001). There is also excitatory feedback to the IO via the mesodiencephalic junction (De Zeeuw, 1998) and as such, could have differing effects on regions of the IO that provide the ZII+ and ZII- CF, so that the balance of inhibitory and excitatory inputs on these IO neurons vary. Alternatively, the ZII- PCs may also have a separate primary stimulus it is tuned to detect, such as vestibular manipulation.

4.4.2. *ZII+ and ZII- PCs and retinal stabilization*

The VbC is involved with the integration of visual-optokinetic and vestibular signals that control locomotion as the organism moves through space and mediates retinal image

stabilization. Stabilization during lower velocity movement is driven by visual signals, as the vestibular system is less sensitive to slower movement, whereas vestibular signals drive stabilization during higher velocity movement (Waespe and Henn, 1987; Yakusheva et al., 2007). As visual mossy fibres show preferential termination subjacent to the ZII+ PCs, (Pakan et al., 2010), it follows that they would be more visually driven, and therefore associated with slower movements, as there is more information to be gained from a slow moving object. This is consistent with comments from De Zeeuw and Ten Brinke, (2015) who suggest that ZII+ and ZII- PCs are involved with the control of slow and fast movements, respectively. While it is known that the pigeon VbC receives inputs from the vestibular system as mossy fibres, (Daz and Puelles, 2003; Pakan et al., 2008) it is not known if they specifically target the ZII- stripes. However, there is literature suggesting that mossy fibre afferents often do respect boundaries delineated by ZII (Pijpers et al., 2006), so it is likely that vestibular inputs would show some adherence to ZII boundaries. Based on these theories, it is possible that ZII- PCs are more likely to process faster movements, and each functional unit within the VbC would have a submodule for visual input, serviced by the ZII+ PCs, and a submodule for vestibular input, serviced by the ZII- PCs.

4.4.3. *ZII and cerebellar learning*

Recent studies suggest that, in mammals, ZII+ and ZII- cells differ with respect to the primary mechanism of synaptic plasticity during motor learning. ZII+ cells preferentially engage in long term potentiation (LTP), whereas ZII- cells employ long term depression strategies (LTD, (Wadiche and Jahr, 2005; Paukert et al., 2010; Wang et al., 2011; Ebner et al., 2012; Hawkes, 2014; Zhou et al., 2014; De Zeeuw and Ten Brinke, 2015). The association of ZII- cells with LTD has mainly been studied in the context of the conditioned eyeblink response in the

predominantly ZII- folium VI (Jirenhed et al., 2007; De Zeeuw and Ten Brinke, 2015), and the association of ZII+ cells and LTP has been primarily established through vestibulo-ocular reflex (VOR) learning in the flocculus of rodents (Voges et al., 2017). The flocculus in rodents is uniformly ZII+ (Brochu et al., 1990; Sillitoe and Hawkes, 2002), and studies have shown that disruption of LTP impairs VOR learning in rodents, while disruption of LTD does not (Schonewille et al., 2010, 2011; Gutierrez-Castellanos et al., 2017). We suggest that the plasticity of the VOR may be different in pigeons, as there are both ZII+ and ZII- PCs within the VbC. We speculate that, since both ZII+ and ZII- cells are present within a single functional unit, pigeons use both LTD and LTP during VOR learning, and that these are mediated by ZII- and ZII+ PCs respectively.

Furthermore, ZII- cells may be associated with paradigms involving gain enhancement, whereas ZII+ cells may be associated with paradigms involving gain suppression. Although this is a different scenario in rodents, in cats it has been reported that VOR enhancement is associated with LTD mechanisms and VOR suppression may be achieved through LTP (Titley et al., 2010; Broussard et al., 2011). It is noteworthy that the flocculus in cats as well as other mammals show ZII+ and ZII- stripes (Sillitoe et al., 2003; Fujita et al., 2010). Thus, it may be that a functional unit in the pigeon VbC consists of a ZII+ stripe that is more highly modulated by slow moving, visual input and is involved primarily with VOR suppression to slow the eye via LTP, and a ZII- stripe is less modulated by visual signals, though likely receiving vestibular input, and is involved in VOR enhancement via LTD to increase the eye velocity to stabilize the image.

This division of function may be due to the specific visual demands of the species, and therefore be present in birds but not rodents. For flying birds that use head bobbing for gaze stabilization during self-translation (Friedman, 1975), constant modification of the translational

VOR is necessary. When a bird is close to the substrate, the velocity of the visual optic flow is high compared to when the bird is further from the ground. Thus, when a bird is flying, distant from the ground, it is using slower visual optic flow signals for navigation, and thus requires a suppression of the translational VOR, which would involve the ZII+ stripes. However, as the bird approaches the substrate, a progressive enhancement of the translational VOR is needed to stabilize the quickly moving imagery, engaging the ZII- stripes and therefore diminishing the need for highly modulated visual optic flow signals.

4.4.4. *Functional modules and their subdivisions in the VbC*

The cerebellum, similar to other sensory systems across the brain, is made up of modules, and these modular divisions can often be further subdivided (Voogd and Glickstein, 1998; Meunier et al., 2010; Ruigrok, 2011; Apps et al., 2018). This project focuses on one such example where a functional module can be further subdivided, and these subdivisions appear to be driven by the stimulus feature itself. Graham and Wylie (2012) defined the functional unit as a ZII+/- stripe pair that respond to the same form of optic flow. This project now suggests that we reinstate the boundaries depicted by ZII, with the ZII+ half of the functional unit being more sensitive to the visual input, and the ZII- half being tuned towards vestibular input.

The alternating placement of differing sensory inputs is recapitulated in somatosensory cortex as well, with slowly adapting mechanoreceptors terminating in adjacent space to rapidly adapting mechanoreceptors, and this pattern is repeated for each receptive field (Mountcastle, 1997). Again, we see this paralleled in hypercolumns in visual cortex, with each hypercolumn split into two, with one half receiving input from the left eye, and the right half receiving input from the right eye (Hubel et al., 1977), and again this is repeated such that there is a hypercolumn for each receptive field. This alternating pattern helps bring together information

from two systems in a hierarchical fashion, but in somatosensory or visual cortex, that information is of the same modality, albeit different features within that sense. This is an example of two distinct sensory modalities brought together in the same manner and allows for integration and association between the two. However, this is an example where the next hierarchical level of organization is defined by a function, as opposed to a receptive field.

4.5. Future Directions

4.5.1. *Vestibular inputs to ZII- zones*

Pakan et al. (2010) demonstrated that visual inputs arising from mossy fibres from the LM and the nBOR, two visual nuclei in the AOS, preferentially terminate subjacent to ZII+ zones suggesting that ZII- zones receive inputs from other regions. A potential follow-up experiment would be to inject a retrograde tracer into the ZII- zones and see if neurons in the vestibular nuclear complex are labeled, or even neuronal bodies within Scarpa's ganglion. As discussed above, this would further support the idea that each functional zone integrates visual and vestibular information, with the ZII- relying on signals arising from vestibular motion, and the ZII+ PCs relying on visual signals arising from the AOS.

4.5.2. *Anterograde tracings of ZII- PC projections*

To confirm our hypothesis of a closed/open loop, one way to help support the existence of the open loop would be to inject anterograde tracers into ZII+ and ZII- PCs within a functional unit to see if they innervate separate regions of the vestibular nuclei. Additionally, retrograde tracers could be applied to oculomotor nuclei (possible location within the purported open circuit), and double labeling of cells within the vestibular system could help suggest the presence of an open circuit. Ultimately, it would be best if we could trace the circuit across synapses, to

visualize the full extent of the circuit. Several techniques for trans-synaptic tracing have been developed (see Saleeba et al., 2019 for review), though there are still significant limitations with non-selective labeling.

4.5.3. *VOR and non-VOR neurons*

In a series of papers, Mitsacos et al., (1983a, 1983b) describe two populations of cells within the superior vestibular nucleus: a centrally located population, which project to oculomotor areas, and a peripheral area, which project back to the cerebellum, and other areas. Anterograde tracers could help elucidate whether ZII+ PC axons terminate in the peripheral area, congruent with the closed loop hypothesis, and if ZII- PC axons terminate in the central area, as part of the open loop. We already have some data supporting ZII- axons terminating in the central region (Wylie et al., 2012).

4.6. Conclusions

The distinct, alternating modular zones in the cerebellum have been admired for decades, but there is still little understanding as to why it is arranged as such. Following results from a previous paper from our lab, Graham and Wylie (2012) demonstrated that cells within a ZII+/- stripe pair share the same visual stimulus preferences and were grouped as a functional unit. However, since ZII stripes receive differing inputs, this project aimed to reconcile these two contrasting findings. We found that the ZII+ cells show more modulatory depth in response to visual stimuli compared to ZII- cells, and that each functional unit has a more modulated zone (ZII+) and a lesser modulated zone (ZII-). We suggest, that based on electrophysiological signatures of both ZII+ and ZII- PCs within a functional unit, there are further nuances in their physiology, likely arising from the differing circuitry. These differences may be delineated along

sensory lines, with ZII+ PCs receiving input from visual systems, and the ZII- PCs receiving input from vestibular systems. This would allow each functional unit to have repeating "submodules" from two sensory modalities, allowing them to integrate this information to tackle different tasks within the vestibulo-ocular reflex. Much like how the rest of the brain maintains a separation of features from stimuli, this is perhaps an example of how this separation would allow for more appropriate, fine-tuned responses from the animal.

Chapter 5: Summary and Conclusions

Abbreviations

DRG	dorsal root ganglion
PC	Purkinje cells
Pcdh-γ	clustered protocadherins gamma subcluster
PNS	peripheral nervous system
VbC	vestibulocerebellum
ZII	Zebrin II

5. *Summary and Conclusions*

5.1. Summary of Chapters

This dissertation consists of projects investigating the patterning of sensory systems at different levels in three different animal models, in order to demonstrate common concepts important to their organization.

In Chapter 2, we started at the level of sensory terminals in the mammalian peripheral nervous system. The peripheral nervous system (PNS) is constantly at risk of injury, so the ongoing maintenance of sensory patterning is critically important. Driven by the recent description of the gamma subcluster of the clustered protocadherins (Pcdh-γ) and their role in self avoidance and tiling in the central nervous system (Wu and Maniatis, 1999; Lefebvre et al., 2012), we aimed to see if this was the mechanism in which the PNS used to allow self/non-self recognition to aid in patterning the complex innervation within the skin following regeneration. We found both expression of Pcdh-γ mRNA and protein in the PNS, mainly situated within the dorsal root ganglion (DRG) cell bodies. As well, we found that, following knockdown, naïve cultured DRG neurons showed much more outgrowth than controls. However, following a peripheral nerve injury, this increased outgrowth associated with Pcdh-γ knockdown was lost. We also noticed that injured neurons with Pcdh-γ knocked down engaged in less self crossings, but more neighbouring neuron crossings. Sensory neurons have been shown to engage in tiling, the process of neighbour avoidance, particularly in tissues with multiple subtypes that all must avoid redundant innervations of an area already serviced by a neuron of the same type (Grueber et al., 2002; Grueber and Sagasti, 2010; Lefebvre et al., 2012; Kuehn et al., 2019). Proper tiling is important in skin innervation, as it allows separation between cells that collect specific features of the sensory stimulus. Indeed, following Pcdh-γ knockdown *in vivo* following a

peripheral nerve injury, we noticed that there were more axons entering the epidermis than the contralateral footpad than seen in historic data, which could be because neurons are no longer restricted by neighbour avoidance. As well, this result is unique, as historically an injured footpad never approaches the same innervation levels as seen in the contralateral footpad.

This participation of Pcdh in the regenerating nervous system suggests a recapitulation of the mechanisms that drive the initial innervation during development. The ability for self/non-self recognition in neurons provides guidance to efficiently and effectively innervate the skin to provide adequate stimulus collection to aid the organism in navigating the outside environment. As we have shown that Pcdh likely plays a role in terminal patterning, they also have been shown to play a role in directing axonal projections. Seen in the olfactory glomeruli, as well as in serotonergic fibre projections, Pcdh plays a role in guiding large tracts to appropriate areas of the brain as well as locally directing terminal branching and even proper circuit formation (Chen et al., 2017; Hasegawa et al., 2017; Mountoufaris et al., 2017). Considering we see a maintenance of spatial relationship between peripheral terminals in the skin and the spinal cord (Kuehn et al., 2019), it is highly possible Pcdhs are linked to primary afferent terminations, such as those discussed in the Chapter 3. Our data on Pcdh in the PNS provides more evidence that the patterning process is not random, but purposeful, linked to the features of the sensory stimulus, and is enacted within a species, and across species.

The second project within this thesis is yet another example of the extent in which sensory systems are consistently patterned across species. Using a novel, *ex vivo* approach to trace the projection patterns from each semicircular canal in two species of snake, we were able to show conserved patterning of the primary afferent termination in two species of snakesthat dramatically differ in both ecological niche and body design compared to later branching

vertebrates. Not only were we able to repeat the results seen in other reptiles that stained a single canal per animal, but we also were able to repeat the results seen across other distantly related vertebrates like aves and primates, further confirming that the organization of vestibular terminals seen at the level of primary projections must be a conserved practice. This conservation across such a wide phylogenetic range speaks to the importance of how the system was initially designed. The partitioning of the terminations by each canal on secondary neurons in the context of the physiologic data put forth by Straka et al. (1997) maintains the separation of stimulus features, which likely aids in the integration in higher brain regions, as well as its relationship with the extraocular muscles to aid in the vestibulo-ocular reflex (Szentágothai, 1950; Pantle and Dieringer, 1998). Like other sensory systems that maintain sensory feature distinction as part of the organizational hierarchy, the separation of distinct aspects of sensory inputs allows for stepwise processing in higher cortex. However, here is where we see differences between the vestibular system and other sensory systems. In other systems we've mentioned before, there are multiple levels of organization in a hierarchical pattern. In the visual system, each hypercolumn represents a single receptive field, and those columns can be further divided, ending in further clusters of neurons that respond to single lines in varying orientations. The vestibular system lacks some of these features as it does not operate within a receptive field, rather it responds to motion of the entire system. Instead, perhaps we can relate the entire vestibular primary projection to a single hypercolumn, with all the canals terminating in distinct regions as do the orientation columns, segregated by specific but related features. This predictable, logical pattern likely aids in the proper interpretation of these signals. Chapter 4 describes an example of sensory interpretation across one such pattern.

The third project in this thesis highlights a logical pattern of sensory feature separation that is maintained during integration between two sensory modalities. The cerebellum is organized into alternating modules and can be visualized by the molecule, Zebrin II (ZII). Using the pigeon vestibulocerebellum, (VbC), we investigated the electrophysiological differences between ZII+ Purkinje cells (PC), and ZII- PCs. Since the VbC is organized into functional units, where all PCs respond to the same type of optic flow stimuli, but contain both ZII+ and ZII- cells, we compared the complex spike activity within a functional unit. We noticed that the ZII+ PCs exhibited greater modulation in response to motion in their preferred and anti-preferred direction, whereas ZII- PCs showed a more attenuated response. We propose the greater modulatory depth (ie. greater excitation firing rates, lower inhibitory firing rates), to be a result of specific circuitry resulting in a disinhibition, or feed-forward loop of activity involving the inferior olive, deep cerebellar nuclei, and the ZII+ PCs. We also propose that, due to the other inputs that selectively target the ZII+ PCs, we hypothesize that ZII+ and ZII- PCs specialize in different aspects of vestibulo-ocular reflex learning, and receive specific, alternating, sensory input. Since visual input seems to preferentially terminate below the ZII+ PCs (Pakan et al., 2010), as well as having been associated with slower movements (De Zeeuw and Ten Brinke, 2015), it is possible they are intricately involved with gain suppression during VOR learning, which slows eye movement (Broussard et al., 2011). We hypothesize that ZII- PCs receive primarily vestibular input, and have been linked to quicker movements (De Zeeuw and Ten Brinke, 2015), so it follows that they would participate in gain enhancement, or increasing eye velocity, during VOR learning. This would allow the eyes to increase their rotational speed to match the stimulus. Again, we can draw links back to the other sensory systems that alternate between inputs within the same receptive field. However, here we see an additional level to the

organizational hierarchy, but it is not depicted by receptive fields as it is in other systems. As hypothesized before, perhaps the vestibular system does not have a traditional receptive field, as movement of the entire organism causes its activation. Optic flow is similar, as it has a panoramic receptive field, meaning that the entire retina contributes to the processing of optic flow, and its receptive field encompasses the entire environment. Now the two systems can be compared within the same context, and we see that this comparison is likely completed in the vestibulocerebellum. Further, we provide our theory to link this integration to function. Having two adjacent cell populations within a functional unit handling the two ends of VOR learning, would allow the cerebellum to achieve the fine-tuned motor coordination it is famous for.

5.2. Conclusion

Sensory systems are patterned intentionally, and these conserved hierarchical patterns allow complex integrative functions to occur to allow the animal more freedom in responses. These patterns are driven internally, are replicated time and again within species and across phylogeny, and likely participate in fine-tuned sensory processing that has been developed and perfected over time. The patterns observed in the sensory nervous system are logical, predictable, ubiquitous, and appear to be driven by features of the stimulus itself. By keeping the idea of patterns present when approaching problems such as describing the fundamental organizational concepts of the brain and nervous system, we can provide much needed context and precedence to assist us in accurately understanding how the elephant in the room, the nervous system, works.

Works Cited

Abraira VE, Ginty DD (2013) The sensory neurons of touch. Neuron 79:618–639.

Ahn AH, Dziennis S, Hawkes R, Herrup K (1994) The cloning of zebrin II reveals its identity with aldolase C. Development 120:2081–2090.

Alexander G (1901) Zur Anatomie des Ganglion vestibulare der Säugethiere. Arch f Ohrenh 51:109–125.

Apps R et al. (2018) Cerebellar Modules and Their Role as Operational Cerebellar Processing Units. Cerebellum 17:654–682.

Apps R, Hawkes R (2009) Cerebellar cortical organization: a one-map hypothesis. Nat Rev Neurosci 10:670–681.

Arendt D, Hausen H, Purschke G (2009) The 'division of labour' model of eye evolution. Phil Trans R Soc B 364:2809–2817.

Aspden JW, Armstrong CL, Gutierrez-Ibanez CI, Hawkes R, Iwaniuk AN, Kohl T, Graham DJ, Wylie DR (2015) Zebrin II / aldolase C expression in the cerebellum of the western diamondback rattlesnake (Crotalus atrox). PLoS ONE 10:1–11.

Balaban CD, Beryozkin G (1994) Organization of vestibular nucleus projections to the caudal dorsal cap of Kooy in rabbits. Neuroscience 62:1217–1236.

Banelli B, Brigati C, Di Vinci A, Casciano I, Forlani A, Borzì L, Allemanni G, Romani M (2012) A pyrosequencing assay for the quantitative methylation analysis of the PCDHB gene cluster, the major factor in neuroblastoma methylator phenotype. Lab Invest 92:458–465.

Bangma GC (1983) Cerebellar connections in some reptiles.

Bangma GC, Donkelaar HJT (1982) Afferent connections of the cerebellum in various types of reptiles. J Comp Neurol 207:255–273.

Banker G (2003) Pars, PI 3-kinase, and the establishment of neuronal polarity. Cell 112:4–5.

Barbas-Henry HA, Lohman AHM (1988) Primary projections and efferent cells of the VIIIth cranial nerve in the monitor lizard, Varanus exanthematicus. J Comp Neurol 277:234–249.

Barmack NH, Yakhnitsa V (2008) Functions of interneurons in mouse cerebellum. J Neurosci 28:1140–1152.

Barrientos SA, Martinez NW, Yoo S, Jara JS, Zamorano S, Hetz C, Twiss JL, Alvarez J, Court FA (2011) Axonal degeneration is mediated by the mitochondrial permeability transition pore. J Neurosci 31:966–978.

Blenkinsop TA, Lang EJ (2011) Synaptic action of the olivocerebellar system on cerebellar nuclear spike activity. J Neurosci 31:14708–14720.

Bradke F, Fawcett JW, Spira ME (2012) Assembly of a new growth cone after axotomy: the precursor to axon regeneration. Nat Rev Neurosci 13:183–193.

Bradman MJG, Ferrini F, Salio C, Merighi A (2015) Practical mechanical threshold estimation in rodents using von Frey hairs/Semmes–Weinstein monofilaments: Towards a rational method. Journal of Neuroscience Methods 255:92–103.

Brochu G, Maler L, Hawkes R (1990) Zebrin II: A polypeptide antigen expressed selectively by Purkinje cells reveals compartments in rat and fish cerebellum. J Comp Neurol 291:538–552.

Broussard DM, Titley HK, Antflick J, Hampson DR (2011) Motor learning in the VOR: the cerebellar component. Exp Brain Res 210:451–463.

Brown MC, Lunn ER, Perry VH (1992) Consequences of slow wallerian degeneration for regenerating motor and sensory axons. J Neurobiol 23:521–536.

Burian M, Gstoettner W (1988) Projection of primary vestibular afferent fibres to the cochlear nucleus in the guinea pig. Neurosci Lett 84:13–17.

Butler AB, Hodos W (1996) Comparative vertebrate neuroanatomy: Evolution and adaptation. New York, NY, US: Wiley-Liss.

Cai D, Cohen KB, Luo T, Lichtman JW, Sanes JR (2013) Improved tools for the Brainbow toolbox. Nat Methods 10:540–547.

Carpenter MB, Stein BM, Peter P (1972) Primary vestibulocerebellar fibers in the monkey: Distribution of fibers arising from distinctive cell groups of the vestibular ganglia. Am J Anat 135:221–249.

Carriere CH, Sing AD, Wang WX, Jones BE, Yee Y, Ellegood J, Marocha J, Maganti H, Awofala L, Aziz A, Lerch JP, Lefebvre JL (2020) The gamma-protocadherins regulate the survival of GABAergic interneurons during developmentally regulated cell death. bioRxiv.

Casanova MF, El-Baz A, Switala A (2011) Laws of conservation as related to brain growth, aging, and evolution: Symmetry of the minicolumn. Front Neuroanat 5:1–9.

Catania KC, Kaas JH (1996) The unusual nose and brain of the star-nosed mole. BioScience 46:578–586.

Chen WV, Alvarez FJ, Lefebvre JL, Friedman B, Nwakeze C, Geiman E, Smith C, Thu CA, Tapia JC, Tasic B, Sanes JR, Maniatis T (2012) Functional significance of isoform diversification in the protocadherin gamma gene cluster. Neuron 75:402–409.

Chen WV, Nwakeze CL, Denny CA, Rieger MA, Mountoufaris G, Kirner A, Dougherty JD, Hen R, Wu Q, Maniatis T (2017) Pcdhac2 is required for axonal tiling and assembly of serotonergic circuitries in mice. Science 356:7.

Cheng C, Guo GF, Martinez JA, Singh V, Zochodne DW (2010) Dynamic plasticity of axons within a cutaneous milieu. J Neurosci 30:14735–14744.

Christie KJ, Krishnan A, Martinez JA, Purdy K, Singh B, Eaton S, Zochodne DW (2014) Enhancing adult nerve regeneration through the knockdown of retinoblastoma protein. Nat Commun 5:3670.

Conforti L, Gilley J, Coleman MP (2014) Wallerian degeneration: an emerging axon death pathway linking injury and disease. Nat Rev Neurosci 15:394–409.

Craciun I, Gutierrez-Ibañez C, Chan ASM, Luksch H, Wylie DR (2019) Secretagogin immunoreactivity reveals Lugaro cells in the pigeon cerebellum. Cerebellum 18:544–555.

Craciun I, Gutiérrez-Ibáñez C, Corfield JR, Hurd PL, Wylie DR (2018) Topographic organization of inferior olive projections to the zebrin II stripes in the pigeon cerebellar uvula. Front Neuroanat 12:18.

Cragg BG (1970) What is the signal for chromatolysis? Brain Res 23:1–21.

Dallosso AR et al. (2009) Frequent long-range epigenetic silencing of protocadherin gene clusters on chromosome 5q31 in Wilms' tumor. PLoS Genet 5:1–13.

Dallosso AR, Øster B, Greenhough A, Thorsen K, Curry TJ, Owen C, Hancock AL, Szemes M, Paraskeva C, Frank M, Andersen CL, Malik K (2012) Long-range epigenetic silencing of chromosome 5q31 protocadherins is involved in early and late stages of colorectal tumorigenesis through modulation of oncogenic pathways. Oncogene 31:4409–4419.

Daz C, Puelles L (2003) Plurisegmental vestibulocerebellar projections and other hindbrain cerebellar afferents in midterm chick embryos: biotinylated dextranamine experiments in vitro. Neuroscience 117:71–82.

De Zeeuw C (1998) Microcircuitry and function of the inferior olive. Trends Neurosci 21:391–400.

De Zeeuw CI, Gerrits NM, Voogd J, Leonard CS, Simpson JI (1994a) The rostral dorsal cap and ventrolateral outgrowth of the rabbit inferior olive receive a GABAergic input from dorsal group Y and the ventral dentate nucleus. J Comp Neurol 341:420–432.

De Zeeuw CI, Hoebeek FE, Bosman LWJ, Schonewille M, Witter L, Koekkoek SK (2011) Spatiotemporal firing patterns in the cerebellum. Nat Rev Neurosci 12:327–344.

De Zeeuw CI, Ten Brinke MM (2015) Motor learning and the cerebellum. Cold Spring Harb Perspect Biol 7:1–20.

De Zeeuw CI, Wylie DR, Digiorgi PL, Simpson JI (1994b) Projections of individual Purkinje cells of identified zones in the flocculus to the vestibular and cerebellar nuclei in the rabbit. J Comp Neurol 349:428–447.

Dickman JD, Angelaki DE (2002) Vestibular convergence patterns in vestibular nuclei neurons of alert primates. J Neurophysiol 88:3518–3533.

Dickman JD, Fang Q (1996) Differential central projections of vestibular afferents in pigeons. J Comp Neurol 367:110–131.

Dobzhansky T (1973) Nothing in biology makes sense except in the light of evolution. American Biology Teacher.

Duraikannu A, Krishnan A, Chandrasekhar A, Zochodne DW (2019) Beyond trophic factors: Exploiting the intrinsic regenerative properties of adult neurons. Front Cell Neurosci 13:1–22.

Duraikannu A, Martinez JA, Chandrasekhar A, Zochodne DW (2018) Expression and manipulation of the APC-β-catenin pathway during peripheral neuron regeneration. Sci Rep 8:1–15.

Ebner TJ, Wang X, Gao W, Cramer SW, Chen G (2012) Parasagittal zones in the cerebellar cortex differ in excitability, information processing, and synaptic plasticity. Cerebellum 11:418–419.

Eccles JC, Llinás R, Sasaki K (1966) The excitatory synaptic action of climbing fibres on the Purkinje cells of the cerebellum. J Physiol 182:268–296.

Esumi S, Kakazu N, Taguchi Y, Hirayama T, Sasaki A, Hirabayashi T, Koide T, Kitsukawa T, Hamada S, Yagi T (2005) Monoallelic yet combinatorial expression of variable exons of the protocadherin-α gene cluster in single neurons. Nat Genet 37:171–176.

Faul F, Erdfelder E, Lang A-G, Buchner A (2007) G*Power 3: A flexible statistical power analysis program for the social, behavioral, and biomedical sciences. Behavior Research Methods 39:175–191.

Finn JT, Weil M, Archer F, Siman R, Srinivasan A, Raff MC (2000) Evidence that wallerian degeneration and localized axon degeneration induced by local neurotrophin deprivation do not involve caspases. J Neurosci 20:1333–1341.

Foster RE, Hall WC (1978) The organization of central auditory pathways in a reptile, Iguana iguana. J Comp Neurol 178:783–831.

Fournier AE, Strittmatter SM (2001) Repulsive factors and axon regeneration in the CNS. Curr Opin Neurobiol 11:89–94.

Frank M, Ebert M, Shan W, Phillips GR, Arndt K, Colman DR, Kemler R (2005) Differential expression of individual gamma-protocadherins during mouse brain development. Mol Cell Neurosci 29:603–616.

Friedman MB (1975) Visual control of head movements during avian locomotion. Nature 255:67–69.

Fujita H, Oh-Nishi A, Obayashi S, Sugihara I (2010) Organization of the marmoset cerebellum in three-dimensional space: Lobulation, aldolase C compartmentalization and axonal projection. J Comp Neurol 518:1764–1791.

Garrett AM, Bosch PJ, Steffen DM, Fuller LC, Marcucci CG, Koch AA, Bais P, Weiner JA, Burgess RW (2019) CRISPR/Cas9 interrogation of the mouse Pcdhg gene cluster reveals a crucial isoform-specific role for Pcdhgc4 Garcia-Bassets I, ed. PLoS Genet 15:1–32.

Garrett AM, Schreiner D, Lobas MA, Weiner JA (2012) γ-protocadherins control cortical dendrite arborization by regulating the activity of a FAK/PKC/MARCKS signaling pathway. Neuron 74:269–276.

Gerdts J, Summers DW, Sasaki Y, DiAntonio A, Milbrandt J (2013) Sarm1-Mediated Axon Degeneration Requires Both SAM and TIR Interactions. Journal of Neuroscience 33:13569–13580.

Gierer A (1982) Model for the retino-tectal projection. Proc R Soc Lond B 218:77–93.

Glickstein M, Voogd J (2009) Cerebellum: Evolution and Comparative Anatomy. In: Encyclopedia of Neuroscience, pp 743–756. Elsevier.

Goldberg JM, Fernandez C (1980) Efferent vestibular system in the squirrel monkey: anatomical location and influence on afferent activity. J Neurophysiol 43:986–1025.

Graf W, Simpson JI, Leonard CS (1988) Spatial organization of visual messages of the rabbit's cerebellar flocculus. II. Complex and simple spike responses of Purkinje cells. J Neurophysiol 60:2091–2121.

Graham DJ, Wylie DR (2012) Zebrin-immunopositive and -immunonegative stripe pairs represent functional units in the pigeon vestibulocerebellum. J Neurosci 32:12769–12779.

Granit R, Phillips CG (1956) Excitatory and inhibitory processes acting upon individual Purkinje cells of the cerebellum in cats. J Physiol 133:520–547.

Gregory JE, Iggo A, McIntyre AK, Proske U (1988) Receptors in the bill of the platypus. J Physiol 400:349–366.

Grueber WB, Jan LY, Jan YN (2002) Tiling of the Drosophila epidermis by multidendritic sensory neurons. Development 129:2867–2878.

Grueber WB, Sagasti A (2010) Self-avoidance and tiling: Mechanisms of dendrite and axon spacing. Cold Spring Harb Perspect Biol 2:1–17.

Gutierrez-Castellanos N, Da Silva-Matos CM, Zhou K, Canto CB, Renner MC, Koene LMC, Ozyildirim O, Sprengel R, Kessels HW, De Zeeuw CI (2017) Motor learning requires purkinje cell synaptic potentiation through activation of AMPA-receptor subunit GluA3. Neuron 93:409–424.

Harada Y, Kasuga S, Tamura S (2001) Comparison and evolution of the lagena in various animal species. Acta Otolaryngol 121:355–363.

Hartline HK, Wagner HG, Ratliff F (1956) Inhibition of the eye of limulus. J Gen Physiol 39:651–673.

Hartline PH (1974) Thermoreception in Snakes. In: Electroreceptors and Other Specialized Receptors in Lower Vertrebrates (Fessard A, ed), pp 297–312. Berlin, Heidelberg: Springer Berlin Heidelberg.

Hasegawa S, Kobayashi H, Kumagai M, Nishimaru H, Tarusawa E, Kanda H, Sanbo M, Yoshimura Y, Hirabayashi M, Hirabayashi T, Yagi T (2017) Clustered Protocadherins Are Required for Building Functional Neural Circuits. Frontiers in Molecular Neuroscience 10 Available at: http://journal.frontiersin.org/article/10.3389/fnmol.2017.00114/full [Accessed December 5, 2018].

Hattori D, Millard SS, Wojtowicz WM, Zipursky SL (2008) Dscam-mediated cell recognition regulates neural circuit formation. Annu Rev Cell Dev Biol 24:597–620.

Hawkes R (2014) Purkinje cell stripes and long-term depression at the parallel fiber-Purkinje cell synapse. Front Syst Neurosci 8:1–11.

Herculano-Houzel (2010) Coordinated scaling of cortical and cerebellar numbers of neurons. Front Neuroanat 4:1–8.

Highstein SM, Holstein GR (2006) The anatomy of the vestibular nuclei. In: Progress in Brain Research, pp 157–203. Elsevier.

Hilgetag CC, Goulas A (2020) ‘Hierarchy’ in the organization of brain networks. Phil Trans R Soc B 375:20190319.

Hilton BJ, Bradke F (2017) Can injured adult CNS axons regenerate by recapitulating development? Development 144:3417–3429.

Hirayama T, Tarusawa E, Yoshimura Y, Galjart N, Yagi T (2012) CTCF is required for neural development and stochastic expression of clustered Pcdh genes in neurons. Cell Rep 2:345–357.

Hodos W, Butler AB (1997) Evolution of sensory pathways in vertebrates. Brain Behav Evol 50:189–197.

Honrubia V, Suarez C, Kuruvilla A, Sitko S (1985) Central projections of primary vestibular fibres in the bullfrog: III: The anterior semicircular canal afferents. Laryngoscope 95:1526–1535.

Hovaguimian A, Gibbons CH (2011) Diagnosis and Treatment of Pain in Small Fiber Neuropathy. Curr Pain Headache Rep 15:193–200.

Hubel DH, Wiesel TN (1963) Shape and arrangement of columns in cat's striate cortex. J Physiol 165:559-568.2.

Hubel DH, Wiesel TN, Stryker MP (1977) Orientation columns in macaque monkey visual cortex demonstrated by the 2-deoxyglucose autoradiographic technique. Nature 269:328–330.

Ing-Esteves S, Kostadinov D, Marocha J, Sing AD, Joseph KS, Laboulaye MA, Sanes JR, Lefebvre JL (2018) Combinatorial effects of alpha- and gamma-protocadherins on neuronal survival and dendritic self-avoidance. J Neurosci 38:2713–2729.

Ito M (1984) The Cerebellum and Neural Control. New York: Raven Press.

Jan Y-N, Jan LY (2010) Branching out: mechanisms of dendritic arborization. Nat Rev Neurosci 11:316–328.

Jessen KR, Mirsky R (2016) The repair Schwann cell and its function in regenerating nerves. J Physiol 594:3521–3531.

Jirenhed D-A, Bengtsson F, Hesslow G (2007) Acquisition, extinction, and reacquisition of a cerebellar cortical memory trace. J Neurosci 27:2493–2502.

Johnson BA, Leon M (2007) Chemotopic odorant coding in a mammalian olfactory system. J Comp Neurol 503:1–34.

Kaas JH (2008) The evolution of the complex sensory and motor systems of the human brain. Brain Res Bull 75:384–390.

Kandel ER, Schwartz JH, Jessell TM, Siegelbaum SA, Hudspeth AJ (2000) Principles of Neural Science, Fifth. New York, NY: McGraw-Hill, Health Professions Division.

Kaneko R, Kato H, Kawamura Y, Esumi S, Hirayama T, Hirabayashi T, Yagi T (2006) Allelic gene regulation of Pcdh-α and Pcdh-γ clusters involving both monoallelic and biallelic expression in single purkinje cells. J Biol Chem 281:30551–30560.

Karten HJ, Hodos W (1967) Stereotaxic atlas of the brain of the pigeon (Columba livia). The Johns Hopkins University Press.

Kohmura N, Senzaki K, Hamada S, Kai N, Yasuda R, Watanabe M, Ishii H, Yasuda M, Mishina M, Yagi T (1998) Diversity Revealed by a Novel Family of Cadherins Expressed in Neurons at a Synaptic Complex. Neuron 20:1137–1151.

Kostadinov D, Sanes JR (2015) Protocadherin-dependent dendritic self-avoidance regulates neural connectivity and circuit function. eLife 4:e08964.

Krarup C (2004) Compound sensory action potential in normal and pathological human nerves. Muscle Nerve 29:465–483.

Krishnan A, Purdy K, Chandrasekhar A, Martinez J, Cheng C, Zochodne DW (2018) A BRCA1-dependent DNA damage response in the regenerating adult periphera nerve milieu. Mol Neurobiol 55:4051–4067.

Kruger L (2001) Methods in Pain Research. Boca Raton, FL: CRC Press.

Kuehn ED, Meltzer S, Abraira VE, Ho C-Y, Ginty DD (2019) Tiling and somatotopic alignment of mammalian low-threshold mechanoreceptors. Proc Natl Acad Sci USA 116:9168–9177.

Kuruvilla A, Sitko S, Schwartz I, Honrubia V (1985) Central projections of primary vestibular fibres in the bullfrog: I. The vestibular nuclei. Laryngoscope 95:692–707.

Lange W (1975) Cell number and cell density in the cerebellar cortex of man and some other mammals. Cell Tissue Res 157:115–124.

Langer T, Fuchs AF, Scudder CA, Chubb MC (1985) Afferents to the flocculus of the cerebellum in the rhesus macaque as revealed by retrograde transport of horseradish peroxidase. J Comp Neurol 235:1–25.

Langley JN (1895) Note on regeneration of præ-ganglionic fibres of the sympathetic. J Physiol 18:280–284.

Larsell O (1926) The cerebellum of reptiles: Lizards and snake. J Comp Neurol 41:59–94.

Larsell O, Jansen J (1967) The Comparative Anatomy and Histology of the Cerebellum: From monotremes through apes. University of Minnesota Press.

Lefebvre JL (2017) Neuronal territory formation by the atypical cadherins and clustered protocadherins. Seminars in Cell & Developmental Biology 69:111–121.

Lefebvre JL, Kostadinov D, Chen WV, Maniatis T, Sanes JR (2012) Protocadherins mediate dendritic self-avoidance in the mammalian nervous system. Nature 488:517–521.

Lefebvre JL, Zhang Y, Meister M, Wang X, Sanes JR (2008) γ-Protocadherins regulate neuronal survival but are dispensable for circuit formation in retina. Development 135:4141–4151.

Li Y, Chen Z, Gao Y, Pan G, Zheng H, Zhang Y, Xu H, Bu G, Zheng H (2017) Synaptic adhesion molecule Pcdh-γC5 mediates synaptic dysfunction in Alzheimer's disease. J Neurosci 37:9259–9268.

Lieberman AR (1971) The axon reaction: A review of the principal features of perikaryal responses to axon injury. In: International Review of Neurobiology (Pfeiffer CC, Smythies JR, eds), pp 49–124. Academic Press.

López-Muñoz F, Boya J, Alamo C (2006) Neuron theory, the cornerstone of neuroscience, on the centenary of the Nobel Prize award to Santiago Ramón y Cajal. Brain Res Bull 70:391–405.

Mah KM, Houston DW, Weiner JA (2016) The γ-Protocadherin-C3 isoform inhibits canonical Wnt signalling by binding to and stabilizing Axin1 at the membrane. Sci Rep 6:1–17.

Mah KM, Weiner JA (2016) Clustered Protocadherins. In: The Cadherin Superfamily (Suzuki ST, Hirano S, eds), pp 195–221. Tokyo: Springer Japan. Available at: http://link.springer.com/10.1007/978-4-431-56033-3_8 [Accessed March 14, 2020].

Mannen H, Sasaki S, Ishizuka N (1982) Trajectory of primary vestibular fibers originating from the lateral, anterior, and posterior semicircular canals in the cat. Proc Jpn Acad Ser B Phys Biol Sci 58:237–242.

Masland RH (2012) The neuronal organization of the retina. Neuron 76:266–280.

Matesz C (1979) Central projection of the VIIIth cranial nerve in the frog. Neuroscience 4:2061–2071.

Meunier D, Lambiotte R, Bullmore ET (2010) Modular and hierarchically modular organization of brain networks. Front Neurosci 4:1–11.

Meyer RL (1998) Roger Sperry and his chemoaffinity hypothesis. Neuropsychologia 36:957–980.

Miller CT, Hale ME, Okano H, Okabe S, Mitra P (2019) Comparative principles for next-generation neuroscience. Front Behav Neurosci 13.

Miller MR, Kasahara M (1979) The cochlear nuclei of some turtles. J Comp Neurol 185:221–235.

Misra UK, Kalita J, Nair PP (2008) Diagnostic approach to peripheral neuropathy. Ann Indian Acad Neurol 11:89–97.

Mitsacos A, Reisine H, Highstein SM (1983a) The superior vestibular nucleus: An intracellular hrp study in the cat. I. Vestibulo-ocular neurons. J Comp Neurol 215:78–91.

Mitsacos A, Reisine H, Highstein SM (1983b) The superior vestibular nucleus: An intracellular hrp study in the cat. II. Non-vestibulo-ocular neurons. J Comp Neurol 215:92–107.

Moayedi M, Davis KD (2013) Theories of pain: from specificity to gate control. J Neurophysiol 109:5–12.

Molumby MJ, Keeler AB, Weiner JA (2016) Homophilic protocadherin cell-cell interactions promote dendrite complexity. Cell Rep 15:1037–1050.

Mountcastle V (1997) The columnar organization of the neocortex. Brain 120:701–722.

Mountoufaris G, Chen WV, Hirabayashi Y, O'Keeffe S, Chevee M, Nwakeze CL, Polleux F, Maniatis T (2017) Multicluster Pcdh diversity is required for mouse olfactory neural circuit assembly. Science 356:411–414.

Napper RMA, Harvey RJ (1988) Number of parallel fiber synapses on an individual Purkinje cell in the cerebellum of the rat. J Comp Neurol 274:168–177.

Navarro X, Vivó M, Valero-Cabré A (2007) Neural plasticity after peripheral nerve injury and regeneration. Prog Neurobiol 82:163–201.

Newlands SD, Perachio AA (2003) Central projections of the vestibular nerve: a review and single fiber study in the Mongolian gerbil. Brain Res Bull 60:475–495.

Nieuwenhuys R (1967) Comparative anatomy of the cerebellum. Prog Brain Res 25:1–93.

Novak P, Jensen T, Oshiro MM, Watts GS, Kim CJ, Futscher BW (2008) Agglomerative epigenetic aberrations are a common event in human breast cancer. Cancer Res 68:8616–8625.

Oh YM, Mahar M, Ewan EE, Leahy KM, Zhao G, Cavalli V (2018) Epigenetic regulator UHRF1 inactivates REST and growth suppressor gene expression via DNA methylation to promote axon regeneration. Proc Natl Acad Sci USA 115:1–10.

Osorio D, Vorobyev M (2008) A review of the evolution of animal colour vision and visual communication signals. Vision Res 48:2042–2051.

Pakan JMP, Graham DJ, Gutiérrez-Ibáñez C, Wylie DR (2011) Organization of the cerebellum: Correlating zebrin immunochemistry with optic flow zones in the pigeon flocculus. Vis Neurosci 28:163–174.

Pakan JMP, Graham DJ, Iwaniuk AN, Wylie DRW (2008) Differential projections from the vestibular nuclei to the flocculus and uvula-nodulus in pigeons (Columba livia). J Comp Neurol 508:402–417.

Pakan JMP, Graham DJ, Wylie DR (2010) Organization of visual mossy fiber projections and zebrin expression in the pigeon vestibulocerebellum. J Comp Neurol 518:175–198.

Pakan JMP, Graham DJ, Wylie DR (2014) Climbing fiber projections in relation to zebrin stripes in the ventral uvula in pigeons: climbing fiber projections to ventral uvula. J Comp Neurol 522:3629–3643.

Pakan JMP, Iwaniuk AN, Wylie DRW, Hawkes R, Marzban H (2007) Purkinje cell compartmentation as revealed by Zebrin II expression in the cerebellar cortex of pigeons (Columba livia). J Comp Neurol 501:619–630.

Pantle C, Dieringer N (1998) Spatial transformation of semicircular canal signals into abducens motor signals. A comparison between grass frogs and water frogs. J Comp Physiol A 182:475–487.

Parnas D, Linial M (1997) Acceleration of neuronal maturation of P19 cells by increasing culture density. Brain Res Dev Brain Res 101:115–124.

Paukert M, Huang YH, Tanaka K, Rothstein JD, Bergles DE (2010) Zones of enhanced glutamate release from climbing fibers in the mammalian cerebellum. J Neurosci 30:7290–7299.

Penfield W, Boldrey E (1937) Somatic motor and sensory representation in the cerebral cortex of man as studied by electrical stimulation. Brain 60:389–443.

Pfaffl MW (2001) A new mathematical model for relative quantification in real-time RT-PCR. Nucleic Acids Res 29:45e–445.

Pijpers A, Apps R, Pardoe J, Voogd J, Ruigrok TJH (2006) Precise spatial relationships between mossy fibers and climbing fibers in rat cerebellar cortical zones. J Neurosci 26:12067–12080.

Poitras T, Chandrasekhar A, McCoy L, Komirishetty P, Areti A, Webber CA, Zochodne DW (2019) Selective sensory axon reinnervation and TRPV1 activation. Mol Neurobiol 56:7144–7158.

Prasad T, Wang X, Gray PA, Weiner JA (2008) A differential developmental pattern of spinal interneuron apoptosis during synaptogenesis: insights from genetic analyses of the protocadherin- gene cluster. Development 135:4153–4164.

Prinz AA, Bucher D, Marder E (2004) Similar network activity from disparate circuit parameters. Nat Neurosci 7:1345–1352.

Radio NM, Breier JM, Shafer TJ, Mundy WR (2008) Assessment of chemical effects on neurite outgrowth in PC12 cells using high content screening. Toxicol Sci 105:106–118.

Ramírez OA, Couve A (2011) The endoplasmic reticulum and protein trafficking in dendrites and axons. Trends Cell Biol 21:219–227.

Ramon y Cajal S (1889) Sur l'origene et la direction des prolongations nerveuses de la couche moleculaire du cervelet. Int Monatschr Anat Physiol 6.

Ramon y Cajal S (1911) Histologie du système nerveux de l'homme et des vertébrés. Maloine, Paris 2:153–173.

Randel N, Jékely G (2016) Phototaxis and the origin of visual eyes. Phil Trans R Soc B 371:20150042.

Rishal I, Golani O, Rajman M, Costa B, Ben-Yaakov K, Schoenmann Z, Yaron A, Basri R, Fainzilber M, Galun M (2013) WIS-neuromath enables versatile high throughput analyses of neuronal processes. Dev Neurobiol 73:247–256.

Robinson LR (2000) Traumatic injury to peripheral nerves. Muscle Nerve 23:863–873.

Ruigrok TJH (2003) Collateralization of climbing and mossy fibers projecting to the nodulus and flocculus of the rat cerebellum. J Comp Neurol 466:278–298.

Ruigrok TJH (2011) Ins and Outs of Cerebellar Modules. Cerebellum 10:464–474.

Saleeba C, Dempsey B, Le S, Goodchild A, McMullan S (2019) A student's guide to neural circuit tracing. Front Neurosci 13:897.

Sanes JR, Zipursky SL (2010) Design principles of insect and vertebrate visual systems. Neuron 66:15–36.

Sargent PB (1989) What distinguishes axons from dendrites? Neurons know more than we do. Trends Neurosci 12:203–205.

Saxe JG (1868) The poems of John Godfrey Saxe: Complete in one volume. Ticknor and Fields.

Schmolesky MT, Weber JT, De Zeeuw CI, Hansel C (2002) The making of a complex spike: Ionic composition and plasticity. Ann N Y Acad Sci 978:359–390.

Schmucker D, Chen B (2009) Dscam and DSCAM: Complex genes in simple animals, complex animals yet simple genes. Genes Dev 23:147–156.

Schmucker D, Clemens JC, Shu H, Worby CA, Xiao J, Muda M, Dixon JE, Zipursky SL (2000) Drosophila Dscam is an axon guidance receptor exhibiting extraordinary molecular diversity. Cell 101:671–684.

Schonewille M, Belmeguenai A, Koekkoek SK, Houtman SH, Boele HJ, van Beugen BJ, Gao Z, Badura A, Ohtsuki G, Amerika WE, Hosy E, Hoebeek FE, Elgersma Y, Hansel C, De Zeeuw CI (2010) Purkinje cell-specific knockout of the protein phosphatase PP2B impairs potentiation and cerebellar motor learning. Neuron 67:618–628.

Schonewille M, Gao Z, Boele H-J, Vinueza Veloz MF, Amerika WE, Šimek AAM, De Jeu MT, Steinberg JP, Takamiya K, Hoebeek FE, Linden DJ, Huganir RL, De Zeeuw CI (2011) Reevaluating the role of LTD in cerebellar motor learning. Neuron 70:43–50.

Schreiner D, Weiner JA (2010) Combinatorial homophilic interaction between -protocadherin multimers greatly expands the molecular diversity of cell adhesion. Proc Natl Acad Sci USA 107:14893–14898.

Schwarz IE, Schwarz DWF (1983) The primary vestibular projection to the cerebellar cortex in the pigeon (Columba livia). J Comp Neurol 216:438–444.

Seddon HJ (1943) Three types of nerve injury. Brain 66:237–288.

Senger J-LB, Verge VMK, Chan KM, Webber CA (2018) The nerve conditioning lesion: A strategy to enhance nerve regeneration. Ann Neurol 83:691–702.

Severson PL, Tokar E, Vrba L, Waalkes M, Futscher B (2012) Agglomerates of aberrant DNA methylation are associated with toxicant-induced malignant transformation. Epigenetics 7:1238–1248.

Sherrington C (1952) The integrative action of the nervous system. CUP Archive.

Shi S-H, Jan LY, Jan Y-N (2003) Hippocampal neuronal polarity specified by spatially localized mPar3/mPar6 and PI 3-kinase activity. Cell 112:63–75.

Sillitoe RV, Hawkes R (2002) Whole-mount immunohistochemistry: A high-throughput screen for patterning defects in the mouse cerebellum. J Histochem Cytochem 50:235–244.

Sillitoe RV, Hulliger M, Dyck R, Hawkes R (2003) Antigenic compartmentation of the cat cerebellar cortex. Brain Res 977:1–15.

Sillitoe RV, Marzban H, Larouche M, Zahedi S, Affanni J, Hawkes R (2005) Conservation of the architecture of the anterior lobe vermis of the cerebellum across mammalian species. In: Progress in Brain Research, pp 283–297. Elsevier.

Simpson JI (1984) The accessory optic system. Annu Rev Neurosci 7:13–41.

Simpson JI, Wylie DR, De Zeeuw CI (1996) On climbing fiber signals and their consequence(s). Behav Brain Sci 19:384–398.

Soba P, Zhu S, Emoto K, Younger S, Yang S-J, Yu H-H, Lee T, Jan LY, Jan Y-N (2007) Drosophila sensory neurons require Dscam for dendritic self-avoidance and proper dendritic field organization. Neuron 54:403–416.

Sperry RW (1943) Effect of 180-degree rotation of the retinal field on visuomotor coordination. J Exp Zool 92:263–279.

Stein BM, Carpenter MB (1967) Central projections of portions of the vestibular ganglia innervating specific parts of the labyrinth in the rhesus monkey. Am J Anat 120:281–317.

Straka H, Baker R (2013) Vestibular blueprint in early vertebrates. Front Neural Circuits 7:1–9.

Straka H, Biesdorf S, Dieringer N (1997) Canal-specific excitation and inhibition of frog second-order vestibular neurons. J Neurophysiol 78:1363–1372.

Suarez C, Kuruvilla A, Sitko S, Schwartz I, Honrubia V (1985) Central projections of primary vestibular fibres in the bullfrog: II. Nerve branches from individual receptors. Laryngoscope 95:1238–1250.

Sugihara I, Marshall SP, Lang EJ (2007) Relationship of complex spike synchrony bands and climbing fiber projection determined by reference to aldolase C compartments in crus IIa of the rat cerebellar cortex. J Comp Neurol 501:13–29.

Sulaiman W, Gordon T (2013) Neurobiology of peripheral nerve injury, regeneration, and functional recovery: From bench top research to bedside application. Ochsner J 13:100–108.

Sunderland S (1951) A classification of peripheral nerve injuries producing loss of function. Brain 74:491–516.

Suo L, Lu H, Ying G, Capecchi MR, Wu Q (2012) Protocadherin clusters and cell adhesion kinase regulate dendrite complexity through Rho GTPase. J Mol Cell Biol 4:362–376.

Szentágothai J (1950) The elementary vestibulo-ocular reflex arc. J Neurophysiol 13:395–407.

Talavage TM, Sereno MI, Melcher JR, Ledden PJ, Rosen BR, Dale AM (2004) Tonotopic organization in human auditory cortex revealed by progressions of frequency sensitivity. J Neurophysiol 91:1282–1296.

Tasic B, Nabholz CE, Baldwin KK, Kim Y, Rueckert EH, Ribich SA, Cramer P, Wu Q, Axel R, Maniatis T (2002) Promoter Choice Determines Splice Site Selection in Protocadherin a and g Pre-mRNA Splicing. mol cell 10:21–33.

Taylor CA, Braza D, Rice JB, Dillingham T (2008) The incidence of peripheral nerve injury in extremity trauma. Am J Phys Med Rehabil 87:381–385.

Ten Donkelaar HJ, Bangma GC, Boer-van Huizen R (1983) Reticulospinal and vestibulospinal pathways in the snake Python regius. Anat Embryol 168:277–289.

Themistocleous AC, Ramirez JD, Serra J, Bennett DLH (2014) The clinical approach to small fibre neuropathy and painful channelopathy. Pract Neurol 14:368–379.

Titley HK, Heskin-Sweezie R, Broussard DM (2010) The bidirectionality of motor learning in the vestibulo-ocular reflex is a function of cerebellar mGluR1 receptors. J Neurophysiol 104:3657–3666.

Toth C, Brussee V, Zochodne DW (2006) Remote neurotrophic support of epidermal nerve fibres in experimental diabetes. Diabetologia 49:1081–1088.

Verge VMK, Gratto KA, Karchewski LA, Richardson PM (1996) Neurotrophins and nerve injury in the adult. Phil Trans R Soc Lond B 351:423–430.

Vogels R, Orban GA (1994) Activity of inferior temporal neurons during orientation discrimination with successively presented gratings. J Neurophysiol 71:1428–1451.

Voges K, Wu B, Post L, Schonewille M, De Zeeuw CI (2017) Mechanisms underlying vestibulo-cerebellar motor learning in mice depend on movement direction: Adaptation of compensatory eye movements in directional learning. J Physiol 595:5301–5326.

Voogd J, Glickstein M (1998) The anatomy of the cerebellum. Trends Neurosci 21:370–375.

Voogd J, Wylie DRW (2004) Functional and anatomical organization of floccular zones: A preserved feature in vertebrates. J Comp Neurol 470:107–112.

Wadiche JI, Jahr CE (2005) Patterned expression of Purkinje cell glutamate transporters controls synaptic plasticity. Nat Neurosci 8:1329–1334.

Waespe W, Henn V (1987) Gaze stabilization in the primate: The interaction of the vestibulo-ocular reflex, optokinetic nystagmus, and smooth pursuit. In: Reviews of Physiology, Biochemistry and Pharmacology, Volume 94, pp 37–125. Berlin, Heidelberg: Springer.

Waha A, Güntner S, Huang TH-M, Yan PS, Arslan B, Pietsch T, Wiestler OD, Waha A (2005) Epigenetic silencing of the protocadherin family member PCDH-γ-A11 in astrocytomas. Neoplasia 7:193–199.

Waller A (1850) Experiments on the section of the glossopharyngeal and hypoglossal nerves of the frog, and observations of the alterations produced thereby in the structure of their primitive fibres. Phil Trans R Soc Lond B 140:423–429.

Wang F, Julien DP, Sagasti A (2013) Journey to the skin: Somatosensory peripheral axon guidance and morphogenesis. Cell Adh Migr 7:388–394.

Wang X, Chen G, Gao W, Ebner TJ (2011) Parasagittally aligned, mGluR1-dependent patches are evoked at long latencies by parallel fiber stimulation in the mouse cerebellar cortex in vivo. J Neurophysiol 105:1732–1746.

Wang X, Weiner JA, Levi S, Craig AM, Bradley A, Sanes JR (2002) Gamma protocadherins are required for survival of spinal interneurons. Neuron 36:843–854.

Warner FJ (1935) The medulla of Crotalus atrox. J Nerv Ment Dis:504–523.

Warner FJ (1945) The diencephalon and midbrain of the american rattlesnake (Crotalus adamanteus). Proceedings of the Zoological Society of London 116:531–550.

Webber CA, Christie KJ, Cheng C, Martinez JA, Singh B, Singh V, Thomas D, Zochodne DW (2011) Schwann cells direct peripheral nerve regeneration through the Netrin-1 receptors, DCC and Unc5H2. Glia 59:1503–1517.

Weston JK (1936) The reptilian vestibular and cerebellar gray with fiber connections. J Comp Neurol 65:93–199.

Wiest G (2015) The origins of vestibular science. Ann NY Acad Sci 1343:1–9.

Wilson VJ, Felpel LP (1972) Semicircular canal inputs to vestibular nuclear neurons in the pigeon. In: Progress in Brain Research, pp 157–163. Elsevier.

Winship IR, Hurd PL, Wylie DRW (2005) Spatiotemporal tuning of optic flow inputs to the vestibulocerebellum in pigeons: Differences between mossy and climbing fiber pathways. J Neurophysiol 93:1266–1277.

Wojtowicz WM, Wu W, Andre I, Qian B, Baker D, Zipursky SL (2007) A vast repertoire of Dscam binding specificities arises from modular interactions of variable Ig domains. Cell 130:1134–1145.

Woolsey TA, Van der Loos H (1970) The structural organization of layer IV in the somatosensory regions (SI) of mouse cerebral cortex. Brain Res 17:205–242.

Wu Q (2001) Comparative DNA sequence analysis of mouse and human protocadherin gene clusters. Genome Res 11:389–404.

Wu Q, Maniatis T (1999) A striking organization of a large family of human neural cadherin-like cell adhesion genes. Cell 97:779–790.

Wylie DR (2001) Projections from the nucleus of the basal optic root and nucleus lentiformis mesencephali to the inferior olive in pigeons (Columba livia). J Comp Neurol 429:502–513.

Wylie DR, Bischof WF, Frost BJ (1998) Common reference frame for neural coding of translational and rotational optic flow. Nature 392:278–282.

Wylie DR, Brown MR, Barkley RR, Winship IR, Crowder NA, Todd KG (2003) Zonal organization of the vestibulocerebellum in pigeons (Columba livia): II. Projections of the rotation zones of the flocculus. J Comp Neurol 456:140–153.

Wylie DR, Frost BJ (1993) Responses of pigeon vestibulocerebellar neurons to optokinetic stimulation. II. The 3-dimensional reference frame of rotation neurons in the flocculus. J Neurophysiol 70:2647–2659.

Wylie DR, Gutiérrez-Ibáñez C, Corfield JR, Craciun I, Graham DJ, Hurd PL (2017) Inferior olivary projection to the zebrin II stripes in lobule IXcd of the pigeon flocculus: A retrograde tracing study. J Comp Neurol 525:3158–3173.

Wylie DR, Hoops D, Aspden JW, Iwaniuk AN (2016) Zebrin II is expressed in sagittal stripes in the cerebellum of dragon lizards (Ctenophorus sp.). Brain Behav Evol 88:177–186.

Wylie DR, Kripalani T, Frost BJ (1993) Responses of pigeon vestibulocerebellar neurons to optokinetic stimulation. I. Functional organization of neurons discriminating between translational and rotational visual flow. J Neurophysiol 70:2632–2646.

Wylie DR, Pakan JMP, Huynh H, Graham DJ, Iwaniuk AN (2012) Distribution of zebrin-immunoreactive Purkinje cell terminals in the cerebellar and vestibular nuclei of birds. J Comp Neurol 520:1532–1546.

Xiao J, Cerminara NL, Kotsurovskyy Y, Aoki H, Burroughs A, Wise AK, Luo Y, Marshall SP, Sugihara I, Apps R, Lang EJ (2014) Systematic regional variations in Purkinje cell spiking patterns Chédotal A, ed. PLoS ONE 9:1–14.

Yahata N, Yuasa S, Araki T (2009) Nicotinamide mononucleotide adenylyltransferase expression in mitochondrial matrix delays Wallerian degeneration. J Neurosci 29:6276–6284.

Yakusheva TA, Blazquez PM, Chen A, Angelaki DE (2013) Spatiotemporal properties of optic flow and vestibular tuning in the cerebellar nodulus and uvula. J Neurosci 33:15145–15160.

Yakusheva TA, Shaikh AG, Green AM, Blazquez PM, Dickman JD, Angelaki DE (2007) Purkinje cells in posterior cerebellar vermis encode motion in an inertial reference frame. Neuron 54:973–985.

Yang J, Weimer RM, Kallop D, Olsen O, Wu Z, Renier N, Uryu K, Tessier-Lavigne M (2013) Regulation of axon degeneration after injury and in development by the endogenous calpain inhibitor calpastatin. Neuron 80:1175–1189.

Zhou H, Lin Z, Voges K, Ju C, Gao Z, Bosman LW, Ruigrok TJ, Hoebeek FE, De Zeeuw CI, Schonewille M (2014) Cerebellar modules operate at different frequencies. eLife 3:1–18.

Zigmond RE, Echevarria FD (2019) Macrophage biology in the peripheral nervous system after injury. Prog Neurobiol 173:102–121.

Zipursky SL, Sanes JR (2010) Chemoaffinity revisited: Dscams, protocadherins, and neural circuit assembly. Cell 143:343–353.

Zochodne DW (2008) Neurobiology of Peripheral Nerve Regeneration. Cambridge: Cambridge University Press.

Zochodne DW (2012) The challenges and beauty of peripheral nerve regrowth. J Peripher Nerv Syst 17:1–18.

Zubkow K (2018) A novel non-viral knockdown strategy targeting retinoblastoma protein for regeneration of peripheral axons.

Zurborg S, Piszczek A, Martínez C, Hublitz P, Al Banchaabouchi M, Moreira P, Perlas E, Heppenstall PA (2011) Generation and characterization of an Advillin-Cre driver mouse line. Mol Pain 7:1–10.

Zylka MJ, Rice FL, Anderson DJ (2005) Topographically distinct epidermal nociceptive circuits revealed by axonal tracers targeted to Mrgprd. Neuron 45:17–25.